5-3-2019

Framework for Algorithmically Optimizing Longitudinal Health Outcomes: Examples in Cancer Radiotherapy and Occupational Radiation Protection

Lydia Joyce Wilson
Louisiana State University and Agricultural and Mechanical College

FRAMEWORK FOR ALGORITHMICALLY OPTIMIZING LONGITUDINAL HEALTH OUTCOMES: EXAMPLES IN CANCER RADIOTHERAPY AND OCCUPATIONAL RADIATION PROTECTION

A Dissertation

Submitted to the Graduate Faculty of the
Louisiana State University and
Agricultural and Mechanical College
in partial fulfillment of the
requirements for the degree of
Doctor of Philosophy

in

The Department of Physics and Astronomy

by
Lydia Joyce Wilson
B.A., University of California, Berkeley, 2009
M.S., Louisiana State University, 2013
August 2019

Copyright

Acknowledgements

I would like to thank my advisor, Dr. Wayne Newhauser, for his support and guidance throughout the course of this project. I also thank the members of my advisory committee: Dr. Wei-Hsung Wang, Dr. Juana Moreno, Dr. Joyoni Dey, Dr. Shafiqul Chowdhury, and Dr. Robert Carver, for their assistance and time. Without their mentorship, I wouldn't be where I am today.

A special thanks to my colleagues at the PTB and Klinikum Grosshadern in Germany, for their hospitality and measurement assistance, and to Mr. Phillip Wall and Dr. Jonas Fontenot for providing the sample-population data, without which this project would not have been nearly as successful as it was. I would like to acknowledge the members of our research group, my fellow students, and colleagues, whose help, input, and edits were invaluable: William Donahue, Christopher Schneider, Margaret Carey, Meagan Moore, and Addie Barron. Of course, none of this would have been possible without the aid and advocacy of the support staff, Susan Hammond and Yao Zeng.

This project was made possible by funding support from the Bella Bowman Foundation, the Nuclear Regulatory Commission, Louisiana State University, and the DAAD (translates to the German Academic Exchange Service).

I would also like to thank my friends and family. Their love and support has allowed me to become who I am today and helped to keep me focused and grounded through my seemingly unending graduate studies. Finally, I'd like to thank my fiancé, Martial. I couldn't have gotten through this without his unwavering patience, love, and support and I'm so excited to see where life after LSU takes us!

Table of Contents

List of Tables

List of Figures

Abstract

Background: Advancements in the treatment of non-infectious disease have enabled survival rates to steadily increase in recent decades (*e.g.,* diabetes, heart disease, and cancer). Epidemiological studies have revealed that the treatments for these diseases can have life-threatening and/or life–altering effects. Thus, realizing the full beneficial potential of advanced treatments necessitates new tools to algorithmically consider all major components of the health outcome, including benefit and detriment. The goal of this dissertation was to develop a framework for improving projected health outcomes following planned radiation exposures in consideration of all beneficial and detrimental, early and late, and fatal and non-fatal effects.

Methods: We designed a generally applicable framework for aggregating the benefits and detriments of planned exposures to individuals, groups, and populations. We demonstrated the utility of this framework with illustrative hypothetical example applications to emergency response, diagnostic radiology, and cancer radiotherapy. Finally, we used this new framework to directly optimize health outcomes in a population of men with prostate cancer receiving radiotherapy. We compared the resulting projected outcomes to those of conventional treatment-planning methods.

Results: Applications of the comprehensive framework to three illustrative scenarios revealed the utility of this framework for guiding objective and algorithmic decision making. Radiotherapy outcome-optimization methods yielded equivalent or superior projected health outcomes compared to conventional dose-optimization methods for every patient in the population. On average, outcome-optimized plans increased the probability of treatment benefit by 1%, while simultaneously decreasing the cumulative probability of long- and short-term treatment side effects by 3% compared to conventional treatment plans. We estimate that this would add up to 7

additional healthy-life months to each patients' life expectancy compared to that from conventional treatment plans.

Conclusions: The major finding is that it is feasible to directly optimize the projected health outcome of planned radiation exposures (*e.g.*, industrial, diagnostic, or therapeutic) in a personalized or population-averaged manner. Furthermore, these methods are entirely compatible with current approaches and limits. This work, taken together, provides a comprehensive methodological framework that could enable a paradigm shift towards more objective and automated approaches to realizing the full beneficial potential of planned exposures.

Chapter 1. Introduction

1.1. Background and Motivation

The principles of medical ethics comprise four main tenets: autonomy, beneficence, non-maleficence, and justice[1]. When considered together, the tenets of beneficence and non-maleficence represent what is known as the Hippocratic Oath, which implores medical practitioners to do no harm. Rarely, however, does there exist a medical intervention free from all risks of harmful side effects. For example, while advancements in non-infectious disease treatments have enabled survival rates to steadily increase in recent decades (*e.g.,* diabetes[2], heart disease[3], and cancer[4]), studies have revealed that the treatments for these diseases can have life-threatening and/or life–altering effects[5-7]. Thus, in practice, medical practitioners aim to ensure that the benefits of the intervention outweigh the risks of harmful side effects, thereby producing some net benefit for the patient[1]. As survival rates continue to rise, however, the number and complexity of potential benefits and detriments is likely to increase as well, thus necessitating new tools to algorithmically consider and balance all major components of the health outcome.

Of these non-infectious diseases, cancer is one of the most significant health-care problems in the world today. It is responsible for 1 in 6 deaths worldwide and is the second leading cause of death in the developed world[8]. In the United States, it is estimated that nearly half of all men and women born today will be diagnosed with some form of cancer in their lifetime[9]. Furthermore, increasing cancer-survival rates have created a large and growing population of cancer survivors, expected to surpass 20 million in the next decade[10]. The majority of cancer survivors received radiation therapy as a part of their care, as it is one of the most commonly used tools in the treatment of cancer[11]. This is largely due to the many benefits of radiation therapy, which include that the treatment is considered safe, effective, and is one of the least invasive of the cancer-

treatment options. As with most medical interventions, however, radiotherapy is not free from risks of side effects.

The side effects with which radiotherapy is linked can be divided into two broad categories: early and late. Early effects of radiotherapy tend to occur during the course of treatment or shortly thereafter and include such effects as bladder toxicity[12], lung pneumonitis[13], and bone fractures[14], to name a few. The late effects of radiotherapy, on the other hand, can occur months, years, or even decades after the completion of treatment and include effects such as second cancer[15], cardiac toxicity[16], and fertility complications[17]. Epidemiological studies on the large and growing population of cancer survivors have revealed that many long-term cancer survivors suffer from one or more of these conditions for the duration of their lifetime[7]. Thus it would appear that the full beneficial potential of radiotherapy cannot be realized without innovative approaches to not only increase rates of tumor cure, but also minimize the myriad long- and short-term harmful side effects[18].

One approach to achieving this is by way of treatment-plan optimization. Most current radiotherapy treatment-planning methods optimize the spatial distribution of absorbed dose in the patient. Absorbed dose, however, is a purely physical quantity and is a poor surrogate for the health outcome[19]. New developments in treatment-plan optimization instead aim to directly optimize the clinical goals of treatment, namely, the patient's health outcome. Early attempts at direct optimization replaced purely dosimetric constraints with biologically-guided dosimetric constraints[20, 21]. More recent work has focused on replacing dosimetric constraints entirely with dose-response functions. The majority of these studies only attempted to consider the early effects of treatment, thereby neglecting the patient's long-term health outcome[22-28]. Relatively less is known about optimizing the late effects of radiotherapy[29-31]. Furthermore, only two of

these studies considered the dose deposited by stray-radiation exposures in the healthy tissues outside of the therapeutic target[29, 32], which contributes to the risk of late effects[15].

1.2. Statement of the Problem

We lack a framework for combining all outcomes (*i.e.,* beneficial and detrimental, long- and short-term, fatal and non-fatal) associated with all of the dose (*i.e.,* therapeutic and stray) in all of the tissues (*i.e.,* diseased and healthy) in individual radiotherapy patients. Doing so necessitates new methods to combine risks of varying types and severity into a single metric and to directly optimize the outcomes. It will also require several new tools to calculate and evaluate the dose from both therapeutic and stray exposures in individual patients. Therefore, the feasibility of improving projected health outcomes (*i.e.,* inclusive of long- and short-term health effects of varying severity) by optimizing them directly, rather than their surrogate (*i.e.,* indirectly with constraints on the distribution of absorbed dose), is currently unknown.

1.3. Objective

The goal of this dissertation was to develop a framework for improving projected health outcomes following radiation exposures in consideration of all health effects, including beneficial and detrimental, early and late, and life-threatening and non-life-threatening effects. We achieved this via practical examples in medicine and occupational radiation protection. For these examples, we first developed tools to close a chronic gap in the knowledge of radiotherapy exposures, namely, the evaluation[33] (Chapter 2) and calculation[34] (Chapter 3) of the absorbed dose from therapeutic- and stray-radiation exposures in individual patients. Next, we designed a generally applicable framework for aggregating all of the beneficial and detrimental effects of planned radiation exposures to individuals, groups, and populations. We demonstrated the utility of this framework in a variety of planned-radiation-exposure settings with three illustrative

example scenarios: emergency response, diagnostic radiology, and cancer radiotherapy[35] (Chapter 4). Finally, we used these new dose-calculation and risk-aggregation tools to directly optimize the health outcomes for a population of prostate-cancer radiotherapy patients. We compared the projected health outcomes for outcome-optimized treatment plans to those for conventionally dose-optimized treatment plans to determine the beneficial potential of these new methods[36] (Chapter 5).

Chapter 2. An Objective Method to Evaluate Radiation Dose Distributions Varying by Three Orders of Magnitude

2.1. Introduction

Modern radiotherapy practices require that the absorbed dose to the patient is accurately predicted to within 5% of the prescribed absorbed dose (D_{Rx}) in order to ensure adequate tumor control and/or ablation of non-cancer disease (*e.g.,* arteriovenous malformation)[37]. Additionally, protecting the surrounding normal tissues from acute injury necessitates the accurate knowledge of the absorbed dose down to the 5-10% dose level, relative to D_{Rx}. Thus, radiotherapy treatment-plan development[38-41] and evaluation[42] typically consider dose magnitudes of 5 to 10% of D_{Rx} and higher. Epidemiological studies, however, have revealed a burgeoning population of long-term cancer survivors[4] who are at risk of serious late-occurring health conditions[7] including second cancer[15], cardiac toxicity[16], and fertility complications[17]. The low-dose exposures from radiotherapy (*i.e.,* below the 5 to 10% relative dose level) are implicated in a number of these side effects[15, 17, 43, 44]. This has spurred the development of various methods for obtaining these out-of-field dose magnitudes, including measurements[45], analytical model calculations[40, 46-50], and Monte Carlo simulations[46, 50-52].

A great deal is known about how to evaluate therapeutic dose distributions (*i.e.,* in regions with dose (D) $\geq 5\%$ of D_{Rx}). Typically, the evaluation approach comprises a comparison of reference and test dose distributions. Metrics like dose difference, distance to agreement, or some combination of these (*e.g.,* the gamma (γ) index) are well understood and widely used for such comparisons[53-55]. Further, for assessing accuracy inside of the therapeutic treatment field, a

---

This chapter was previously published as L.J. Wilson, W.D. Newhauser, C.W. Schneider, "An objective method to evaluate radiation dose distributions varying by three orders of magnitude," Medical Physics **46**, 1888-1895 (2019). Reprinted by permission of John Wiley and Sons.

wealth of literature exists on the level of agreement that can be achieved[42, 56-58]. However, γ -index passing rates vary with the user's selection of agreement criteria, which are selected subjectively[59]. Relatively less is known about how to evaluate doses below the 5% relative dose level. Numerous recent studies reported that γ -index analysis is insensitive to dosimetric discrepancies outside of the therapeutic dose region[60-62]. Our review of the literature did not reveal a method for reliably evaluating the accuracy of dose distributions spanning three orders of magnitude.

The purpose of this study was to develop a method to assess dosimetric agreement that works universally, *i.e.*, in both high- and low-dose regions of distributions spanning three orders of magnitude in dose. To do this, we generalized γ -index analysis methods to include an additional agreement criterion specifically for the low-dose region (*i.e.*, for doses ≤ 5%). We also created an algorithm to objectively select the appropriate magnitudes for each agreement criterion. We then demonstrated this new evaluation method in 1-, 2-, and 3-dimensional dose distributions obtained from measurements, treatment-planning-system calculations, Monte-Carlo simulations, and analytical-model calculations.

2.2. Materials and Methods

2.2.1. Generalized Gamma Index

Traditional γ-index methods utilize a threshold dose, D_{thresh}, below which all data are excluded from analysis. D_{thresh} is typically placed between 5 and 10% of D_{Rx}, thus limiting the scope of applicability[42]. To expand the scope, we generalized traditional γ-index methods. Specifically, we calculated the generalized gamma index, Γ_{G}, for a 1-dimensional comparison by,

$$\Gamma_{\mathrm{G}}(x_{\mathrm{m}}, x_{\mathrm{c}}) = \begin{cases} \sqrt{\dfrac{r^2(x_{\mathrm{m}}, x_{\mathrm{c}})}{\Delta d^2} + \dfrac{{\delta_R}^2(x_{\mathrm{m}}, x_{\mathrm{c}})}{\Delta {D_{\mathrm{R}}}^2}}, \text{ for } x_{\mathrm{m}} \text{ where } D(x_m) > D_{\mathrm{thresh}} \\ \sqrt{\dfrac{r^2(x_{\mathrm{m}}, x_{\mathrm{c}})}{\Delta d^2} + \dfrac{{\delta_A}^2(x_{\mathrm{m}}, x_{\mathrm{c}})}{\Delta {D_{\mathrm{A}}}^2}}, \text{ for } x_{\mathrm{m}} \text{ where } D(x_m) \leq D_{\mathrm{thresh}} \end{cases} \quad 2.1$$

where x_{m} and x_{c} are the locations of measured and calculated dose values, D, respectively. $r(x_{\mathrm{m}}, x_{\mathrm{c}})$ is the difference in location between measured and calculated dose values. This was calculated for all combinations $(x_{\mathrm{m}}, x_{\mathrm{c}})$ by

$$r(x_{\mathrm{m}}, x_{\mathrm{c}}) = |x_{\mathrm{m}} - x_{\mathrm{c}}| \forall \{x_{\mathrm{m}}, x_{\mathrm{c}}\}. \quad 2.2$$

$\delta_{\mathrm{R}}(x_{\mathrm{m}}, x_{\mathrm{c}})$ is the relative difference between measured and calculated dose values at locations x_{m} and x_{c}, computed as

$$\delta_{\mathrm{R}}(x_{\mathrm{m}}, x_{\mathrm{c}}) = \frac{D_{\mathrm{c}}(x_{\mathrm{c}}) - D_{\mathrm{m}}(x_{\mathrm{m}})}{D_{\mathrm{Rx}}}, \quad 2.3$$

where $D_{\mathrm{c}}(x_{\mathrm{c}})$ and $D_{\mathrm{m}}(x_{\mathrm{m}})$ are the calculated and measured absorbed-dose values at x_{c} and x_{m}, respectively. These two factors are identical to those commonly used in traditional γ-index analysis. Additionally, the proposed Γ_{G} in Eq. 2.1 includes $\delta_{\mathrm{A}}(x_{\mathrm{m}}, x_{\mathrm{c}})$, the absolute dose difference between measured and calculated dose values at locations x_{m} and x_{c}, respectively. We calculated this as

$$\delta_{\mathrm{A}}(x_{\mathrm{m}}, x_{\mathrm{c}}) = D_{\mathrm{c}}(x_{\mathrm{c}}) - D_{\mathrm{m}}(x_{\mathrm{m}}) \quad 2.4$$

where $D_{\mathrm{c}}(x_{\mathrm{c}})$ and $D_{\mathrm{m}}(x_{\mathrm{m}})$ are the same as in Eq. 2.3. Finally, Δd, ΔD_{R}, and ΔD_{A}, represent the Γ_{G} agreement criteria of distance to agreement, relative dose difference, and absolute dose

difference, respectively. As in traditional γ-index methods, D_{thresh} in Eq. 2.1 represents the threshold dose, which is used here to discriminate between therapeutic and out-of-field locations. The magnitudes of agreement criteria and the placement of D_{thresh} will be discussed in section 2.2.2.

Following traditional γ-index methods, the final generalized-gamma-index array, $\gamma_{\text{G}}(x_{\text{m}})$, at all locations x_{m} was found by

$$\gamma_{\text{G}}(x_{\text{m}}) = \min\{\Gamma_{\text{G}}(x_{\text{m}}, x_{\text{c}})\}\forall\{x_{\text{c}}\}. \quad 2.5$$

Thus, as with traditional γ-index analysis, a value of $\gamma_{\text{G}}(x_{\text{m}}) \leq 1$ indicates that the result of a comparison at x_{m} is a pass. A value of $\gamma_{\text{G}}(x_{\text{m}}) > 1$ signifies a failure at x_{m}. For the reader's convenience, the corresponding versions of Eqs. 2.1 through 2.5 for 2- and 3-dimensional comparisons are given in Appendix B. Calculating γ_{G} in this way generalizes γ -index methods to universally evaluate the high- and low-dose regions, *i.e.,* all data may be included in the analysis.

2.2.2. Objective Determination of Agreement Criteria

These γ_{G}-index methods include three agreement criteria, two that are used in traditional γ-index analysis, Δd and ΔD_{R}, and an additional criterion, ΔD_{A}. No standard values for this new criterion yet exist. In addition, it cannot be assumed that Δd and ΔD_{R} values from traditional γ-index analysis are appropriate for the generalized method. Thus, we systematically determined the proper magnitudes for all three criteria. Traditionally, γ-index criteria have been determined by manual retrospective analyses of which criteria were achievable at a specified pass rate and D_{thresh} (typically, 90% pass rate with D_{thresh} = 5% of D_{Rx})[63, 64]. Although this method may be used with γ_{G}, we developed an algorithmic approach to determine the agreement criteria that

enables automation and reduces subjectivity. The algorithm determines the set of agreement criteria corresponding to a specified passing rate. The ability to specify an arbitrary passing rate is important because passing-rate requirements vary with the application, *e.g.,* patient care, epidemiological research, and dose-algorithm development.

Our algorithm for determining the γ_{G}-index agreement criteria utilizes a systematic search for the minimum agreement criteria magnitudes that result in the specified passing rate. This search was performed using in-house code written in MATLAB (The MathWorks Inc., version R2016a, Natick, Massachusetts, United States). The systematic search required two inputs: a representative data set and the initial conditions for the search. The former is representative of the dose-determination method (*e.g.,* measurement, treatment planning system (TPS) calculation, Monte Carlo simulation, *etc.*) to which the agreement criteria will be applied. The latter is a set of agreement criteria that are so large such that the initial γ_{G} passing rate surpasses the ultimately specified passing rate. First, the code iteratively and monotonically reduced the agreement criteria values by steps of 0.05 mm, 0.05%, and 0.05 mGy/Gy for Δd, ΔD_{R}, and ΔD_{A}, respectively. The code flagged all combinations of agreement criteria that resulted in the specified passing rate or higher. Each flagged set of agreement criteria was assigned an overall score according to,

$$S = \left(\frac{\Delta d_i}{\Delta d_{\mathrm{min}}}\right) \times \left(\frac{\Delta D_{\mathrm{R},i}}{\Delta D_{\mathrm{R,min}}}\right) \times \left(\frac{\Delta D_{\mathrm{A},i}}{\Delta D_{\mathrm{A,min}}}\right) \qquad 2.6$$

where Δd_i, $\Delta D_{\mathrm{R},i}$, and $\Delta D_{\mathrm{A},i}$ are the distance-to-agreement, relative-dose-difference, and absolute-dose-difference criteria magnitudes in the i^{th} set of flagged agreement criteria. Δd_{min}, $\Delta D_{\mathrm{R,min}}$, and $\Delta D_{\mathrm{A,min}}$ are the minimum magnitudes of each criterion amongst those in the list of

all flagged combinations. Next, the list of scored sets of agreement-criteria triplets were sorted in order of ascending score. The final result was the set of agreement criteria with the lowest score.

In addition to these three criteria, the γ_{G}-index method requires the user to select D_{thresh} (See Eq. 2.1). This threshold was represented as a percentage of D_{Rx}. Following current clinical practice, we used $D_{\mathrm{thresh}} = 5\%$ of D_{Rx}. To confirm that our results were insensitive to our selection of D_{thresh}, we additionally calculated passing rate as a function of D_{thresh}.

2.2.3. Demonstration of New Methods

In order to demonstrate the new γ_{G}-index method, we performed an example of the analysis method in two steps. First, we demonstrated the use of our algorithm for determining γ_{G}-index agreement criteria for a set of measured and calculated dose profiles. Second, we used the new γ_{G}-index method to perform three example evaluations: one 1-dimensional comparison of dose profiles (independent from those used in determining the agreement criteria), one 2-dimensional comparison of dose planes, and one 3-dimensional comparison of dose volumes. In each case, we performed both traditional- and generalized-gamma-index analyses. We designed this demonstration to be of relevance to clinical, research (*e.g.,* epidemiological studies), and development (*e.g.,* dose-algorithm development) applications. The following sections contain details on each of these steps and the data used for this demonstration.

2.2.3.1 Determination of Agreement Criteria.

We used the systematic-search algorithm (see Section 2.2.2) to find the agreement criteria corresponding to four specified passing rates (100%, 95%, 90%, and 67.5%). The 100% passing rate corresponds to the agreement criteria that accommodate the maximum discrepancy between reference and test dose magnitudes, *i.e.*, all data agree within these criteria. The 90% pass rate is commonly used to evaluate clinical therapeutic dose distributions[42]. Finally, 95% and 67%

passing rates conveniently correspond to 2-σ and 1-σ confidence intervals, respectively. The initial guesses of agreement criteria were Δd of 50 mm, ΔD_R of 10%, and ΔD_A of 20 mGy for the pass rate of 100% (γ_{G}-index analysis confirmed a 100% γ_{G} passing rate). The initial guesses for the searches at the next lower passing rate were the resulting agreement criteria from the next larger passing rate (*e.g.*, initial guesses for a systematic search for criteria corresponding to a 95% passing rate were the results of the search for a 100% passing rate, *etc.*).

2.2.3.2 Example Gamma-Index Evaluations

Table 2.1 contains the agreement criteria, D_{thresh}, and test passing rate used for 1-, 2-, and 3-dimensional γ- and γ_{G}-index evaluations. It should be noted that traditional γ-index comparisons used only ΔD_R, Δd, and D_{thresh}, while the γ_{G}-index comparisons additionally used ΔD_{A}.

Table 2.1. Parameters for example gamma- and generalized-gamma-index evaluations. Parameters include the agreement criteria (*i.e.,* relative dose difference, ΔD_R, absolute dose difference, ΔD_{A}, distance to agreement, Δd), threshold dose, D_{thresh}, and the test passing rate.

	ΔD_R [%]	ΔD_{A} [mGy][1]	Δd [mm]	D_{thresh} [%]	Test Passing Rate [%]
1-D	3.0	0.8	3.0	5.0	≥90
2-D	4.6	0.8	0.5	5.0	≥90
3-D	3.0	0.8	3.0	5.0	≥90

[1]used for γ_{G}-index comparisons only

2.2.3.3 Reference and Test Absorbed Dose Distributions.

We acquired the data for this study by four methods: measurement, treatment-planning-system calculation, Monte-Carlo simulation, and analytical-model calculation. Measured dose profiles were previously published by Kaderka *et al*.[65] The measurements utilized in this study were performed on an electron linear accelerator (Elekta SL25, Stockholm) equipped with an MLCi2 at Universitätsklinikum (KGU) in Frankfurt, Germany operated at 6 MV. Kaderka *et al.* measured photon doses to a distance of 40 cm from the beam central axis (CAX) with a 1.03-mm spatial resolution using a diamond detector (60003 PTW, Freiburg) in a water-tank phantom

(PTW, Freiburg) and reported a maximum relative uncertainty of 9%. These data were used as the reference data in the systematic search for appropriate agreement criteria and in the γ- and γ_G-index evaluations of a 1-dimensional absorbed dose profile.

We used one commercial TPS (Eclipse, Varian Medical Systems, Palo Alto, CA) and one research TPS (CERR)[66] in this study. The commercial TPS was commissioned for the electron linear accelerator (Elekta Synergy, Stockholm) equipped with an MLCi2 at Mary Bird Perkins Cancer Center in Baton Rouge, Louisiana and provided the test data for the 1-dimensional evaluations. Prior to these evaluations, we took steps to confirm that the commercial TPS was suitably commissioned for calculating beams from the treatment unit measured by Kaderka *et al.* for the purposes of this manuscript (*i.e.,* average dose difference of 1.5% and 0.4 mGy/Gy in the high- and low-dose regions, respectively). The dose grid for these TPS calculations extended to a distance of 40 cm from the beam CAX in the in- and cross-plane directions with a resolution of 0.5 x 0.5 x 0.5 cm^3. The commercial TPS, however, only calculated non-zero dose magnitudes to a distance of 16.5 cm from the beam CAX. Only this non-zero dose region was included in the example comparison. The research TPS, CERR, provided the test data for the 3-dimensional evaluations with a 1 x 1 x 1-cm^3 grid resolution covering the entire imaged patient anatomy (axial distance of 30 cm). Additionally, we created an extended version of CERR that includes dose calculations in the low-dose region based on the analytical model of Schneider *et al.*[67] This extended version of CERR provided the reference data for the 3-dimensional evaluations with a 0.10 x 0.10 x 0.25-cm^3 grid resolution also covering the entire imaged anatomy. The 3-dimensional dose distributions were calculated for a single AP photon beam to the prostate in a patient previously treated at our institution (Mary Bird Perkins Cancer Center, Baton Rouge).

Monte Carlo simulations of absorbed dose were performed using the Monte Carlo N-Particle eXtended (MCNPX) transport code version 2.7[68]. The MCNPX model was designed based on design information for an Elekta Precise medical linear accelerator equipped with an Agility MLC provided by the manufacturer. The phantom used in the simulations was a homogeneous water box measuring 120 cm x 120 cm in the plane perpendicular to the beam central axis (CAX) and 30 cm deep in the plane parallel to the beam CAX. Photons and electrons were transported and F6 lattice tallies for each particle type were used to determine the energy deposited in each 1.0 x 1.0 x 1.0-cm^3 voxel in the phantom extending to a distance of 20 cm from the beam CAX in the in- and cross-plane directions. We utilized high-performance-parallel-computing resources at Louisiana State University to simulate 10^9 electrons on target on 256 CPU-cores resulting in an average statistical fluctuation of 6.9%. These data were used for the reference dose plane in the 2-dimensional comparison.

We used an analytical absorbed dose model[40, 67] to generate the test data for both the determination of appropriate agreement criteria and the 2-dimensional γ- and γ_G-index evaluations. This model was previously trained and validated for an Elekta SL25 medical linear accelerator (see above) with a reported average uncertainty of 9.9%[67]. We used this model to calculate absorbed dose with a spatial resolution of 0.1 cm to a distance of 50 cm from the beam CAX.

Table 2.2 lists the configuration details for all reference and test data sets used in this study. Different sources of reference and test data were used for each comparison to provide representative examples of a variety of research and future clinical applications of the generalized-gamma-index method. The example agreement-criteria determination is representative of using this method in the research setting to characterize the accuracy of a new

dose-calculation algorithm. The one-dimensional evaluation provides a representative example of a possible future clinical application of this method to compare measurements and commercial TPS calculations. The two-dimensional evaluation is representative of using this method in the research setting to test the accuracy of an analytical model during algorithm development. Finally, the three-dimensional example is representative of a research application of this method to the clinical translation and commercialization of a new dose-calculation algorithm. Figure 2.1 shows a representative example of reference and test data used in the systematic search for appropriate agreement criteria. Figure 2.2 shows the reference and test dose distributions used for 1-, 2-, and 3-dimensional γ- and γ_G-index analyses.

Table 2.2. Configuration for all reference and test data used for the demonstration of generalized-gamma-index methods. Details include the square field size, source-to-surface distance (SSD), depth in water, profile orientation (in plane or cross plane), and the source of data.

Agreement Criteria Determination					
Field Size (cm^2)	SSD (cm)	Depth (cm)	Orientation	Source of Reference Data	Source of Test Data
5x5	100	1.5	In-Plane Profile	Measurement[65]	Analytical Model[40]
5x5	100	1.5	Cross-Plane Profile	Measurement[65]	Analytical Model[40]
5x5	100	10	In-Plane Profile	Measurement[65]	Analytical Model[40]
10x10	100	1.5	In-Plane Profile	Measurement[65]	Analytical Model[40]
10x10	100	1.5	Cross-Plane Profile	Measurement[65]	Analytical Model[40]
Example Evaluations					
10x10	100	1.5	Cross-Plane Profile	Measurement[65]	Commercial TPS (This work)
10x10	100	1.5	2-Dimensional Plane	Monte Carlo (This work)	Analytical Model[67]
6.5x6.5	94.8	N/A	3-Dimensional Volume	Extended CERR (This work)	CERR[66]

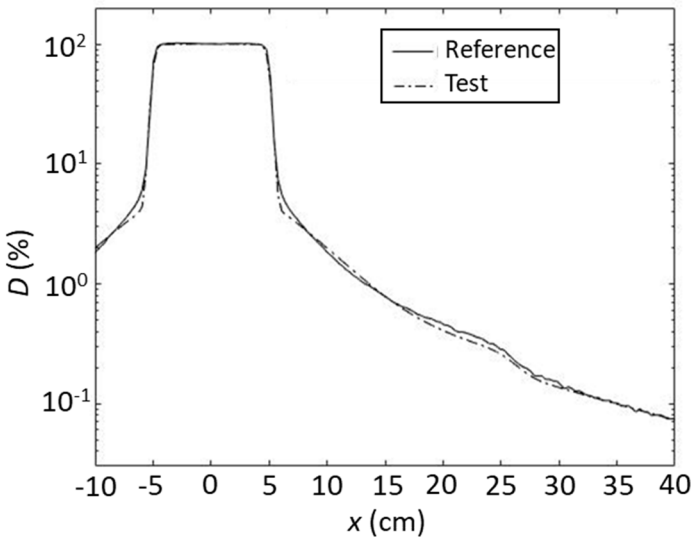

Figure 2.1. Representative example of reference and test profiles for the systematic search for appropriate agreement criteria. Absorbed dose, *D,* versus off-axis distance, *x*, for a 10x10 cm^2, 6-MV photon field at a depth of 1.5 cm in a homogeneous water-box phantom in the cross-plane direction. Reference data were measured[65] and test data were calculated using an analytical model[40] (See Table 2.2).

2.3. Results

2.3.1. Determination of Agreement Criteria

Using the systematic-search method described in Section 2.2.2, we found the agreement criteria listed in Table 2.3. These results show that the appropriate agreement criteria are generally sensitive to the selected passing rate. More specifically, the magnitudes of the agreement criteria are inversely related to the passing rate. The information contained in Table 2.3 demonstrates the advantages of the systematic-search method over *a priori* user-selection of criteria; namely that the passing rate may be largely an artifact of the subjectively selected criteria. Thus, *a priori* selection provides limited information on algorithm performance. By the proposed method, one may obtain a more complete picture of the performance envelope of the algorithm in question.

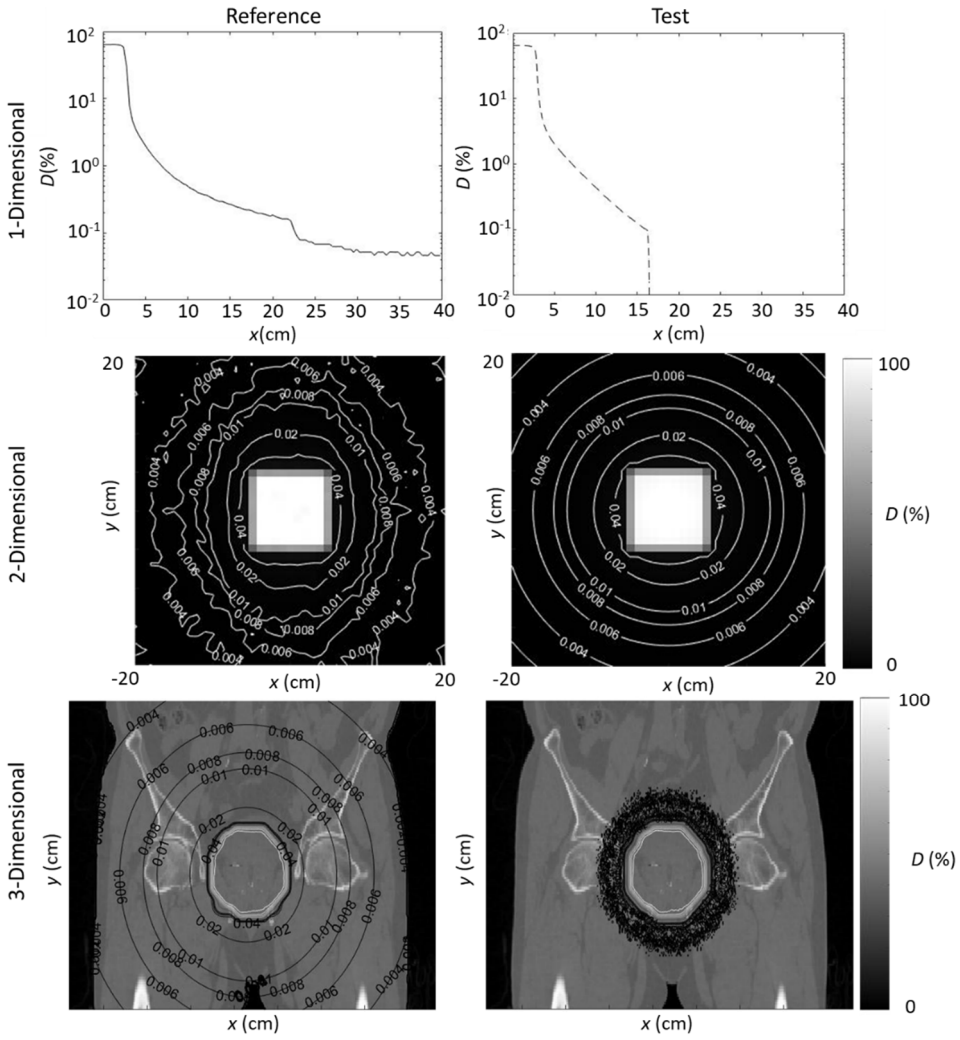

Figure 2.2. Reference and test data used for gamma- and generalized-gamma-index analyses in 1, 2, and 3 dimensions.

Table 2.3. Agreement criteria found by the systematic search for four selected passing rates. Results are based on the analysis of data listed in the top section of Table 2.2 and plotted in Figure 2.1. Criteria include distance to agreement (Δd), relative dose difference (ΔD_{R}), and absolute dose difference (ΔD_{A}).

Passing Rate	Δd (mm)	ΔD_{R} (%)	ΔD_{A} (mGy)
100%	3.7	9.1	9.6
95%	1.0	5.2	1.6
90%	0.5	4.6	0.8
67.5%	0.5	1.6	0.2

2.3.2. Example Evaluations

Table 2.4 lists the passing rates for 1-, 2-, and 3-dimensional γ- and γ_G-index evaluations. Each of these reference and test data pairs contained known discrepancies outside of the therapeutic treatment field due to clinically-realistic errors. Discrepancies in the 1- and 3-dimensional dose distributions resulted from the significant underestimation of stray dose by the treatment planning systems[38-41]. These discrepancies were so severe and widespread in the 3-dimensional dose distributions that only 1.05% of the low-dose region passed the generalized-gamma-index analysis. This, combined with the fact that the low-dose region comprised 93% of the total volume considered, resulted in the strikingly lower γ_G-index passing rate for this test. Discrepancies in the 2-dimensional dose distribution resulted from the fact that we calculated the reference and test dose distributions for different treatment machines with different MLC models (See Section 2.2.3.3). γ-index analysis only looks at the region where $D(x) \geq D_{\text{thresh}}$, rendering it insensitive to these discrepancies. This led to test results of "pass" in each case, despite the discrepancies. γ_G-index, on the other hand, looks at the entire dose distribution and correctly resulted in a passing rate considerably lower than 90% and a "fail" of all three tests.

Table 2.4. Passing rates for gamma- and generalized-gamma-index analyses. See Table 2.1 for corresponding test criteria.

	Traditional Gamma Index		Generalized Gamma Index	
Evaluation	γ Passing Rate	Test Result	γ_G Passing Rate	Test Result
1-dimensional	100%	Pass	55.4%	Fail
2-dimensional	97.8%	Pass	44.5%	Fail
3-dimensional	96.4%	Pass	8.9%	Fail

2.4. Discussion

We developed a generalized gamma-index-analysis method in 1-, 2-, and 3-dimensions. The major finding of this study is that the proposed γ_G-index method provides a reliable and objective assessment of the agreement of distributions spanning three orders of magnitude in absorbed

dose. In particular, this new method correctly characterized dosimetric errors in the lowest dose region, which are excluded by traditional γ-index methods[60-62]. We also proposed a method for objectively determining the appropriate γ_{G}-index agreement criteria at any specified passing rate using an algorithmic approach. This new method comprises a more systematic approach with lowered requirements for user skill and subjective judgement.

Traditional γ-index analysis methods exclude all dose magnitudes <5% of D_{Rx}. Our study suggests that it is possible to evaluate the accuracy of dose distributions spanning multiple orders of magnitude with a single, universal method. The proposed γ_{G}-index method could find use in a variety of scientific and development applications. For example, to study the long-term side effects of radiotherapy treatments, radiation epidemiologists require methods to calculate the absorbed dose everywhere in the patient, not just in the therapeutic dose region. Moreover, an understanding of the uncertainties associated with these dose magnitudes can be just as important in these studies as the doses themselves. Thus, the proposed γ_{G}-index method could find utility in developing and benchmarking the required dose algorithms. Additionally, the method for the objective determination of γ_{G}-index agreement criteria enables a more complete description of the envelope of agreement, elucidating vital information about the associated uncertainties.

Our findings are in good agreement with previous γ-index studies in the literature. Nelms *et al.*[62] and Zhen *et al*.[61] studied the sensitivity of passing-rate to patient dose errors for 2- and 3-dimensional γ-index analyses, respectively. In each of these studies, the authors simulated increased and decreased MLC transmission in a dose calculation and assessed whether traditional gamma-index methods were sensitive to these errors. Nelms *et al.* concluded that there was no correlation between γ passing rates and the introduced errors while Zhen *et al.* found negligible to weak correlations. Much like these previous studies, the MLC transmission differed between

our reference and test 2-dimensional dose distributions. Similarly, our traditional γ-index test still passed despite these errors, adding to the growing body of evidence showing the insensitivity of traditional γ-index analysis to dosimetric errors outside of the therapeutic treatment field[60-62].

In this study, we showed for the first time that it is possible to simultaneously evaluate high- and low-dose regions of a dose profile spanning three orders of magnitude using a universal method. The major strength of this study was that it utilized the well-established and widely used γ-index analysis at doses above the threshold dose level, providing coherence with previous works and consistency with current clinical practices. Another strength of this study is that it demonstrated evaluations of 1-, 2-, and 3-dimensional dose distributions in both simple (*i.e.,* water-box phantom) and clinically-realistic geometries.

This study has several limitations. One limitation is that we only demonstrated the new method on single-field, conventional dose distributions. This is not a serious limitation because a study by Nelms *et al*. found that the majority of clinics perform field-by-field analysis in patient-specific quality assurance tests rather than composite analysis[42]. Further, the purpose of this work was to develop and demonstrate the ability of the new method to overcome limitations of hitherto methods, not to conclusively characterize any particular dose distribution. Future work, however, should examine the application of the proposed method to additional treatment types (*e.g.*, IMRT, *etc.*) and for measurements taken in other QA phantoms (solid water, anthropomorphic phantom, *etc.*).

2.5. Conclusion

The new method developed in this study enables the analysis of 1-, 2-, and 3-dimensional dose distributions across three decades of absorbed dose. Additionally, we proposed an objective,

algorithmic procedure for determining the appropriate agreement criteria, *e.g.*, relative and absolute dose difference and distance to agreement. The demonstration of the γ_{G} analysis method revealed that the new γ_{G} method is capable of simultaneously evaluating the agreement of dose distributions spanning three orders of magnitude in both high- and low-dose regions. Moreover, the results were insensitive to the user-selected D_{thresh}.

Recent interest in understanding and mitigating the long-term side effects of radiotherapy treatments has led to the emergence of numerous whole-body-dose calculation methods, such as analytical algorithms and Monte Carlo simulations. A standardized method of meaningfully assessing dosimetric accuracy throughout the whole human body (*i.e.,* high- and low-dose magnitudes) is required to assess and compare the accuracy of these dose algorithms. The generalized-gamma-index method proposed here could initially find utility in a variety of research applications including dose algorithm development and translation, as well as in epidemiological studies on radiation toxicities. Furthermore, continued interest in improving long-term patient health outcomes will likely lead to the clinical implementation of such dose algorithms, at which point this same method could also be applied to clinical tasks including patient-specific quality assurance and machine commissioning.

Chapter 3. Method to Quickly and Accurately Calculate Absorbed Dose from Therapeutic and Stray Photon Exposures throughout the Entire Body in Individual Patients

3.1. Introduction

Increasing cancer survival rates in the United States have created a large and growing population of cancer survivors, which is expected to number over 20 million in the next decade[10]. Epidemiological research on this population has revealed that the majority of long-term cancer survivors are at a heightened risk for health complications as a result of their primary disease and/or treatment[7, 69]. Nearly two-thirds of these survivors will have received radiation therapy as a part of their care[11] and the vast majority of these radiotherapy treatments will have been performed with megavoltage photon therapy[70]. Photon treatment techniques typically devote considerable attention to limiting the exposure of healthy tissues outside of the intended treatment volume[71]. Nonetheless, small levels of unwanted stray radiation reach the patient's entire body, which increase the risk of late effects, including second cancer[72], cardiac toxicity[16], and fertility complications[17]. Of these late effects, perhaps the most extensively studied is second cancer[73]. Second malignancies occur most frequently outside of the volume treated for the primary cancer with peak frequency in volumes which received < 2.5 Gy[43].

Despite strong evidence of the importance of stray radiation to patient outcomes[74, 75], commercial Treatment Planning Systems (TPS's) significantly underestimate the total absorbed dose outside of the therapeutic treatment field[38-41, 76]. Figure 3.1 shows a representative example of just how poorly these doses are known clinically. The shaded area represents the region in which one study observed nearly a quarter of all reported second malignant neoplasms[43]. This figure reveals that the shaded area corresponds to the region where the commercial TPS's underestimate or

neglect the absorbed dose. Thus, these exposures, and the risks they incur, are not explicitly considered in the treatment-planning process.

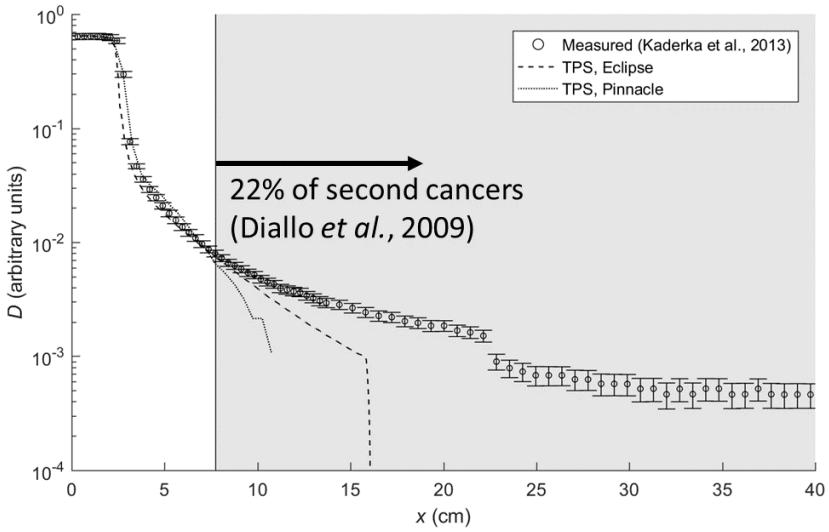

Figure 3.1. Dosimetric limitations of commercial treatment planning systems. Total absorbed dose (D) versus distance from the beam central axis (x) from two contemporary commercial TPS's compared to measurements. Measurements and calculations are for a 5x5 cm^2, 6-MV photon field at 10-cm depth in a water-box phantom at 100 cm source-to-surface distance. The grey-shaded region represents the region in which Diallo *et al*. observed 22% (25 of 115) of reported second cancers[43].

This has led to the emergence of numerous alternative methods for quantifying out-of-field doses from photon radiotherapy including measurements[65, 77], Monte Carlo simulations[46, 52, 78], and analytical models[40, 46, 47, 74, 75, 79-81]. Of these, measurements are considered the gold standard in accuracy. However, the time required for obtaining high-quality, patient-specific measurements render this method impractical for routine clinical implementation. Monte Carlo dose models are the most physically realistic and dosimetrically accurate of the calculation methods. This has made them a popular tool for research groups focused on treatment planning using whole-body dose calculations[75, 82]. Despite these clear advantages, complete Monte Carlo dose models tend to be highly complex to develop and calibrate, a task which often requires proprietary information regarding the radiation treatment machines. Furthermore, they require long computation times to

converge on a solution and achieve acceptably low statistical fluctuations, especially outside of the therapeutic treatment field. These and other factors decrease the feasibility of implementing Monte-Carlo methods into the clinical treatment-planning workflow as a whole-body-dose calculation tool. Analytical models, on the other hand, are comparatively simple and fast[40]. There is also promising evidence suggesting they can be dosimetrically accurate in the out-of-field region[40, 49, 67, 75, 79, 83]. Further, a recently published analytical model is readily generalizable to different treatment machines and irradiation conditions without the need for proprietary information due to its physics-based framework[40, 67]. It is not known, however, if such algorithms could be implemented into a TPS to quickly and accurately predict the otherwise missing out-of-field dosimetric information.

The purpose of this study was to test the feasibility of quickly and accurately calculating the total absorbed dose to the whole body in individual patients receiving photon radiotherapy. To accomplish this, we implemented a physics-based analytical dose model into a research TPS and assessed the dosimetric accuracy by comparing results to measured total absorbed dose in water-box and anthropomorphic phantoms. We also characterized the additional computation time required for whole-body dose calculations.

3.2. Methods

In this study, we implemented a physics-based analytical model following the methods of Schneider *et al.*[67] into a TPS. For the reader's convenience, we briefly review the analytical model (Section 3.2.1) before describing how we implemented it as an extension to the research TPS (Section 3.2.2). We detail how we configured the extended TPS for calculating whole-body doses from 6- and 15-MV photon radiotherapy exposures in a water-box phantom (Section 3.2.3) and validated it in water-box (Section 3.2.4) and adult-male anthropomorphic phantoms (Section

3.2.5). Finally, we describe methods to measure the computation time required for a whole-body dose reconstruction using the extended TPS (Section 3.2.6).

3.2.1. Analytical Model for Total Absorbed Photon Dose

We modeled the total absorbed dose from therapeutic and stray photon sources during photon radiotherapy, D_{T}, as the sum of four terms following Schneider, *et al.*[67], or

$$D_{\mathrm{T}} = D_{\mathrm{P}} + D_{\mathrm{HS}} + D_{\mathrm{PS}} + D_{\mathrm{L}} \qquad 3.1$$

where D_{P} denotes the primary therapeutic dose, D_{HS} is the dose from head-scattered photons, D_{PS} is the dose from photons that scattered in the phantom or patient, and D_{L} is the dose from leakage photons. Each term in Eq. 3.1 contained separate functions to characterize the photon attenuation and scattering in the treatment unit and in the phantom or patient. This model was specifically designed for ease and simplicity of configuration, (*i.e.,* all configuration data can be quickly measured in most clinics and proprietary information is not used). A complete description of the model's components and fitting parameters was given elsewhere[67].

3.2.2. Implementation of the Analytical Model into a Research TPS

We implemented the analytical model for total absorbed dose from therapeutic- and stray-photon radiation exposures (see Eq. 3.1) in the treatment-planning module of the Computational Environment for Radiotherapy Research (CERR version 5.2)[66] using MATLAB (The MathWorks Inc., version 2014a, Natick, Massachusetts, United States), thus creating an extended version of CERR henceforth referred to as CERR-LSU. To do this, we used a bridging technique to combine the dose distributions from CERR and the analytical model into a single CERR-LSU dose distribution.

The bridging technique divided the exposed volume into three distinct regions: in-field, near-field, and far-from-field. The in-field region comprised all locations where the dose calculated by the TPS (in this case CERR) was ≥ 50% of the prescribed dose (D_{Rx}). The far-from-field region included locations where the total absorbed dose calculated by the TPS was ≤ 5% of D_{Rx}. The near-field region included all remaining locations, or those locations where the TPS-calculated dose was between 50% and 5% of D_{Rx}. Figure 3.2a shows a schematic illustration of these three regions.

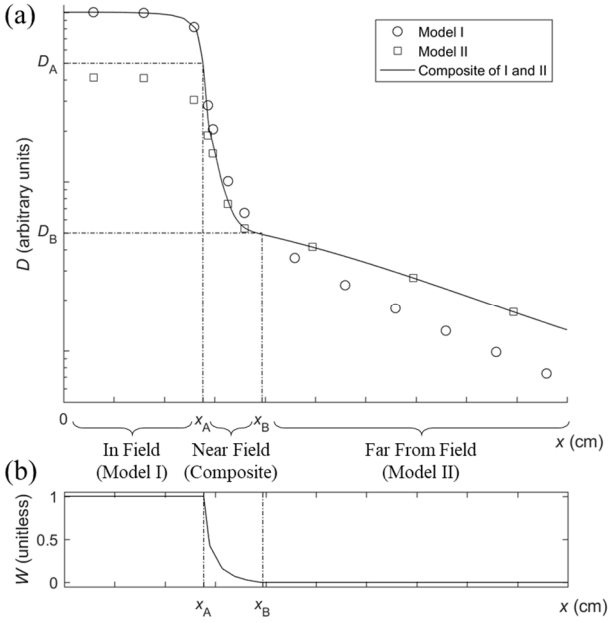

Figure 3.2. Schematic illustration of the bridging method to composite dose distributions from two models. (a) Plot of the relative absorbed dose, D, versus position, x, where x_A is the location at which Model I (i.e., CERR) reached the D_A relative-dose level (i.e., 50%) and x_B is the location at which Model I reached the D_B relative-dose level (i.e., 5%). x_A separated the in- and near-field regions and x_B discriminated between the near- and far-from-field regions (b) Plot of weight given to Model I, W, versus position, x, corresponding to the example of the bridging technique shown in panel (a) (see Eq. 3.3).

The dose matrix in CERR-LSU comprised three regions. Doses in the in-field region came from CERR, those in the far-from-field region came from the analytical model, and doses in the near-

field region were calculated as a weighted sum of the two dose calculations, as depicted in Figure 3.2a. Algorithmically,

$$D_{\text{CERR-LSU}} = D_{\text{CERR}} \times W + D_{\text{AM}} \times [1 - W] \tag{3.2}$$

where $D_{\text{CERR-LSU}}$ is the CERR-LSU dose, D_{CERR} is the dose calculated by CERR, D_{AM} is the dose from Eq. 3.1 (*i.e.,* D_{T}) of the analytical model, and W is a weighting factor calculated by,

$$W = \begin{cases} 1 & \text{for } D_{\text{CERR}} \geq 50\% \times D_{\text{Rx}} \\ \left(\dfrac{D_{\text{CERR}}(\%) - 5\%}{50\% - 5\%}\right) & \text{for } 5\% \times D_{\text{Rx}} < D_{\text{CERR}} < 50\% \times D_{\text{Rx}} \\ 0 & \text{for } D_{\text{CERR}} \leq 5\% \times D_{\text{Rx}} \end{cases} \tag{3.3}$$

where all parameters are as previously defined. Figure 3.2(b) shows a representative example of W.

3.2.3. CERR-LSU Configuration

We configured CERR-LSU to calculate the absorbed dose from a medical linear accelerator (Elekta Precise, SN: 1605, Stockholm, Sweden) at the Physikalisch-Technische Bundesanstalt (PTB) in Braunschweig, Germany (Electron Accelerator Facility, Dosimetry for Radiation Therapy and Diagnostic Radiology, High-Energy Photon and Electron Radiation, Group 6.21). The primary task in configuring CERR-LSU was to determine the magnitudes of the 28 empirical parameters in the analytical model. To do this, we followed the methods of Schneider *et al.*[67] and utilized a commercially available optimization toolbox (MATLAB version R2016a, The MathWorks Inc., Natick, Massachusetts, United States) to perform a least-squares fit of the analytical model to total-absorbed-dose profiles measured in a water-box phantom.

Due to limitations of the documentation available on the research platform CERR, we were unable to commission the treatment-planning module for our linear accelerator (*i.e.,* to input measured dose profiles). To overcome this limitation, we applied a multiplicative correction factor (C) to the doses initially calculated by CERR, $D_{\mathrm{CERR,O}}$, such that the corrected relative-depth-dose curve on the beam central axis (CAX) matched the respective measured curve, D_{measured}, for each field size. More specifically,

$$D_{\mathrm{CERR}}(x,y,d) = D_{\mathrm{CERR,O}}(x,y,d) \times C(d) \tag{3.4}$$

where D_{CERR} was the corrected dose (*i.e.,* that used in Eqs. 3.2 and 3.3) and C was empirically found such that

$$D_{\mathrm{CERR,O}}(0,0,d) \times C(d) = D_{\mathrm{measured}}(0,0,d), \tag{3.5}$$

where,

$$C = \begin{cases} \left(9 \times 10^{-6} \times \dfrac{4A}{P} - 2 \times 10^{-4}\right) \times d + \left(-1 \times 10^{-5} \times \dfrac{4A}{P} + 1\right) & \text{for 6-MV photon beams} \\ \left(2 \times 10^{-6} \times \dfrac{4A}{P} + 3 \times 10^{-4}\right) \times d + \left(3 \times 10^{-5} \times \dfrac{4A}{P} + 1\right) & \text{for 15-MV photon beams,} \end{cases} \tag{3.6}$$

where d was the depth in mm, and A and P were the collimated field area and perimeter in mm, respectively, defined at isocenter.

Table 3.1 lists the measurement conditions used to configure the analytical model. We performed all measurements in a 60x60x60-cm^3 water-box phantom at a source-to-surface distance (SSD) of 90 cm for 6- and 15-MV photon beams. We used a diamond detector (PTW TM60019 SN: 122240, Freiburg) for measurements in the in- and near-field regions to achieve high spatial resolution in areas of steep dose gradient (*e.g.,* the penumbra). The relatively lower signal in the

far-from-field region necessitated a large-volume detector and thus we used a farmer-type chamber (IBA FC65-G SN: 3068, Louvain-la-Neuve) for measurements in this region. We corrected the measurements made with the diamond detector for dose-rate effects following the methods of Laub *et al.*[84] We corrected the farmer-chamber measurements for variations in photon spectral fluence with measurement location following the methods of Chofor *et al.*[85, 86]

Table 3.1. Measurement conditions for the profiles used to configure and validate CERR-LSU in a water-box phantom. Conditions include square field size, depth in water, scan direction, and the purpose of the measurement (i.e., model configuration or validation). All profiles were measured for 6- and 15-MV photon beams in a 60x60x60-cm^3 water-box phantom at 90-cm SSD using a diamond detector and a farmer chamber.

Field Size (cm^2)	Depth in Water (cm)	Scan Direction	Purpose
2x2, 4x4, 10x10, 20x20	3.5, 10, 40	In plane	Configuration
”	”	Cross plane	”
”	-	Depth dose	”
2x2, 4x4, 10x10, 20x20	20	In plane	Validation
”	”	Cross plane	”
14x14, 20x5	3.5, 10, 20, 40	In plane	”
”	”	Cross plane	”
”	-	Depth dose	

We performed two tests to characterize the dosimetric accuracy compared to the measurements used to configure the model (see Table 3.1). First, we calculated the relative local dose differences (dD_{R}) in the in- and near-field regions and the absolute local dose differences (dD_{A}) in the far-from-field region for both CERR and CERR-LSU. From these, we calculated the average, root-mean-square (RMS), median, and maximum local dose differences between measured and calculated dose magnitudes. Second, we determined the appropriate generalized-gamma-index agreement criteria for CERR-LSU corresponding to four selected passing rates (67.5%, 90%, 95%, and 100%) following the methods of Wilson *et al.*[33] (see Chapter 2). The generalized gamma index provides a universal method of assessing the dosimetric accuracy of dose distributions spanning three orders of magnitude. It is calculated according to

$$\Gamma_{\mathrm{G}}(x_{\mathrm{m}}, x_{\mathrm{c}}) = \begin{cases} \sqrt{\dfrac{r^2(x_{\mathrm{m}}, x_{\mathrm{c}})}{\Delta d^2} + \dfrac{{\delta_R}^2(x_{\mathrm{m}}, x_{\mathrm{c}})}{{\Delta D_{\mathrm{R}}}^2}}, \text{ for } x_{\mathrm{m}} \text{ at in- and near-field locations} \\ \sqrt{\dfrac{r^2(x_{\mathrm{m}}, x_{\mathrm{c}})}{\Delta d^2} + \dfrac{{\delta_A}^2(x_{\mathrm{m}}, x_{\mathrm{c}})}{{\Delta D_{\mathrm{A}}}^2}}, \text{ for } x_{\mathrm{m}} \text{ at far-from-field locations} \end{cases} \quad 3.7$$

where $r^2(x_{\mathrm{m}}, x_{\mathrm{c}})$ is the difference between measured, x_{m}, and calculated, x_{c}, locations, respectively, (*i.e.,* distance to agreement). ${\delta_R}^2(x_{\mathrm{m}}, x_{\mathrm{c}})$ is the relative dose difference and ${\delta_A}^2(x_{\mathrm{m}}, x_{\mathrm{c}})$ is the absolute dose difference between measured and calculated dose magnitudes at locations x_{m} and x_{c}, respectively. Δd, ΔD_R, and ΔD_A are the criteria of distance to agreement, relative dose difference, and absolute dose difference, respectively. In-, near-, and far-from-field regions are defined as in Section 3.2.2. A more complete description of this method and examples of its use are given elsewhere[33] (see Chapter 2).

3.2.4. Validation in a Water-Box Phantom

We validated the dosimetric accuracy of CERR and CERR-LSU calculations of 6- and 15-MV photon-therapy beams in a water-box phantom by comparison to measurements. These measurement conditions were intentionally distinct and different from those used to configure CERR-LSU and are listed in Table 3.1. Specifically, we measured at different therapeutic field sizes, aspect ratios, and depths in water compared to the configuration data. These measurements utilized the same medical linear accelerator, water-box phantom, and detectors as previously described (see Section 3.2.3). We characterized the dosimetric accuracy compared to measurements for validation in a water-box phantom in a manner similar to that described in Section 3.2.3. Specifically, the first test was the same. For the second test, we found the generalized-gamma-index passing rates for CERR and CERR-LSU compared to validation

measurements following the methods of Wilson *et al.*[33] (see Chapter 2 and Eq. 3.7). The generalized-gamma-index agreement criteria for these comparisons were 4.5% relative dose difference, 3.8 mGy/Gy absolute dose difference, or 1.25 mm distance to agreement.

3.2.5. Validation in Clinically Realistic Anatomy

In order to validate CERR-LSU in more clinically realistic anatomy, we delivered a 4-field-box prostate treatment to an adult-male anthropomorphic phantom (ATOM® Adult Male model 701, Computerized Imaging Reference Systems, Inc., Norfolk, Virginia). We chose to simulate a prostate treatment because the location of the target volume near the lower end of the anthropomorphic phantom placed several organs at risk (*e.g.*, lens of eye, brain, *etc.*) at a large distance from the target volume, thereby providing an extreme test of the extended TPS's far-from-field dosimetric accuracy. We selected a 4-field box treatment because the relative simplicity of the treatment plan facilitated treatment planning and delivery in the research setting. The treatment plan consisted of four 8x8-cm^2 photon fields (*i.e.,* anterior-posterior (AP), posterior-anterior (PA), left lateral (LL), and right lateral (RL)) delivered isocentrically with equal weights. We calculated the total absorbed dose from this treatment plan using both CERR and CERR-LSU for 6- and 15-MV photons. Figure 3.3 shows representative examples of the dose distributions from these calculations.

We compared the dose distributions calculated by CERR and CERR-LSU to measurements in the anthropomorphic phantom. We delivered the treatment plan to the anthropomorphic phantom using the same linear accelerator as was used for the water-box measurements (see Section 3.2.3). We measured the total absorbed dose from photons using thermo-luminescent dosimeters (TLDs) placed at each of 39 locations in organs and tissues throughout the phantom spanning in-, near-, and far-from-field regions (See Figure 3.3c). These dosimeters were composed of lithium

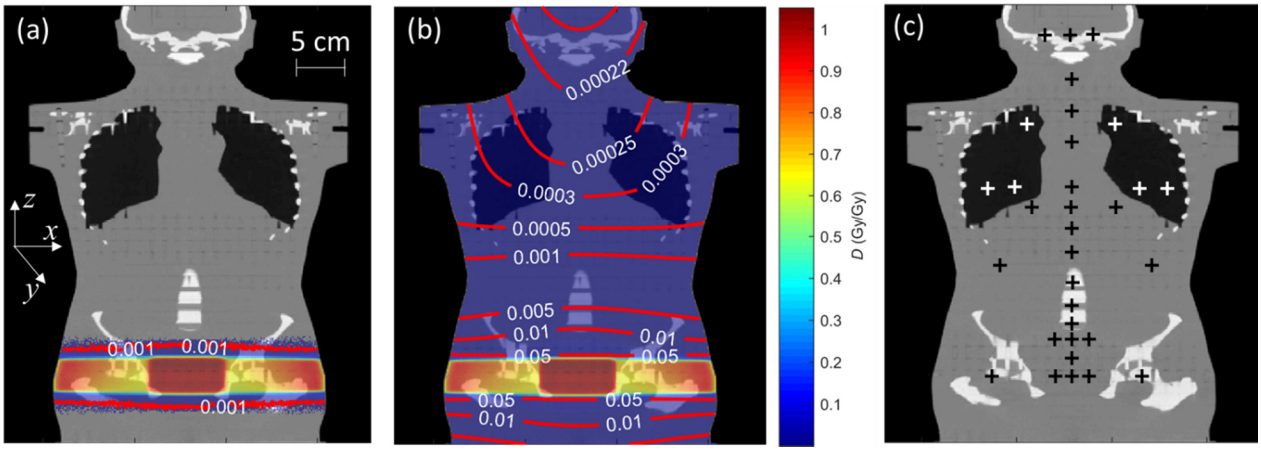

Figure 3.3. Representative examples of dose calculations for validation in an anthropomorphic phantom. Isocentric coronal slice of the anthropomorphic phantom with the color wash representing the relative dose calculated by CERR (a) and CERR-LSU (b) for the 6-MV, 4-field-box prostate treatment plan. Results for the 15-MV calculations were qualitatively similar. Doses were normalized using the dose at isocenter. Isodose lines provide the dose distribution in the far-from-field region in greater detail. The crosses in panel (c) indicate the approximate TLD-measurement locations in the anthropomorphic phantom.

fluoride TLD-100 rods and are suitable for measuring out-of-field photon dose[87]. We irradiated the TLDs in three groups based on the expected dose to the TLD location (*i.e.,* high, medium, and low dose, see Table 3.2) in order to ensure that the dose delivered to each TLD was within the calibrated range. Finally, we corrected the measurements for the changes in spectral photon fluence with location using the methods of Chofor *et al.*[85, 86]

Table 3.2. Characteristics of each field delivered to the anthropomorphic phantom: anterior-posterior (AP), posterior-anterior (PA), left lateral (LL), and right lateral (RL). Details include the number of monitor units delivered and the total planned absorbed dose to isocenter from all four beams (D_{Rx}).

TLD Measurement Group	Monitor Units Delivered				
	AP	PA	LL	RL	D_{Rx}(Gy)
High-dose	31.3	31.3	37.8	37.8	1
Medium-dose	626	626	755.1	755.1	20
Low-dose	6260	6260	7560	7560	200

We normalized the measured dose magnitudes using the planned dose at isocenter (D_{Rx}, see Table 3.2) to obtain the measured relative-absorbed-dose magnitudes. We extracted the relative

dose magnitudes calculated by CERR and CERR-LSU at locations corresponding to the TLD-measurement locations. Finally, we characterized the dosimetric accuracy of CERR and CERR-LSU compared to measurements in the anthropomorphic phantom using the methods described in Section 3.2.4.

3.2.6. CERR-LSU Computation Time

In order to characterize the additional time required to calculate dose using CERR-LSU compared to CERR, we recorded the system CPU-time at the beginning and end of dose calculations. We quantified the total computation time for each system as the difference between beginning and end times. We followed these methods for four selected field sizes incident on a 44x30x180 cm^3 water-box phantom. We chose this phantom size to approximate the size of a large adult human[88]. Field sizes included 2-, 5-, 10-, and 20-cm squares. We repeated these methods for isotropic dose grids of 1- and 2-cm^3 resolution to assess the impact of grid resolution on computation time. We also performed calculations to four regions of interest that varied in volume in order to assess the impact of grid size on the computation time. The smallest region of interest approximated the size of a torso and the largest included the entire phantom (see Table 3.3).

Table 3.3. Regions of interest for characterizing the computation time of CERR-LSU compared to CERR. Details include the *x*, *y*, and *z* dimensions (see Figure 3.3a for coordinate system) of the region and the number of calculation points, N, included in each region at each grid resolution.

			N	
x (cm)	*y* (cm)	*z* (cm)	1-cm^3 grid	2-cm^3 grid
44	30	60	8.5×10^4	1.1×10^4
”	”	100	14×10^4	1.9×10^4
”	”	151	21×10^4	2.8×10^4
”	”	180	25×10^4	3.3×10^4

3.3. Results

3.3.1. CERR-LSU Configuration

Table 3.4 lists the analytical-model parameters obtained by fitting the analytical model to measured dose profiles (see Table 3.1) following the methods of Schneider *et al.*[67] Figure 3.4 shows a selection of representative examples of measured and calculated absorbed dose profiles from the CERR-LSU configuration process. This figure reveals that, qualitatively, CERR-LSU calculations accurately approximated measurements in all regions of dose (*i.e.,* in-, near-, and far-from field) for a variety of irradiation conditions.

Table 3.5 lists the results of the quantitative assessment of the dosimetric accuracy of CERR-LSU configuration. These data show that CERR-LSU had equivalent or superior accuracy compared to CERR in all regions of dose with the largest improvements in the out-of-field region. The most pronounced improvements were measured by the median relative and absolute dose differences (*i.e.,* dD_{R} and dD_{A}, respectively), which decreased by factors of 2 and 50, respectively. These data also show that the average dose discrepancies for CERR-LSU were within ±1% in and near to the treatment field and ±1 mGy/Gy far from the field, indicating that there were no sizable systematic discrepancies.

Table 3.6 lists the values of the generalized-gamma-index agreement criteria at four selected passing rates found using the systematic-search methods of Wilson *et al*.[33] These data show that the appropriate ΔD_{R} and Δd magnitudes for CERR-LSU at a passing rate of 90% were comparable to those for contemporary commercial systems[42].

Table 3.4. Magnitudes of analytical-model parameters. Parameters found by training the model to measurements of 6- and 15-MV photon beams using doses measured for the purpose of model configuration, listed in Table 3.1.

Term in Eq. 3.1	Description	Symbol (units)	Magnitude
D_{P} (Primary)	Dose 0th order coefficient	A_{P} (mGy/Gy)	900
	Field-edge correction factor	$\bar{x}_{\mathrm{P},0}$ $(-)$	1.02
	Secondary collimator penumbral width	$\sigma_{\mathrm{P},0}$ (cm)	0.29
	Projection correction factor	α_{P} $(-)$	0.95
	Attenuation 0th order correction factor	$b_{\mu,\mathrm{P}}$ $(-)$	0.69
	Attenuation 1st order correction factor	$m_{\mu,\mathrm{P}}$ (MeV^{-1})	3.6×10^{-2}
D_{HS} (Head Scatter)	Dose 0th order coefficient	β_{HS} (mGy/Gy)	4000
	Dose 1st order coefficient	γ_{HS} (mGy/Gy/MeV)	723
	Source width parameter	$\alpha_{\mathrm{HS},0}$ (cm)	4.25
	Projection correction factor	α_{HS} $(-)$	0.64
	Attenuation 0th order correction factor	$b_{\mu,\mathrm{HS}}$ $(-)$	-0.13
	Attenuation 1st order correction factor	$m_{\mu,\mathrm{HS}}$ (MeV^{-1})	0.19
D_{PS} (Patient Scatter)	Dose 0th order coefficient	β_{PS} (mGy/Gy)	8586
	Dose 1st order coefficient	γ_{PS} (mGy/Gy/MeV)	-0.06
	Lateral width	$\alpha_{\mathrm{PS},0}$ (cm)	15.0
	Projection correction factor	α_{PS} $(-)$	1.04
	Attenuation 0th order correction factor	$b_{\mu,\mathrm{PS}}$ $(-)$	1.41
	Attenuation 1st order correction factor	$m_{\mu,\mathrm{PS}}$ (MeV^{-1})	-9.1×10^{-19}
D_{L} (Leakage)	Dose 0th order coefficient	β_{L} (mGy/Gy)	10202
	Dose 1st order coefficient	γ_{L} (mGy/Gy/MeV)	-0.03
	Lateral width correction factor	$\alpha_{\mathrm{L},0}$ (cm)	340
	Projection correction factor	α_{L} $(-)$	0.86
	Attenuation 0th order correction factor	$b_{\mu,\mathrm{L}}$ $(-)$	1.71
	Attenuation 1st order correction factor	$m_{\mu,\mathrm{L}}$ (MeV^{-1})	-9.2×10^{-3}
	Primary collimator 0th order coefficient	β_{PC} $(-)$	0.32
	Primary collimator 1st order coefficient	γ_{PC} (MeV^{-1})	2.2×10^{-2}
	Primary collimator location	$\bar{x}_{\mathrm{PC}}$ (cm)	22.5
	Primary collimator penumbral width	$\sigma_{\mathrm{PC},0}$ (cm)	0.05

3.3.1. Validation in a Water-Box Phantom

Figure 3.5 plots representative examples of absorbed dose calculated by CERR-LSU compared to measurements for the purpose of validation in a water-box phantom (see Table 3.1). This figure shows that, qualitatively, CERR-LSU accurately calculated the dose for field sizes, aspect ratios, and depths in water that differed from those for which it was specifically configured.

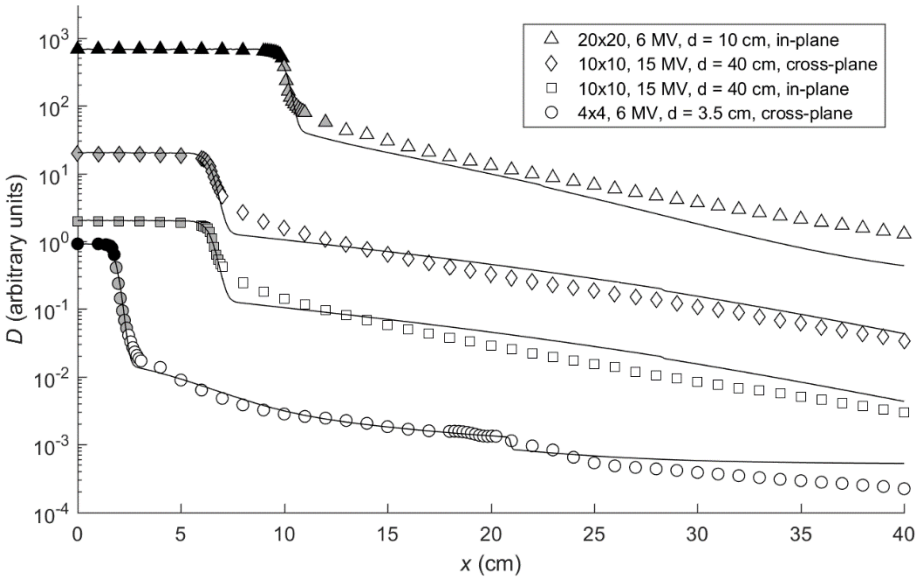

Figure 3.4. Representative examples of the results of CERR-LSU configuration. Relative dose (D) versus distance from the beam central axis (x). Points represent measured dose magnitudes and lines represent CERR-LSU calculations. Black-filled markers are located in the in-field region, gray-filled markers are in the near-field region, and open markers are in the far-from-field region. Note that profiles at a depth of 40 cm did not contain any points in the in-field region because the depth was such that the dose on the CAX was below 50% of D_{Rx}. Absorbed dose magnitudes for each profile are offset by factors of 10 for visual clarity.

Table 3.5. Dosimetric agreement as assessed by comparison to configuration data. Data include the average, root-mean-square (RMS), median, and maximum dose discrepancies for relative dose comparisons (dD_{R}) in the in- and near-field regions and absolute dose comparisons (dD_{A}) in the far-from-field region (see Section 3.2.2). Data are for calculations by CERR and CERR-LSU compared to measurements of 6- and 15-MV photon beams in a water-box phantom for the purpose of configuration (see Table 3.1).

	In- and Near-Field Regions dD_{R} (%)		Far-from-Field Region dD_{A} (mGy/Gy)	
	CERR	CERR-LSU	CERR	CERR-LSU
Average	-1.3	-0.81	-3.5	-0.32
RMS	5.0	5.0	7.5	3.7
Median	-0.84	-0.44	-1.1	-0.022
Maximum	37	36	58	35

Table 3.7 lists the results of the quantitative assessment of dosimetric agreement for validation in water. These data reveal that CERR-LSU achieved superior accuracy to that of CERR in all regions of dose. Furthermore, the mean, RMS, and median discrepancies for CERR-LSU in the out-of-field region were similar to those in Table 3.5. This suggests that the accuracy in the out-

Table 3.6. Generalized-gamma-index agreement criteria for an interval of selected passing rates. Agreement criteria include relative dose difference (ΔD_{R}), absolute dose difference (ΔD_{A}), and distance to agreement (Δd), and were determined based on comparisons to measurements of 6- and 15-MV photon beams in a water-box phantom (see Table 3.1).

Passing Rate (%)	ΔD_{R}(%)	ΔD_{A}(mGy/Gy)	Δd(mm)
100	8.2	23.8	3.5
95	6.3	6.8	1.5
90	4.5	3.8	1.25
67.5	4.1	1.2	1.0

of-field region was not sensitive to changes in treatment configuration and provides evidence of CERR-LSU's high level of adaptability to different treatment configurations. The generalized-gamma-index passing rate for CERR-LSU at criteria of 4.5% relative dose difference, 3.8 mGy/Gy absolute dose difference, or 1.25 mm distance to agreement was 90%. The generalized-gamma-index passing rate for CERR compared to the same measurements and at the same agreement criteria was substantially lower at only 64%. These results indicate that CERR-LSU passed the gamma-index analysis while CERR failed at the typical test requirement of a 90% passing rate[42].

3.3.1. Validation in Clinically Realistic Anatomy

Figure 3.6 plots a representative example of the measured and calculated cephalocaudal profiles from the validation of CERR and CERR-LSU in an anthropomorphic phantom. Dot-dashed lines show the 1-σ confidence interval in CERR-LSU calculations, *i.e.,* the interval containing 67.5% of measurements. This figure clearly demonstrates the improved dosimetric accuracy of CERR-LSU compared to CERR in the far-from-field region. Table 3.8 lists the absorbed-dose magnitudes measured by TLD, calculated by CERR-LSU, and calculated by CERR at each of the 39 TLD locations for 6- and 15-MV irradiations. These data indicate that the largest discrepancies were in and near boney structures (*e.g.,* femoral heads and spinal cord) and near to the field edge (*e.g.,* rectum and bladder).

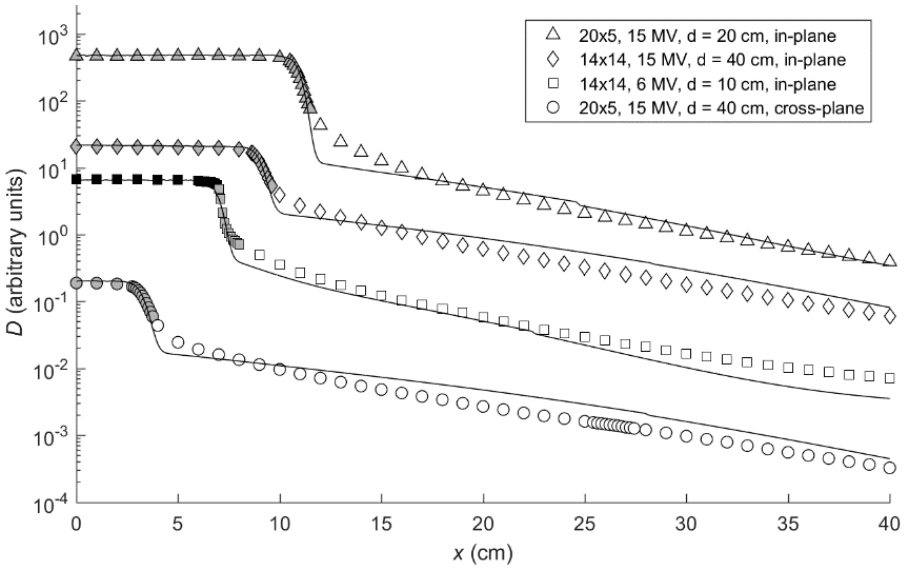

Figure 3.5. Representative examples of dosimetric validation of CERR-LSU profiles in a water-box phantom. Relative absorbed dose (D) versus distance from the beam central axis (x). Points represent measured absorbed dose and lines represent CERR-LSU calculations. Black-filled markers are located in the in-field region, gray-filled markers are in the near-field region, and open markers are in the far-from-field region. Note that profiles for small field areas and at deep depths did not contain any points in the in-field region (*i.e.,* the relative dose on the CAX was below 5% of D_{Rx}). Absorbed-dose magnitudes for different profiles are offset by factors of 10 for visual clarity.

Table 3.7. Dosimetric agreement as assessed by comparison to data for validation in a water-box phantom. Data include the average, root-mean-square (RMS), median, and maximum dose discrepancies for relative dose comparisons (dD_{R}) in the in- and near-field regions and absolute dose comparisons (dD_{A}) in the far-from-field region (see Section 3.2.2). Data are for calculations by CERR and CERR-LSU compared to measurements of 6- and 15-MV photon beams in a water-box phantom for the purpose of validation (see Table 3.1).

	In- and Near-Field Regions dD_{R} (%)		Far-from-Field Region dD_{A} (mGy/Gy)	
	CERR	CERR-LSU	CERR	CERR-LSU
Average	-0.79	-0.068	5.1	0.53
RMS	2.9	2.6	9.2	4.6
Median	-0.56	-0.14	-2	-0.053
Maximum	16	15	48	50

Table 3.9 lists the results of the quantitative assessment of dosimetric agreement for validation in an anthropomorphic phantom at 6- and 15-MV photon-beam energies. These data show that CERR-LSU achieved markedly better accuracy than CERR in the anthropomorphic phantom. The improvement in dosimetric accuracy was especially pronounced in the far-from-field region

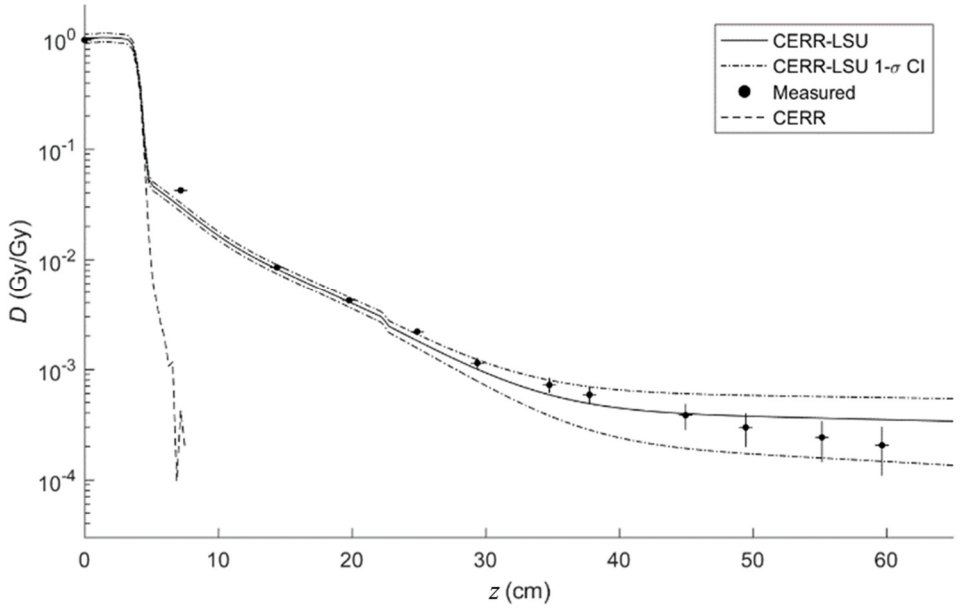

Figure 3.6. Representative example of the results of validation in an anthropomorphic phantom. Relative absorbed dose (D) versus cephalocaudal distance from isocenter (z) for 6-MV measurements and calculations (see Figure 3.3a for coordinate system). Findings for 15 MV were comparable. Measurement error bars represent 1-σ uncertainties. We estimated the dosimetric uncertainty (i.e., vertical error) following the methods of Kry *et al.*[87] We estimated horizontal error bars as the uncertainty in TLD location resulting from positioning uncertainties following the methods of Topolnjak *et al.*[89]

Table 3.8. Values of the absorbed dose measured by TLD, calculated by CERR-LSU, and calculated by CERR for the validation in an anthropomorphic phantom. The listed organ locations for each TLD are approximate (see Figure 3.3c).

		Relative Dose (mGy/Gy)					
		6 MV			15 MV		
TLD Location	Phantom Slice	Measured	CERR-LSU	CERR	Measured	CERR-LSU	CERR
PTV (Isocenter)	34	960	990	990	980	990	990
PTV (Patient L)	34	970	980	980	980	980	980
PTV (Patient R)	34	970	970	970	980	980	980
Femoral Head (R)	34	530	510	460	530	510	470
Femoral Head (L)	34	510	440	430	520	450	430
Rectum	33	720	950	950	700	960	960
Rectum	32	140	52	16	130	52	16
Bladder	32	83	50	19	96	50	18
Bladder	32	74	48	20	70	48	19

(table cont'd.)

		Relative Dose (mGy/Gy)					
		6 MV			15 MV		
TLD Location	Phantom Slice	Measured	CERR-LSU	CERR	Measured	CERR-LSU	CERR
Bladder	32	120	53	16	130	53	17
Bladder	32	45	53	17	38	53	17
Bladder	31	34	26	0.28	25	26	0.18
Spinal cord	29	3.3	11	0	9.1	11	0
Kidney (L)	26	3.3	3.7	0	3.0	3.7	0
Kidney (R)	26	3.2	3.7	0	3.0	3.7	0
Stomach	24	2.2	1.8	0	2.3	1.8	0
Liver	22	1.1	0.99	0	1.2	1.0	0
Chest (skin)	19	0.90	0.63	0	0.98	0.63	0
Chest (skin)	19	0.73	0.63	0	0.73	0.63	0
Chest (skin)	19	0.86	0.64	0	1.0	0.64	0
Lung	18	0.30	0.39	0	0.45	0.39	0
Lung	18	0.30	0.39	0	0.44	0.39	0
Lung	18	0.53	0.49	0	0.69	0.50	0
Lung	18	0.53	0.50	0	0.68	0.50	0
Lung	13	0.50	0.51	0	0.63	0.52	0
Lung	13	0.50	0.52	0	0.62	0.52	0
Heart	14	0.30	0.37	0	0.45	0.37	0
Thyroid	10	0.20	0.35	0	0.34	0.35	0
Brain stem	5	0.18	0.33	0	0.36	0.33	0
Lens of eye (R)	5	0.26	0.33	0	0.26	0.33	0
Lens of eye (L)	5	0.25	0.28	0	0.26	0.28	0
10 cm Superior to Isocenter	31	42	30	0.38	35	30	0.23
15 cm Superior to Isocenter	28	8.5	8.2	0	6.9	8.2	0
20 cm Superior to Isocenter	26	4.2	4.1	0	3.8	4.0	0
35 cm Superior to Isocenter	20	0.72	0.58	0	0.86	0.59	0
40 cm Superior to Isocenter	19	0.58	0.49	0	0.74	0.49	0
45 cm Superior to Isocenter	16	0.38	0.39	0	0.56	0.40	0
55 cm Superior to Isocenter	12	0.24	0.36	0	0.37	0.36	0
60 cm Superior to Isocenter	10	0.20	0.35	0	0.34	0.35	0

where CERR-LSU achieved a median dD_{A} nearly 26 times smaller than that of CERR.

Furthermore, CERR-LSU achieved agreement in an anthropomorphic phantom similar to that in

a water-box phantom (see Table 3.7). This indicates that the accuracy was not sensitive to the presence of clinically realistic anatomy (*i.e.,* surface irregularities and tissue heterogeneities).

Table 3.9. Dosimetric agreement as assessed by comparison to absorbed dose measured in an anthropomorphic phantom. Data include the average, root-mean-square (RMS), median, and maximum dose discrepancies for relative dose comparisons (dD_{R}) in the in- and near-field regions and absolute dose comparisons (dD_{A}) in the far-from-field region (see Section 3.2.2). Data are for calculations by CERR and CERR-LSU compared to measurements of 6- and 15-MV photon beams in an anthropomorphic phantom (see Section 3.2.5).

	In- and Near-Field Regions dD_{R} (%)		Far-from-Field Region dD_{A} (mGy/Gy)	
	CERR	CERR-LSU	CERR	CERR-LSU
Average	-2.3	-0.3	-4.4	0.2
RMS	10	9.0	10	3.2
Median	-5.9	-2.4	-0.70	-0.027
Maximum	26	26	42	15

The generalized-gamma-index passing rate for agreement criteria of 4.5% relative dose difference, 3.8 mGy/Gy absolute dose difference, or 1.25 mm distance to agreement was 81%. The generalized-gamma-index passing rate for CERR comparisons to TLD measurements in the same anthropomorphic phantom and at the same agreement criteria was considerably lower at only 8%. These results provide further evidence of the improved dosimetric accuracy of CERR-LSU compared to CERR. Figure 3.7 plots the generalized-gamma-index results for both CERR and CERR-LSU analyses versus the measurement point's cephalic distance from isocenter. These plots clearly show that CERR and CERR-LSU had comparable agreement in the in- and near-field regions while CERR-LSU performed better than CERR in the far-from-field region. More specifically, Figure 3.7a reveals that CERR-LSU performed better far from the treatment field than in and near to the treatment field. Figure 3.7b, on the other hand, shows that CERR performed best in the treatment field and failed at all far-from-field locations. This indicates that CERR-LSU was limited by its dosimetric accuracy in the in- and near-field regions (*i.e.,* by

doses supplied by CERR) while CERR was limited by its dosimetric accuracy in the far-from-field region.

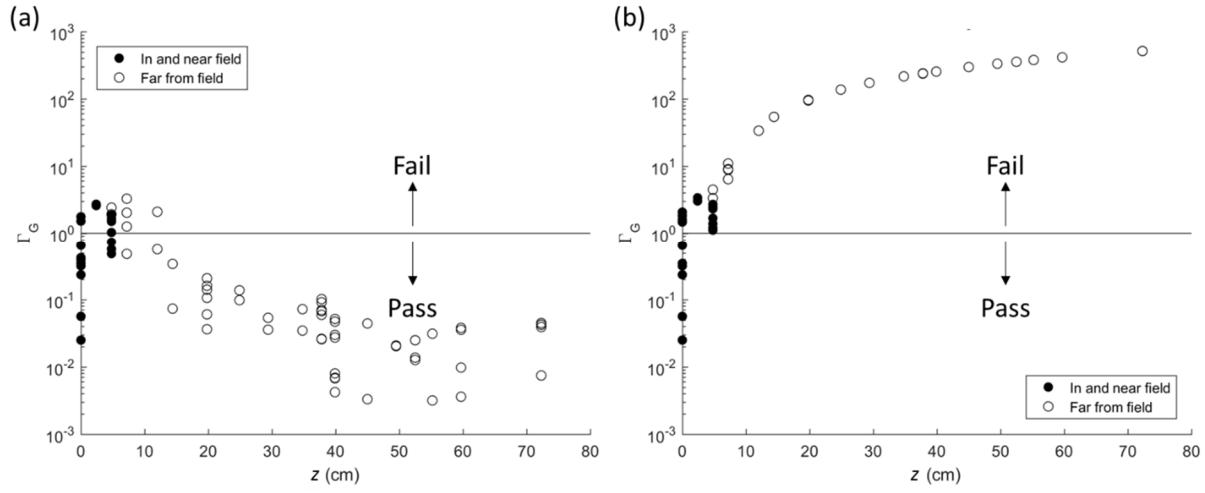

Figure 3.7. Results of the generalized-gamma-index analysis in an anthropomorphic phantom. Generalized-gamma-index magnitudes, Γ_G, versus the measurement cephalic distance from isocenter, z, for (a) CERR-LSU and (b) CERR compared to 6- and 15-MV TLD measurements in an anthropomorphic phantom (see Figure 3.3a for coordinate system). The horizontal solid line separates passing and failing generalized-gamma-index magnitudes.**CERR-LSU Computation Time**

Figure 3.8a shows a representative example of the results of the timing characterization for CERR and CERR-LSU. This figure reveals that the computation time for both systems increased with increasing therapeutic field size and number of calculation points. Figure 3.8b plots the CERR-LSU computation time relative to that for CERR and shows that CERR-LSU required less than 1.3 times the computation time of CERR for all field sizes and regions of interest studied. On average, CERR-LSU required 7% longer than CERR to additionally calculate the absorbed dose from stray radiation exposures. Figure 3.8b also shows that the additional calculation time required by CERR-LSU decreased with increasing therapeutic field size and number of calculation points.

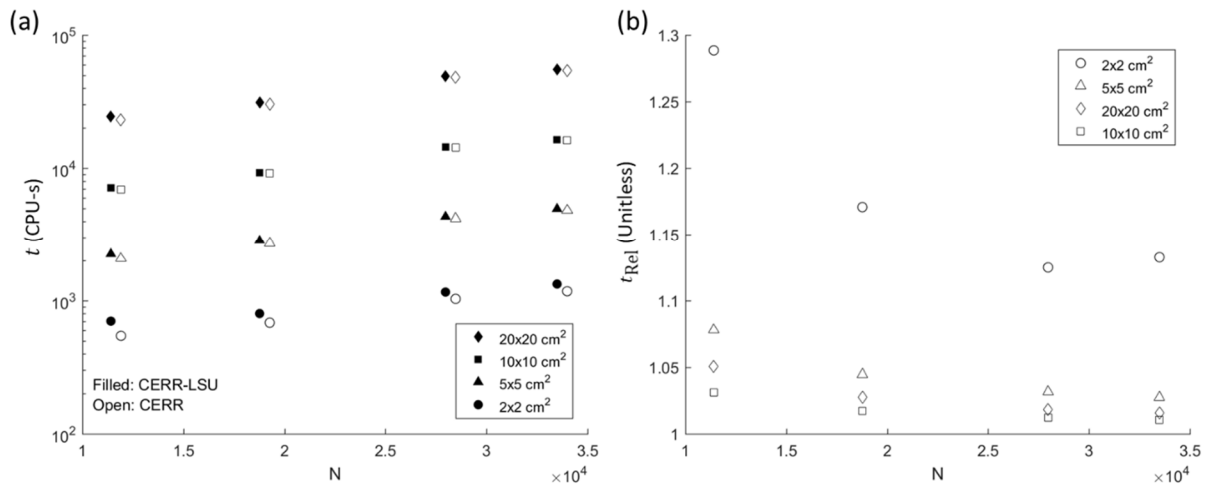

Figure 3.8. Representative example of the characterization of computation time. (a) Computation time, t, in CPU-s versus the number of calculation points, N, for four square field sizes at a 2-cm^3 grid resolution. Filled markers represent CERR-LSU while open markers are for CERR. CERR calculation times are offset by 500 calculation points for visual clarity. (b) Relative timing, t_{Rel}, versus the number of calculation points, N, at a 2-cm^3 grid resolution where t_{Rel} is defined to be the ratio of computation times for CERR-LSU to CERR or, $\frac{t_{\mathrm{CERR\text{-}LSU}}}{t_{\mathrm{CERR}}}$. Results for a 1-cm^3 calculation-grid resolution were qualitatively similar.

3.4. Discussion

In this study, we integrated a physics-based analytical model for the total absorbed dose, including that from stray photons, into a TPS. We configured and validated the system, CERR-LSU, for 6- and 15-MV photon beams using measurements in water-box and anthropomorphic phantoms. The major finding of this work is that it does appear to be feasible to accurately and quickly calculate the total absorbed dose from both therapeutic and stray photons in individual patients as part of a routine treatment-planning process. The specific results of this study revealed a sizable improvement in accuracy in the out-of-field region for calculations by CERR-LSU compared to CERR. For example, we reduced the uncertainty in out-of-field dose to less than 0.5 mGy/Gy at a distance of 30 cm from the beam CAX versus 20 mGy/Gy for CERR at the same location. We expect this improvement in dosimetric accuracy to pertain to commercial TPS's as well. Figure 3.9 shows a representative example of the measured total absorbed dose

along with confidence intervals corresponding to the 1-σ uncertainty in dose calculations by commercial TPS's and CERR-LSU. This figure clearly demonstrates the improvement of dosimetric accuracy in the far-from-field region by CERR-LSU compared to the commercial systems considered in this study. Furthermore, this improved dosimetric accuracy was possible with an average increase in computation time of only 7%.

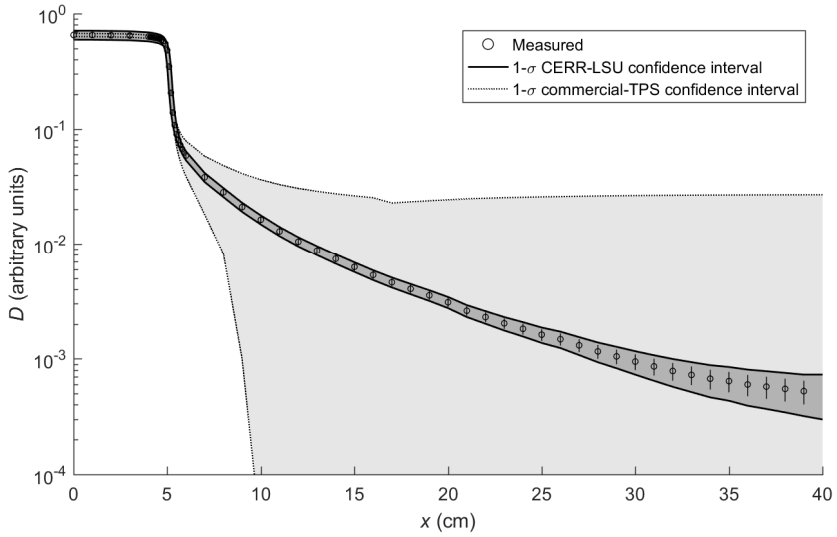

Figure 3.9. 1-σ confidence intervals for commercial-TPS and CERR-LSU dose calculations. Relative absorbed dose (*D*) versus distance from the beam central axis (*x*). Measured dose corresponds to a 10x10 cm^2, 6-MV photon beam at a depth of 10 cm in water.

The implication of these findings is that treatment planning systems should include these or similar algorithms to accurately predict stray radiation exposures. Knowledge of these exposures is a requisite step in risk projection and the optimization of patient health outcomes (as in Wilson *et al.*[36], see Chapter 5). Similarly, the creation of personalized survivorship care plans will require complete exposure data. Additionally, the routine availability of out-of-field doses could simplify the treatment of patients with implanted electronic devices, such as pacemakers and defibrillators. For these patients, it is necessary to estimate the dose to the device, even when it is far from the treatment field, in order to avoid potential device malfunctions[90]. Similarly, these

capabilities could find application to treatment planning for patients requiring retreatment for a recurrence or second primary cancer. In these cases, ensuring that the cumulative dose to healthy tissues remains at safe levels necessitates detailed reconstructions of the dose delivered by the initial treatment, even at far distances from the initial target volume. Such reconstructions could be readily calculated using an extended system, like the one developed in this work. Finally, such an extended system could find use in large-scale epidemiology studies on radiation-related health effects. Currently, the majority of such studies combine two or more dose-reconstruction methods in order to meet requirements of speed and accuracy in therapeutic and stray-dose calculations[75]. A tool like the one developed in this work could greatly simplify and streamline the dose-reconstruction process, including recording the exposures into the electronic medical record, and facilitating the continued development and refinement of risk models.

Our findings are consistent with others in the literature. In the most closely related study, Eley *et al.*[83] implemented an analytical model for leakage-neutron equivalent dose into a proton radiotherapy treatment planning system. Their extended system increased the computation time by 60%, which is on the same order of magnitude of our maximum estimate of the additional time required for therapeutic and stray photon dose calculations of 30%. Wang and Ding assessed the accuracy of out-of-field dose calculations of a model-based algorithm in a commercial TPS. Their out-of-field discrepancy was on the same order of magnitude as ours (*i.e.,* theirs ranged from 3 to 5 mGy/Gy versus our 1 mGy/Gy). Schneider *et al.*[67] previously reported on the analytical model implemented in this work. In the previous study, Schneider *et al.* trained the model to measurements in a water-box phantom from another Elekta medical linear accelerator for three nominal photon beam energies (*i.e.,* 6, 18, and 25 MV). Their average unsigned dosimetric discrepancy with the measurements used to train the model was similar to

ours (9.9% versus CERR-LSU's 3.5%). In another study, Taddei *et al.* developed an empirical analytical model for the stray dose from photon therapy[79]. They reported an RMS deviation from out-of-field measurements in an anthropomorphic phantom of 0.91 cGy/Gy, which is on the same order of magnitude as that of CERR-LSU under comparable conditions, namely, 0.32 cGy/Gy. Hauri *et al.* developed an analytical model for the stray dose from 6-MV photon therapy and validated their model with TLD measurements of a 4-field-box prostate treatment in an anthropomorphic phantom[91]. We found a similar mean dose discrepancy between measurements and calculations in the far-from-field region, *i.e.,* 8.5% in this work and 9% in Hauri *et. al*.

This study has several notable strengths. First, our approach utilized a non-proprietary, physics-based analytical algorithm to quickly and accurately calculate the of out-of-field doses[67]. Physics-based algorithms are more readily adaptable to other treatment units and modalities than, for example, purely empirical models. This study also included high-quality data measured at a national standards laboratory. These measurements spanned a wide range of irradiation conditions and enabled an extensive validation of CERR-LSU in water-box and anthropomorphic phantoms.

This study has several limitations. First, we only configured and validated CERR-LSU for conventional photon therapy. This was not a serious limitation because extension to more complex contemporary treatment deliveries, such as intensity-modulated radiotherapy (IMRT), is possible. Indeed, this challenging task is underway in our laboratory and elsewhere. Another limitation is that we only included stray dose from photons. Photon-beam energies above approximately 8 MV also produce photo-neutrons, mainly in the high-Z components of the treatment head. Our approach neglected these stray neutrons for the 15-MV irradiations. The scope of this study was to incorporate the dose from stray photons. Numerous recent publications

reported measurements and simulations of the photo-neutrons created during high-energy photon therapy[92-97] and models can be added to the presented framework when they are sufficiently mature. Furthermore, there is ongoing work in our laboratory to develop another component of this analytical model, specifically for dose from photo-neutrons. Preliminary results are encouraging. We anticipate that implementation of a physics-based analytical neutron-dose model could follow the same methods as those described above without having a large effect on the computation time based on the findings of Eley *et al.*[83] Another limitation is that the analytical model used to predict stray dose, in its current form, neglects tissue heterogeneities and surface irregularities. In spite of the current limitations of the extended TPS, we were still able to achieve a vastly improved level of dosimetric agreement in the anthropomorphic phantom (see Figure 3.6 and Figure 3.7).

3.5. Conclusions

The extended TPS developed in this study enables the quick and accurate calculation of therapeutic and stray radiation exposures in individual patients. Our results provide promising evidence that it may be feasible to routinely calculate whole-body doses, including therapeutic- and stray-radiation exposures, in individual patients as part of the routine treatment-planning process. This additional out-of-field dosimetric information could enable the personalized consideration of radiotherapy late effects in both the treatment- and survivorship-care-planning phases of the radiotherapy workflow. This in turn could lead to improved long-term health outcomes for the growing population of cancer survivors, many of whom have received radiation therapy.

Chapter 4. Justification and Optimization of Planned Exposures: A New Framework to Aggregate Arbitrary Detriments and Benefits

4.1. Introduction

The general principle of radiation protection comprises three pillars: justification, optimization, and limitation[98, 99]. Justification refers to a planned radiation exposure's ability to "produce sufficient benefit to the exposed individuals or to society to offset the radiation detriment it causes."[100] The pillar of optimization suggests that the radiation doses and number of exposed people should be kept as low as reasonably achievable[100]. The final pillar, limitation, simply states that the combination of all exposures should be subject to dose limits[100]. The pillar of limitation is established by regulation and compliance is accomplished by administrative controls (*e.g.*, restricting access to radiation areas) and safety systems (*e.g.*, safety interlocks on radiation generators). Limitation is the most straightforward of the three pillars and compliance to limits requires little subjective judgement. In contrast, justifying and optimizing planned radiation exposures is generally more complex[101-104] because of myriad radiation effects, including benefits and detriments[102, 105, 106]. Consequently, justification and optimization commonly require approximations, simplifications, assumptions, and subjective judgement.

The International Commission on Radiological Protection (ICRP), a leading advisory body in the theory and application of radiation-protection principles, first proposed the application of cost-benefit analysis for planned radiation exposures in 1973[107]. They noted, however, the difficulties in applying such analyses to public and medical exposures. In fact, the ICRP explicitly excluded the protection of patients from their consideration of medical exposures until the late 1960s, based on an implicit assumption that the benefits to the patient outweighed any incurred risks[108]. The current guiding principle behind recommendations of the ICRP, first proposed in 1990, is the principle of "as low as reasonably achievable" or, ALARA[109]. The definition of reasonable in

this context, however, is largely a matter of subjective judgement based on concepts, common sense, wisdom, and field experience, rather than an objective judgement based on rigorous analysis[110].

Algorithmic methods of risk-benefit analysis are well established for planned medical exposures. A seminal framework for this was proposed by Holthusen[111] in 1936 using the probability of uncomplicated tumor control (P_+). P_+ weighs the benefit against the short-term risk associated with radiotherapy for cancer patients. In the eight decades that have followed, other researchers have extended and modified P_+ for a variety of radiotherapy applications[23, 25, 32]. Yet, P_+ has several important limitations, including that it neglects the risk of non-fatal detriments, which may seriously impact the patient's quality of life, as well as the risk of late-occurring detriments. Other groups have suggested entirely different algorithmic methods of performing radiotherapy risk-benefit analyses, most of which also only consider the patient's short-term health effects[22, 24, 27, 28]. Only since 2015 have studies taken the late-occurring health effects into account[29-31, 112]. All of these methods, however, were developed to evaluate the special case of patients receiving radiotherapy exposures, not for those receiving other forms of medical radiation[113], nor for occupational workers or the public. Recognizing this limitation, in 2014 the International Atomic Energy Agency (IAEA) released a call for action to "strengthen the radiation protection of patients and health workers overall," in which their first recommended actions were to enhance the implementation of justification and optimization in planned radiotherapy exposures[114]. Our literature search revealed the lack of an algorithmic method to justify and/or optimize planned radiation exposures that is comprehensive and generally applicable.

The purpose of this study was to develop a new, comprehensive conceptual framework and the corresponding quantitative methods to aggregate the benefits and detriments of a planned

radiation exposure to individuals, groups, and populations. Specifically, we developed a comprehensive figure of merit (FOM) that takes into account arbitrary host- and exposure-related factors, endpoints, and time points. We then applied this FOM to three illustrative examples of planned exposures: emergency response, diagnostic imaging, and cancer radiation therapy, to evaluate its utility in diverse settings.

4.2. Methods

4.2.1. Comprehensive Figure of Merit

Our proposed FOM builds on concepts in the P_+ formalism, with the introduction of three important new capabilities. First, we generalized it for application to individuals, groups, and populations. Second, we consider arbitrary numbers and types of benefits and/or detriments of planned exposures. Finally, we added the approach of limitation by introducing a penalty factor in the FOM for exposures in excess of specified exposure limits (*e.g.*, regulatory limits).

The FOM for an exposed individual of attained age, a, following the planned exposure at age e was calculated by,

$$FOM(a,e) = PF\left[F_{\mathrm{B}}(a,e) \times \left(1 - F_{\mathrm{D}}(a,e)\right)\right], \qquad 4.1$$

where PF is a penalty factor for exceeding applicable exposure limits[†], and $F_{\mathrm{B}}(a,e)$ and $F_{\mathrm{D}}(a,e)$ are the figures of benefit and detriment, respectively.

Although seemingly antithetical, we modeled $F_{\mathrm{B}}(a,e)$ and $F_{\mathrm{D}}(a,e)$ using identical principles. Namely, they were calculated using

[†] Exposure limits are a mechanism to constrain algorithmic optimization from converging on a solution that concentrates risk, *e.g.,* in one person in a group. This allows explicit consideration of the ethical principal of justice in the optimization.

$$F_{\mathrm{B}}(a,e) = \sum_{k=1}^{N_k} P_{\mathrm{B},k}(H,a,e) \times S_{\mathrm{B},k} \times T_{\mathrm{B},k}(a,e) \times O_{\mathrm{B},k} \quad 4.2$$

and

$$F_{\mathrm{D}}(a,e) = \sum_{m=1}^{N_m} P_{\mathrm{D},m}(H,a,e) \times S_{\mathrm{D},m} \times T_{\mathrm{D},m}(a,e) \times O_{\mathrm{D},m} \ , \quad 4.3$$

where Table 4.1 describes each term and its allowed domain. Figure 4.1a plots a selection of representative examples of the relationship between the probability of an effect (P) and the dose equivalent (H). Figure 4.1b shows representative examples of the relationship between P and time since exposure ($t = a - e$), for early- and late-occurring detrimental effects.

The penalty factor, PF, in Eq. 4.1 was calculated by,

$$PF = \prod_{p=1}^{N_{\mathrm{L}}} \left(\frac{H_{\mathrm{L},p}}{H_p} \right)^{n_p} \quad 4.4$$

where N_{L} is the number of exposure limits applicable to the exposed individual, $H_{\mathrm{L},p}$ is the value of the p^{th} exposure limit, and H_p is the corresponding planned exposure, specified in the same units. It should be noted that the number of exposure limits applied and their magnitudes are selected according to traditional categories, (*e.g.,* fetus, minor, adult, occupational worker, patient, maximally exposed occupational worker, average member of the public, *etc.*). The exponent n_p governs the rate of change in magnitude of the penalty factor as a function of dose equivalent, H_p, or

Table 4.1. Terms involved in calculating the figures of benefit and detriment using Eqs. 4.2 and 4.3. Details include the symbol, description, and allowed domain for each term. All parameters are unitless.

Term		Description	Allowed Domain
Benefit	Detriment		
N_k	N_m	Number of possible benefits (k) or detriments (m)	$0 \leq N \leq \infty$
$P_{\mathrm{B},k}(H,a,e)$	$P_{\mathrm{D},m}(H,a,e)$	Probability of a radiogenic effect as a function of the dose equivalent, H, attained age, a, and age at exposure, e (see Figure 4.1)	$0 \leq P(H,a,e) \leq 1$
$S_{\mathrm{B},k}$	$S_{\mathrm{D},m}$	Maximum relative magnitude of effect	$0 \leq S \leq 1$
$T_{\mathrm{B},k}(a,e)$	$T_{\mathrm{D},m}(a,e)$	Factor for other mitigating circumstances (*e.g.*, competing causes of mortality) as a function of attained age, a, and age at exposure, e	$0 \leq T(a,e) \leq 1$
$O_{\mathrm{B},k}$	$O_{\mathrm{D},m}$	Factor for other considerations that might be important to the decision-making process (*e.g.*, personal preference, economic gain/cost, access to follow up/intervention)	$0 \leq O \leq 1$

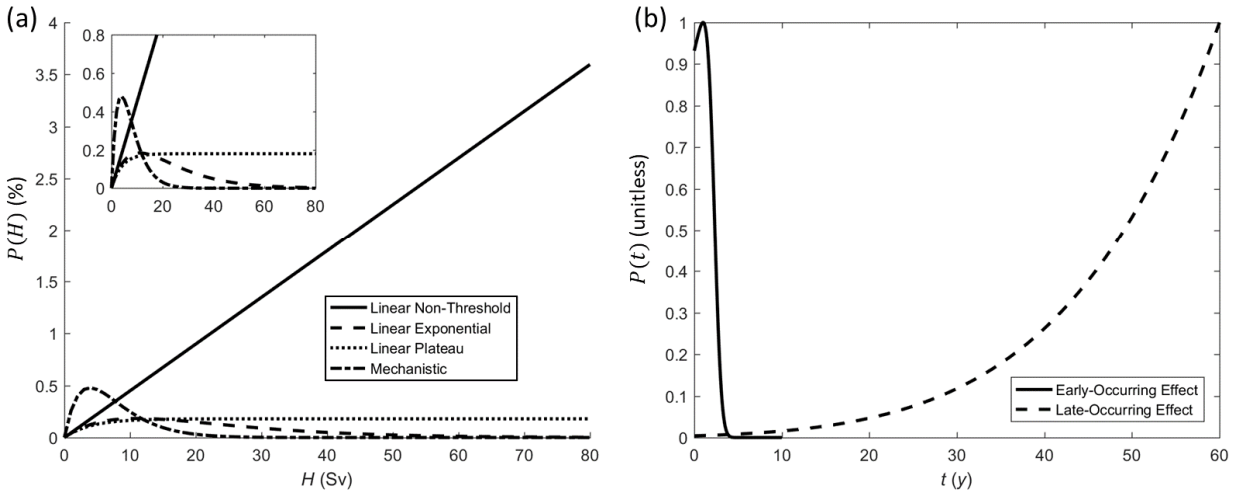

Figure 4.1. Representative examples of the differential probability of radiogenic effect, P, versus (a) dose equivalent, H, and (b) time since exposure, t. (a) Selection of dose-response functions for late effects including the linear-non-threshold, linear-exponential, and linear-plateau models; and the mechanistic model of Dasu *et al.*[115] (b) Representative examples of the relationship between P and time since exposure, $t = a - e$, for early- and late-occurring effects, respectively.

$$n_p = \begin{cases} 0 & \text{for } {H_{\mathrm{L},p}}/{H_p} \geq 1 \\ n_{\mathrm{L},p} & \text{for } {H_{\mathrm{L},p}}/{H_p} < 1, \end{cases} \tag{4.5}$$

where $n_{\mathrm{L},p}$ governs how rapidly the penalty increases with increasing exposure when the exposure limit, $H_{\mathrm{L},p}$, is exceeded. $n_{\mathrm{L},p}$ is a user-selected parameter of magnitude ≥ 1. Thus, penalties are only applied if an exposure exceeds a corresponding limit. Figure 4.2 plots some representative examples of penalty factor curves.

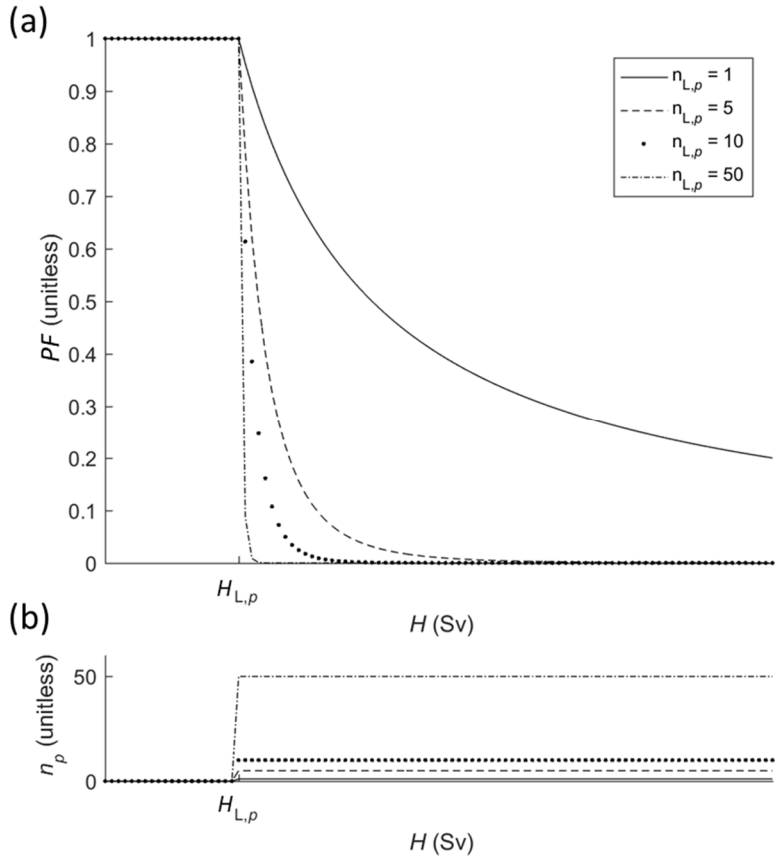

Figure 4.2. Representative examples of the Penalty Factor (*PF*). (a) *PF* versus planned dose equivalent (*H*) for a single exposure limit ($H_{\mathrm{L},p}$) at a selection of possible exponent magnitudes ($n_{\mathrm{L},p}$). (b) Plot of n_p from Eq. 4.5 versus *H* for the same exposure limit ($H_{\mathrm{L},p}$) and exponent magnitudes ($n_{\mathrm{L},p}$) as in panel (a).

The cumulative figure of merit, $\widetilde{FOM}$, from the age at exposure, e, to attained age, a, was calculated by,

$$\widetilde{FOM} = \int_e^a FOM(a,e)\mathrm{d}a \approx \sum_i FOM(a_i,e)\,\Delta a_i, \tag{4.6}$$

where Δa_i is the time differential of $FOM(a_i, e)$. In this work, we calculated cumulative lifetime figures of merit on the assumption that the maximum attained age, a, is 100 years.[‡] It should also be noted that $\widetilde{FOM}$ can be calculated directly using

$$\widetilde{FOM} = PF\left[\widetilde{F_{\mathrm{B}}} \times \left(1 - \widetilde{F_{\mathrm{D}}}\right)\right], \tag{4.7}$$

where $\widetilde{F_{\mathrm{B}}}$ and $\widetilde{F_{\mathrm{D}}}$ are the cumulative lifetime projections of the figures of benefit and detriment, respectively, calculated by,

$$\widetilde{F_{\mathrm{B}}} = \sum_{k=1}^{N_k} \widetilde{P_{\mathrm{B},k}}(H) \times S_{\mathrm{B},k} \times O_{\mathrm{B},k} \tag{4.8}$$

and,

$$\widetilde{F_{\mathrm{D}}} = \sum_{m=1}^{N_m} \widetilde{P_{\mathrm{D},m}}(H) \times S_{\mathrm{D},m} \times O_{\mathrm{D},m} \tag{4.9}$$

where $\widetilde{P_{\mathrm{B},k}}(H)$ and $\widetilde{P_{\mathrm{D},m}}(H)$ are the cumulative lifetime projections of the probabilities of benefit and detriment, respectively. These could be calculated, for example, using models like that of ICRP Report 60[116]. Note that in accumulated figures of benefit and detriment, the temporal factors $T_{\mathrm{B},k}$ and $T_{\mathrm{D},m}$ do not explicitly appear in Eqs. 4.8 and 4.9 as they are already implicitly included in the values of $\widetilde{P_{\mathrm{B},k}}(H)$ and $\widetilde{P_{\mathrm{D},m}}(H)$.

[‡] While we chose to calculate cumulative lifetime figures of merit, one could also calculate for arbitrary values of attained age $a \geq e$ (the age at exposure).

The preceding methods may also be applied to groups or populations. For example, say N_{B} individuals experience benefit and N_{D} individuals incur detriment. Then, for this application we have a figure of merit for a population of N individuals calculated by,

$$FOM_N(a,e) = \sum_{i=1}^{N_{\mathrm{B}}} F_{\mathrm{B},i}(a,e) \times \sum_{j=1}^{N_{\mathrm{D}}} \left(1 - F_{\mathrm{D},j}(a,e)\right) \tag{4.10}$$

where $F_{\mathrm{B},i}(t)$ and $F_{\mathrm{D},j}(t)$ are the figures of benefit and detriment to the i^{th} and j^{th} individuals, respectively. $F_{\mathrm{B},i}(t)$ and $F_{\mathrm{D},j}(t)$ are defined as in Eqs. 4.2 and 4.3. Note that this approach allows full and explicit accounting of the benefit and detriment to each individual in the group or population, whether they incur only risk, only benefit, or both, as the scenario may require.

Thus far, the formalism was evaluated for each individual, separately considering all of the various benefits, detriments, and exposure penalties unique to each individual exposed independently (Eq. 4.1) or as a member of a group or population (Eq. 4.10). In some cases, it is convenient or necessary to forego calculations for each individual and to directly estimate population-averaged results. The direct population-averaged FOM, denoted by $\overline{FOM}$, can be calculated using

$$\overline{FOM(a,e)} = \overline{PF}\left[N_{\mathrm{B}}\overline{F_{\mathrm{B}}(a,e)} \times N_{\mathrm{D}}\left(1 - \overline{F_{\mathrm{D}}(a,e)}\right)\right], \tag{4.11}$$

$$\overline{F_{\mathrm{B}}(a,e)} = \sum_{k=1}^{N_k} \overline{P_{\mathrm{B},k}(H,a,e)} \times \overline{S_{\mathrm{B},k}} \times \overline{T_{\mathrm{B},k}(a,e)} \times \overline{O_{\mathrm{B},k}}\,, \tag{4.12}$$

$$\widetilde{\overline{F_{\mathrm{B}}}} = \sum_{k=1}^{N_k} \widetilde{\overline{P_{\mathrm{B},k}}}(H) \times \overline{S_{\mathrm{B},k}} \times \overline{O_{\mathrm{B},k}}\,, \tag{4.13}$$

$$\overline{F_{\mathrm{D}}(a,e)} = \sum_{m=1}^{N_m} \overline{P_{\mathrm{D},m}(H,a,e)} \times \overline{S_{\mathrm{D},m}} \times \overline{T_{\mathrm{D},m}(a,e)} \times \overline{O_{\mathrm{D},m}}\,, \tag{4.14}$$

$$\widetilde{\overline{F_{\mathrm{D}}}} = \sum_{m=1}^{N_m} \widetilde{\overline{P_{\mathrm{D},m}}}(H) \times \overline{S_{\mathrm{D},m}} \times \overline{O_{\mathrm{D},m}} \,, \tag{4.15}$$

$$\overline{PF} = \prod_{p=1}^{N_{\mathrm{L}}} \left(\frac{H_{\mathrm{L},p}}{\overline{H_p}}\right)^{n_p} \,, \tag{4.16}$$

and

$$\widetilde{\overline{FOM}} = \overline{PF}\left[N_{\mathrm{B}}\widetilde{\overline{F_{\mathrm{B}}}} \times N_{\mathrm{D}}\left(1 - \widetilde{\overline{F_{\mathrm{D}}}}\right)\right] = \int_e^a \overline{FOM(a,e)}\mathrm{d}a \approx \sum_i \overline{FOM(a_i,e)}\,\Delta a_i \,, \tag{4.17}$$

where all parameters are the population-averaged magnitudes for those previously defined for an individual (see Table 4.1).

4.2.2. Illustrative Example Calculations

To evaluate the utility of this FOM for justifying and optimizing planned radiation exposures, we explored its application to inform decision making in three example scenarios: emergency response, diagnostic radiology, and cancer radiotherapy.

4.2.2.1 Emergency Response

In this hypothetical example, we optimized shift assignments for radiation workers during an emergency-response operation. The workers' goal is to minimize the imminent release of a radioactive plume. A nearby town contains 78,000 inhabitants, each of whom would receive a uniform whole-body, hard gamma-ray exposure rate (1 Sv/h) as the plume passes overhead (assumed exposure duration of 1 hour). The operation comprises two separate tasks. Task A involves isolating a cracked pipe to minimize the release of radioactive gas. Task B involves repairing damaged shielding surrounding a second pipe. Tasks A and B are separate and distinct (see Table 4.2), and both are necessary to minimize the plume (*i.e.,* no task can be neglected over the course of the operation). Additionally, there are 10 available workers, where each worker is

available for one 8-hour shift. With the workers and time available, it is not possible to entirely prevent a release (*i.e.,* the work required ≫ capacity to complete it) and therefore, the inhabitants of the town will incur some exposure.

Table 4.2. Details of exposure rates to radiation workers and inhabitants in the illustrative example calculation for emergency response. Details include the population-averaged exposure rate, $\dot{\bar{H}}_{\text{worker}}$, to workers assigned to task A or B and the reduction in the projected exposure rate to the public, $\dot{\bar{H}}_{\text{public}}$, per person-hour (PH), T, of effort applied to each task.

Task	$\dot{\bar{H}}_{\text{worker}}$ (mSv/h)	$\frac{\dot{\bar{H}}_{\text{public}}}{T}$ (mSv/h/PH)
A	3.0	-10.2
B	0.7	-6.1

Planning these exposures requires two decisions. First, we must decide how many of the 10 available workers to assign to tasks A and B. Next, we must decide how long each worker will perform tasks A and B. To reach wise decisions, we must justify exposures to each individual. In addition, we must optimize exposures to all individuals, groups, and populations. We must also limit exposures to responders and inhabitants in order to comply with regulatory limits. Justification, optimization, and limitation must respect the ethical principles of justice (*e.g.,* no individual may be sacrificed for the greater good) and autonomy (*e.g.,* each worker must be informed of risks and be allowed to make autonomous decisions regarding his or her exposure).

We applied our comprehensive figure of merit to this case in order to objectively justify and optimize exposures associated with the decisions regarding worker assignments. Specifically, we used the cumulative lifetime projection of the population-averaged figure of merit ($\widetilde{\overline{FOM}}$, see Eq. 4.17) to guide an algorithmic optimization of the assignment of the number of workers to tasks A and B and the time duration of each worker's assignment(s). We applied the principle of limitation by way of the penalty factor ($\overline{PF}$, see Eq. 4.16) based on the recommendations of the

ICRP, *i.e.,* $H_{\mathrm{L},p}$ was 20 mSv/y averaged over 5 years and not to exceed 50 mSv in any one year for occupational exposures and 1 mSv/y for public exposures[100].

We calculated the population-averaged figure of merit in this example corresponding to cumulative lifetime projections of the benefits and detriments using Eqs. 4.13 and 4.15 (*i.e.,* the temporal factors, $\overline{T_{\mathrm{D}}(a,e)}$ and $\overline{T_{\mathrm{B}}(a,e)}$, in Eqs. 4.12 and 4.14 were implicitly included in the cumulative probabilities of benefit and detriment). We calculated the cumulative figure of benefit for the example in emergency response, $\widetilde{\overline{F_{\mathrm{B,ER}}}}$, using Eq. 4.13 in consideration of a single benefit, avoidance of the risk of harmful effect from exposure to the radioactive plume. The risk of harmful effect considered was the lifetime incidence of radiogenic cancer from uniform, external, whole-body gamma-ray exposure. Thus, we calculated the cumulative population-averaged probability of benefit as,

$$\widetilde{\overline{P_{\mathrm{B}}}}(H) = \dot{\bar{H}}_{\mathrm{avoided}} \times \overline{R/_H}\,, \tag{4.18}$$

where $\dot{\bar{H}}_{\mathrm{avoided}}$ was the avoided exposure rate to the inhabitants due to the emergency-response operation and $\overline{R/_H}$ was the population-averaged lifetime risk coefficient for fatal radiogenic cancer induction per dose equivalent, taken as 5%/Sv[100].[§] More specifically,

$$\dot{\bar{H}}_{\mathrm{avoided}} = \dot{\bar{H}}_{\mathrm{A}} \times \overline{\Delta t_e} + \dot{\bar{H}}_{\mathrm{B}} \times \overline{\Delta t_e} \tag{4.19}$$

where $\overline{\Delta t_e}$ was the projected duration of the exposure of inhabitants to the plume, assumed to be 1 hour, and $\dot{\bar{H}}_{\mathrm{A}}$ and $\dot{\bar{H}}_{\mathrm{B}}$ were calculated by,

[§] Other, more detailed models may be used to calculate the probability of beneficial and/or detrimental effects, such as those published in the Biological Effects of Ionizing Radiation (BEIR VII) report. For simplicity, we used the model from the International Commission on Radiological Protection (ICRP) report number 60.

$$\dot{\tilde{H}}_{\mathrm{A}} = \left(\frac{\dot{\tilde{H}}_{\mathrm{public}}}{T}\right)_{\mathrm{A}} \times \mathrm{T}_{\mathrm{A}} \,, \tag{4.20}$$

and,

$$\dot{\tilde{H}}_{\mathrm{B}} = \left(\frac{\dot{\tilde{H}}_{\mathrm{public}}}{T}\right)_{\mathrm{B}} \times \mathrm{T}_{\mathrm{B}} \,, \tag{4.21}$$

where $\left(\frac{\dot{\tilde{H}}_{\mathrm{public}}}{T}\right)_{\mathrm{A}}$ and $\left(\frac{\dot{\tilde{H}}_{\mathrm{public}}}{T}\right)_{\mathrm{B}}$ were the decrease in the population-averaged exposure rates to the public per person-hour of effort applied to complete tasks A and B, respectively (Table 4.2), and T_{A} and T_{B} were the total number of person-hours spent by exposed workers on tasks A and B, respectively. It is necessary to explicitly include exposure durations (*i.e.,* $\overline{\Delta t_e}$, T_{A}, and T_{B}) in the equations above in order to allow algorithmic optimization and justification of exposures.

We calculated the cumulative figure of detriment (Eq. 4.15) in consideration of two detriments: radiogenic cancer and acute radiation syndrome (ARS). We calculated the population-averaged probability of second-cancer induction for the j^{th} exposed worker as

$$\widetilde{\overline{P_{\mathrm{D},1,J}}}(H) = \left[\left(\dot{\tilde{H}}_{\mathrm{worker}}\right)_{\mathrm{A}} \times t_{\mathrm{A},j} + \left(\dot{\tilde{H}}_{\mathrm{worker}}\right)_{\mathrm{B}} \times \mathrm{t}_{\mathrm{B},j}\right] \times \overline{R/_H} \tag{4.22}$$

where $\left(\dot{\tilde{H}}_{\mathrm{worker}}\right)_{\mathrm{A}}$ and $\left(\dot{\tilde{H}}_{\mathrm{worker}}\right)_{\mathrm{B}}$ were the exposure rates to the workers while performing tasks A and B, respectively (see Table 4.2), $t_{\mathrm{A},j}$ and $t_{\mathrm{B},j}$ were the duration of time the j^{th} worker was assigned to tasks A and B, respectively, and $\overline{R/_H}$ was the same as in Eq. 4.18. We calculated the cumulative population-averaged probability of ARS for the j^{th} worker, or $\widetilde{\overline{P_{\mathrm{D},2,J}}}(H)$, using an empirical sigmoidal function developed in this work based on the findings of Donnelly *et al.*[117] (see Figure 4.3).

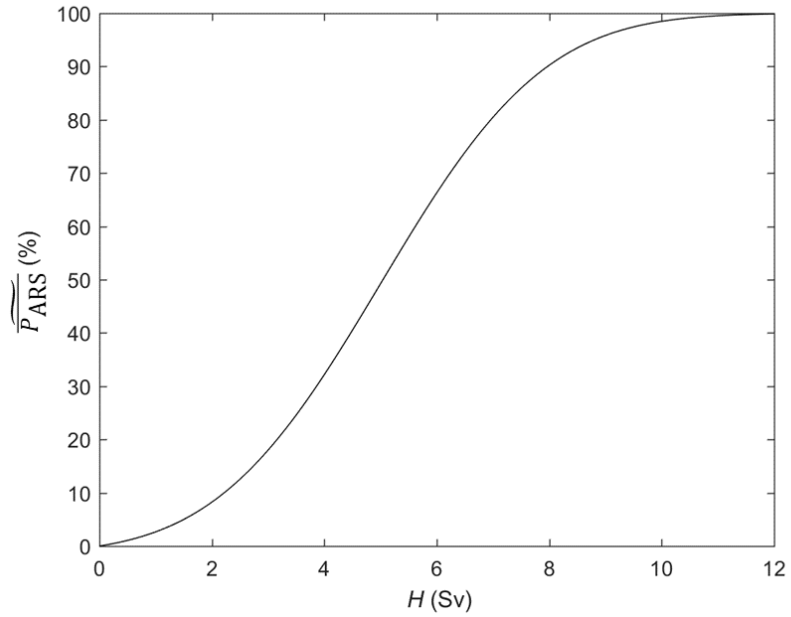

Figure 4.3. Empirical model for the probability of acute radiation syndrome, $\widetilde{\overline{P_{\mathrm{ARS}}}}$. $\widetilde{\overline{P_{\mathrm{ARS}}}}$ versus dose equivalent, H, which was used to quantify the population-averaged probability of the detriment of acute radiation syndrome for the j^{th} worker, $\widetilde{\overline{P_{\mathrm{D},2,J}}}(H)$. The empirical model was developed in this work based on the findings of Donnelly *et al.*[117]

For simplicity, we considered all effects to be fatal (*i.e.,* the benefit was to avoid a fatal cancer and the detriments were fatal cancer and fatal acute radiation syndrome). Thus, for simplicity and clarity in this example, we assigned the maximum value of 1 to the relative magnitudes of all beneficial and detrimental effects (*i.e.,* $\overline{S_{\mathrm{B},1}}$ in Eq. 4.13, $\overline{S_{\mathrm{D},1}}$, and $\overline{S_{\mathrm{D},2}}$ in Eq. 4.15). Table 4.3 lists the parameters involved in calculating $\widetilde{\overline{FOM}}$ for this hypothetical scenario.

In order to decide the number of workers and assigned times, we utilized a commercially available optimization toolbox (MATLAB version R2016a, The MathWorks Inc., Natick, Massachusetts, United States) to perform an iterative optimization of the shift assignments. We discretized the duration of assignments to 30-minute intervals. Thus, each worker was assigned to either task A or task B for each 30-minute interval of their 8-hour shift. This optimization searched through the 10-dimensional parameter space comprising 137 billion possible shift-

assignment combinations $\left(\{t_{\mathrm{A},j}\}\forall j \text{ and where } t_{\mathrm{B},j} = 8\text{ h} - t_{\mathrm{A},j}\right)$. The largest $\widetilde{\overline{FOM}}$ magnitude indicated the optimal shift-assignment combination, *i.e.,* the exposures were justified, optimized, and limited.

Table 4.3. List of parameters and equations for calculating the cumulative lifetime projection of the population-averaged figure of merit ($\widetilde{\overline{FOM}}$) for the illustrative example in emergency response. Data include the term, description, and the corresponding value, equation, or figure.

Term	Description	Value, Equation, or Figure
N_{B}	Population of benefitted inhabitants	78,000
N_{D}	Number of radiation workers experiencing the detriment	10
$H_{\mathrm{L},1}$	Exposure limit applied to radiation workers	20 mSv/yr[100]
$H_{\mathrm{L},2}$	Exposure limit applied to the public (*i.e.,* inhabitants in the nearby town)	1 mSv/yr[100]
$n_{\mathrm{L},1}$	Exponent driving the rate of change of the penalty factor for exceeding $H_{\mathrm{L},1}$ (see Eq. 4.5)	10
$n_{\mathrm{L},2}$	Exponent driving the rate of change of the penalty factor for exceeding $H_{\mathrm{L},2}$ (see Eq. 4.5)	10
$\overline{PF}$	Penalty factor for exceeding applicable exposure limits (*i.e.*, $H_{\mathrm{L},1}$ and $H_{\mathrm{L},2}$)	Eq. 4.16
$\widetilde{\overline{P_{\mathrm{B}}}}$	Cumulative probability of avoided risk of harmful effect (*i.e.*, fatal radiogenic cancer incidence) attributed to the operation	Eq. 4.18
$\overline{S_{\mathrm{B}}}$	Magnitude of the harmful effect for which risk is avoided by the operation (*i.e.,* fatal cancer)	1
$\overline{O_{\mathrm{B}}}$	Factor for other considerations related to the benefit	1
$\widetilde{\overline{F_{\mathrm{B,ER}}}}$	Cumulative population-averaged figure of benefit for the example scenario in emergency response	Eq. 4.13
$\widetilde{\overline{P_{\mathrm{D},1}}}$	Cumulative probability of cancer incidence resulting from exposures incurred while completing the shift assignment	Eq. 4.22
$\overline{S_{\mathrm{D},1}}$	Magnitude of the incident cancer attributed to the shift assignment (*i.e.*, potentially fatal)	1
$\overline{O_{\mathrm{D},1}}$	Factor for other considerations related to the detriment of cancer incidence	1
$\widetilde{\overline{P_{\mathrm{D},2}}}$	Cumulative probability of acute radiation syndrome resulting from exposures incurred while completing the shift assignment	See Figure 4.3
$\overline{S_{\mathrm{D},2}}$	Magnitude of acute radiation syndrome attributed to the shift assignment (*i.e.,* potentially fatal)	1
$\overline{O_{\mathrm{D},2}}$	Factor for other considerations related to the detriment of acute radiation syndrome	1
$\widetilde{\overline{F_{\mathrm{D,ER}}}}$	Population-averaged figure of detriment for the illustrative example in emergency response	Eq. 4.15

4.2.2.2 Diagnostic Radiology

An example application of the figure-of-merit framework to the field of diagnostic radiology is as a decision aid in justifying a new screening procedure. The goal of this hypothetical example was to identify the most appropriate breast-cancer screening procedure for universal screening of women between the ages of 50 and 74[118]. We considered two alternative methods for this example: the current standard of care, namely, digital mammography alone (DM), versus a proposed new standard of care, digital breast tomosynthesis (DBT) in conjunction with digital mammography, denoted by (DBT+DM).

This decision requires the justification of exposures to each individual in a large population of apparently healthy women. Justification considered the ethical principles of autonomy (*i.e.,* patients must be informed of the benefits and risks and their personal decision respected) as well as the principles of beneficence and non-maleficence (*i.e.,* the benefits should outweigh the detriments). These diagnostic radiology procedures comprise small medical exposures, and therefore the principle of limitation was not applied here.

We used our comprehensive framework to objectively justify the selection of the most appropriate procedure. Specifically, we calculated the cumulative lifetime projection of the population-averaged figure of merit ($\widetilde{\overline{FOM}}$, see Eq. 4.17) for each procedure in order quantify the net benefit to each patient and then compared the resulting $\widetilde{\overline{FOM}}$ magnitudes. We calculated the $\widetilde{\overline{FOM}}$ in this example for lifetime projections of the benefits and detriments using Eqs. 4.13 and 4.15 (*i.e.,* the temporal factors, $\overline{T_{\mathrm{D}}(t)}$ and $\overline{T_{\mathrm{B}}(t)}$, in Eqs. 4.12 and 4.14 were implicitly included in the cumulative probability calculations). We calculated the cumulative population-averaged figure of benefit for the example in diagnostic radiology, $\widetilde{\overline{F_{\mathrm{B,DR}}}}$, using Eq. 4.13 in consideration

of a single benefit, the correct detection of a potentially fatal (but curable in 50% of cases if treated) breast cancer. We estimated the cumulative population-averaged probability of this benefit, $\widetilde{\overline{P_{\mathrm{B}}}}$, with the population-averaged positive predictive value ($\overline{PPV}$)[119] of each screening procedure. The $\overline{PPV}$ quantifies the probability that subjects with a positive test result actually have the disease. We represented the magnitude of this benefit, $\overline{\mathrm{S_B}}$, as the relative magnitude of the harmful effect that is avoided by a successful screening procedure (*i.e.,* the lethality factor of breast cancer, taken from ICRP Report 60[100]).**

We calculated the cumulative population-averaged figure of detriment for this example, $\widetilde{\overline{F_{\mathrm{D,DR}}}}$, using Eq. 4.14 in consideration of a single detriment, radiogenic breast-cancer induction. The cumulative probability of this detriment, $\widetilde{\overline{P_{\mathrm{D}}}}$, was the probability of radiogenic breast-cancer induction resulting from the use of each procedure as a universal screening tool[120] and the relative magnitude of this detriment, $\overline{\mathrm{S_D}}$, was the lethality of breast cancer[100]. Table 4.4 lists the magnitudes of the factors involved in calculating $\widetilde{\overline{FOM}}$ for DM and DBT+DM. We identified the procedure with the higher $\widetilde{\overline{FOM}}$ as the most appropriate breast-cancer screening procedure for universal screening.

4.2.2.3 Cancer Radiotherapy

In a final example, we applied the new framework to aid decision making in cancer radiotherapy. The goal of this hypothetical example was to decide between two alternative personalized treatment options (*i.e.,* planned exposures) available to a 60-year-old man with prostate cancer: conventional photon radiotherapy (CRT) and watchful waiting (WW). Such a decision entails, among many other factors, the justification of any exposure to the patient. Cancer radiotherapy

** These were used for simplicity. More accurate data are available and could be used in this framework.

Table 4.4. List of parameters and equations for calculating the cumulative lifetime projection of the population-averaged figure of merit ($\widetilde{\widetilde{FOM}}$) for the illustrative example in diagnostic radiology. Data include the term, description, and the corresponding value or equation for digital mammography alone (DM) and digital breast tomosynthesis in conjunction with digital mammography (DBT+DM).

Term	Description	Value/Equation	
		DM	DBT+DM
N_{B}	Number of people experiencing the benefit of the planned exposure (*i.e.,* the patient)	1	1
N_{D}	Number of people experiencing the detriment of the planned exposure (*i.e.,* the patient)	1	1
$H_{\mathrm{L},}$	Applicable exposure limit	-	-
n_{L}	Exponent driving the rate of change of the penalty factor for exceeding H_{L}	0 (Eq. 4.5)	0 (Eq. 4.5)
$\overline{PF}$	Penalty factor for exceeding applicable exposure limit (*i.e.*, H_{L})	1 (Eq. 4.16)	1 (Eq. 4.16)
$\widetilde{\overline{P_{\mathrm{B}}}}$	Cumulative probability of correctly detecting breast cancer (*i.e.,* the positive predictive value)	4.1%[119]	6.4%[119]
$\overline{S_{\mathrm{B}}}$	Magnitude of the benefit (*i.e.*, harmful effect avoided by successful screening, lethality of breast cancer)	0.50[100]	0.50[100]
$\overline{O_{\mathrm{B}}}$	Factor for other considerations related to the benefit	1	1
$\widetilde{\overline{F_{\mathrm{B,DR}}}}$	Cumulative population-averaged figure of benefit for the illustrative example in diagnostic radiology	Eq. 4.13	Eq. 4.13
$\widetilde{\overline{P_{\mathrm{D}}}}$	Cumulative probability of radiogenic breast-cancer incidence resulting from screening exposure	25/100,000[120]	75/100,000[120]
$\overline{S_{\mathrm{D}}}$	Magnitude of the detriment attributed to the screening procedure (*i.e.*, lethality of breast cancer)	0.5[100]	0.5[100]
$\overline{O_{\mathrm{D}}}$	Factor for other considerations related to the detriment of radiogenic cancer incidence	1	1
$\widetilde{\overline{F_{\mathrm{D,DR}}}}$	Cumulative population-averaged figure of detriment for the illustrative example in diagnostic radiology	Eq. 4.15	Eq. 4.15

comprises a medical exposure, for which the ICRP recommends no exposure limits. As in the previous example, we did not apply exposure limits and we did respect the ethical principles of autonomy, beneficence, and non-maleficence.

We employed our comprehensive figure of merit to provide an algorithmic and personalized approach to justify the treatment plan selected. Specifically, we compared the balance between the patient-specific benefits and detriments (*i.e.*, beneficence and non-maleficence) for each treatment option by calculating the population-averaged figure of merit ($\overline{FOM(a,e)}$) for CRT

and WW in each year after treatment. We calculated the population-averaged figure of benefit for each treatment option (*i.e.*, CRT and WW) using Eq. 4.12 in consideration of a single benefit, control of the tumor. We estimated the population-averaged probability of benefit from CRT, $\overline{P_{\mathrm{B,CRT}}(a,e)}$, with the tumor control probability, $\overline{TCP(a,e)}$. For this example, we assumed $\overline{TCP(a,e)}$ was 95% and constant in time following treatment. We considered the probability of benefit from watchful waiting, $\overline{P_{\mathrm{B,WW}}(a,e)}$, to be the probability of survival, calculated by,

$$\overline{P_{\mathrm{B,WW}}(a,e)} = 1 - \overline{L_{\mathrm{T}}} \qquad 4.23$$

where $\overline{L_{\mathrm{T}}}$ was the lethality factor of prostate cancer, taken from ICRP Report 60[100]. In this case, e can be thought of as the age at diagnosis and we assumed $\overline{P_{\mathrm{B,WW}}(a,e)}$ was constant in time after treatment. Figure 4.4 plots $\overline{P_{\mathrm{B,RT}}(a,e)}$ for an illustrative selection of treatment outcomes for a 60-year-old cancer patient.

In this example, we assumed that the tumor in the prostate was potentially fatal, and thus the benefit was avoiding a potential lethality. We accordingly assigned the maximum value of 1 to the magnitude of the benefit, $\overline{\mathrm{S_B}}$. We represented the temporal factor, $\overline{T_{\mathrm{B}}(a,e)}$, in Eq. 4.12 as the probability of surviving to attained age a = 100 years conditional on survival to the age of exposure, e = 60 years. This corresponds to the factor $\frac{\overline{S(a)}}{S(e)}$ from the BEIR VII report[121]. We calculated this factor from data contained in the life tables tabulated by the U.S. Department of Health and Human Services[122-125]. Figure 4.5 demonstrates how this factor might differ for different populations[124, 125]. In essence, the temporal factor discounts the risk of effect (in this case, the detriment of risk of radiogenic cancer induction) because of competing causes of death (*e.g.,* heart failure) that may occur before a radiogenic cancer develops.

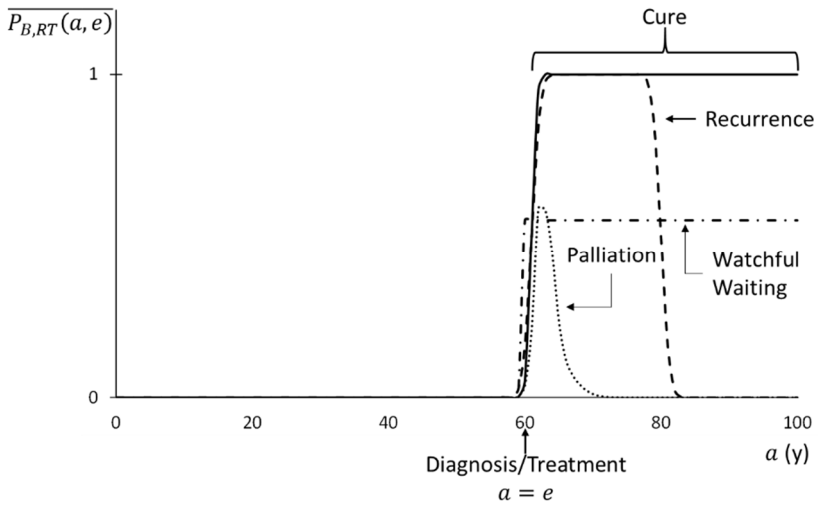

Figure 4.4. Probability of benefit for an illustrative selection of treatment outcomes for a 60-year-old man with prostate cancer. Probability of benefit, $\overline{P_{\mathrm{B,RT}}(a,e)}$, versus attained age, a, for outcomes of tumor cure (*i.e.*, complete response after time at exposure, a=e), tumor recurrence (*i.e.*, complete response followed by recurrence 20 years post-exposure), watchful waiting (*i.e.*, constant probability of survival after time of diagnosis, a=e), and palliation (*i.e.*, short-term, partial response).

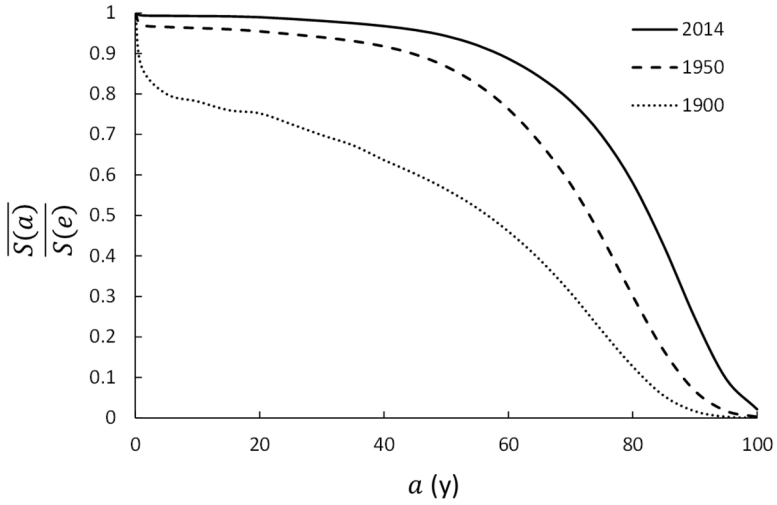

Figure 4.5. Representative examples of the temporal factor for different populations. Temporal factor, $\frac{\overline{S(a)}}{S(e)}$, versus attained age, a, calculated from birth to age 100 based on the average survival in the United States in years 1900[125], 1950[125], and 2014[124].

We calculated the population-averaged figure of detriment for this example, $\overline{F_{\mathrm{D,RT}}(a,e)}$, using Eq. 4.14 in consideration of one detrimental effect, radiogenic cancer of the bladder. We

quantified the probability of this detriment for CRT, $\overline{P_{\mathrm{D,CRT}}(a,e)}$, with the excess absolute risk (EAR) of radiogenic bladder-cancer incidence for a 60-year-old male using the BEIR VII methodology[121] for an average bladder dose of 70 Gy. We considered this a conservative estimate of dose to the bladder from photon CRT based on a random sample of 10 prostate-cancer patients previously treated at our clinic (Mary Bird Perkins Cancer Center, Baton Rouge, LA). The bladder dose for WW was 0 Gy and thus $\overline{P_{\mathrm{D,WW}}(a,e)}$ was 0. We represented the relative magnitude of radiogenic cancer of the bladder, $\overline{\mathrm{S_D}}$, as the lethality of bladder cancer[100] and calculated the temporal factor for the detriment, $\overline{T_{\mathrm{D}}(a,e)}$, with $\frac{\overline{S(a)}}{S(e)}$ (see above). Table 4.5 lists the parameters and equations needed to calculate the population-averaged figure of merit ($\overline{FOM(a,e)}$). From this, we calculated the cumulative projected figure of merit ($\widetilde{\overline{FOM}}$, see Eq. 4.17) and selected the personalized treatment option with the higher $\widetilde{\overline{FOM}}$ as the optimal treatment for this patient.

4.3. Results

4.3.1. Emergency Response

Figure 4.6 plots the cumulative lifetime population-averaged figures of benefit, $\widetilde{\overline{F_{\mathrm{B,ER}}}}$, and detriment, $\widetilde{\overline{F_{\mathrm{D,ER}}}}$, associated with tasks A and B versus the amount of time the j^{th} worker is assigned to task A, $\mathrm{t_{A,}}_j$. These data reveal the opposite monotonic progressions of the benefit and detriment associated with the tasks. The magnitude of $\widetilde{\overline{F_{\mathrm{B,ER}}}}$ for task A crosses that for task B at $\mathrm{t_{A,}}_j = 3$ hours while the $\widetilde{\overline{F_{\mathrm{D,ER}}}}$'s for tasks A and B cross at $\mathrm{t_{A,}}_j = 1.5$ hours. From inspection of these plots alone, the optimal shift assignments are not apparent. Naively, considering only

Table 4.5. List of parameters and equations for calculating the population-averaged figure of merit ($\overline{FOM(a,e)}$) for the illustrative example in cancer radiotherapy. Data include the term, description, and the corresponding value or equation for the two candidate treatment options: conventional photon radiotherapy (CRT) and watchful waiting (WW).

		Value/Equation	
Term	Description	CRT	WW
N_{B}	Number of people experiencing the benefit of the planned exposure (*i.e.,* the patient)	1	1
N_{D}	Number of people experiencing the detriment of the planned exposure (*i.e.,* the patient)	1	1
$H_{\mathrm{L,}}$	Applicable exposure limit	-	-
n_{L}	Exponent driving the rate of change of the penalty factor for exceeding H_{L}	0 (Eq. 4.5)	0 (Eq. 4.5)
$\overline{PF}$	Penalty factor for exceeding applicable exposure limit (*i.e.*, H_{L})	1 (Eq. 4.16)	1 (Eq. 4.16)
$\overline{P_{\mathrm{B}}(a,e)}$	Probability of therapeutic benefit (*i.e.,* tumor cure)	$0.95 \forall e \leq a \leq 100$ (this work)	$0.45 \forall e \leq a \leq 100$ (Eq. 4.23)[100]
$\overline{S_{\mathrm{B}}}$	Magnitude of the benefit (*i.e.*, harmful effect avoided by successful cancer radiotherapy, potentially lethal prostate cancer)	1	1
$\overline{T_{\mathrm{B}}(a,e)}$	Factor for other circumstances mitigating the benefit of the planned exposure (*e.g.*, competing causes of mortality) as a function of time, t, since the planned exposure	$\overline{\frac{S(a)}{S(e=60)}} \forall e \leq a \leq 100$ [121]	$\overline{\frac{S(a)}{S(e=60)}} \forall e \leq a \leq 100$ [121]
$\overline{O_{\mathrm{B}}}$	Factor for other considerations related to the benefit	1	1
$\overline{F_{\mathrm{B,RT}}(a,e)}$	Population-averaged figure of benefit for the illustrative example in cancer radiotherapy	Eq. 4.12	Eq. 4.12
$\overline{P_{\mathrm{D}}(a,e)}$	Probability of radiogenic bladder-cancer incidence resulting from radiotherapy exposure	EAR[121]	0
$\overline{S_{\mathrm{D}}}$	Magnitude of the detriment attributed to the radiotherapy exposure (*i.e.*, lethality of bladder cancer)	0.5[100]	0.5[100]
$\overline{T_{\mathrm{D}}(a,e)}$	Factor for other circumstances mitigating the detriment of radiogenic cancer incidence (*e.g.*, competing causes of mortality) as a function of time, t, since the planned exposure	$\overline{\frac{S(a)}{S(60)}(t=a)}$ [121]	$\overline{\frac{S(a)}{S(60)}(t=a)}$ [121]
$\overline{O_{\mathrm{D}}}$	Factor for other considerations related to the detriment of radiogenic cancer incidence	1	1
$\overline{F_{\mathrm{D,RT}}(a,e)}$	Population-averaged figure of detriment for the illustrative example in cancer radiotherapy	Eq. 4.14	Eq. 4.14

benefits, one would seek to select a shift assignment that maximizes the benefits from both tasks and might subjectively choose to assign all 10 workers to $\mathrm{t}_{\mathrm{A},j} = 3$ h. Considering only the

detriments, on the other hand, one would seek to keep the detriments from both tasks low and thus might believe $\mathrm{t}_{\mathrm{A},j} = 1.5$ h is desirable. Therefore, considering the benefit and detriment together, we might expect a subjective analysis to arrive at a shift assignment of $1.5 \text{ h} \leq \mathrm{t}_{\mathrm{A},j} \leq 3$ h.

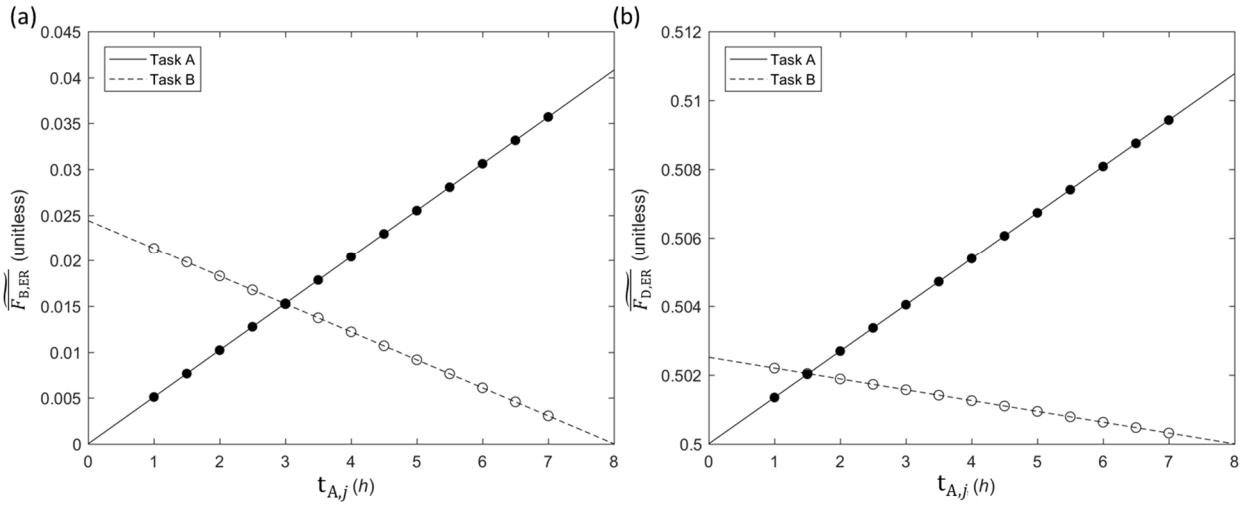

Figure 4.6. Figures of benefit to inhabitants and detriment to workers for the illustrative example in emergency response. Figures of (a) benefit, $\widetilde{\overline{F}_{\mathrm{B,ER}}}$, and (b) detriment, $\widetilde{\overline{F}_{\mathrm{D,ER}}}$, attributed to effort spent on tasks A and B versus the amount of time the j^{th} worker is assigned to Task A, $\mathrm{t}_{\mathrm{A},j}$. Points indicate the possible 30-minute shift intervals.

Figure 4.7 plots the lifetime projection of the population-averaged figure of merit ($\widetilde{\overline{FOM}}$, Eq. 4.17) for an illustrative subset of possible shift-assignment combinations (*i.e.,* those for which all 10 workers received identical relative shift assignments, $\mathrm{t}_{\mathrm{A},1} = \mathrm{t}_{\mathrm{A},j} = \mathrm{t}_{\mathrm{A},10}$). $\widetilde{\overline{FOM}}$ takes benefits, detriments, and applicable exposure limits into account and allows for a comprehensive evaluation of this planned exposure. In Figure 4.7, the optimal shift assignment is readily apparent ($\mathrm{t}_{\mathrm{A},j} = 6$ h), as indicated by the maximum $\widetilde{\overline{FOM}}$ magnitude, and is distinctly different from our subjective conclusion based on Figure 4.6. Indeed, our iterative optimization converged on assigning all 10 workers to the same relative shift assignments (*i.e.*, each of the 10 workers

assigned to 6 hours on task A and 2 hours on task B). This resulted in a planned 19.4 mSv/worker over the course of the 8-hour shift. This result reflects the principle of limitation by keeping each worker below applicable limits (*i.e.,* an average of 20 mSv/y over 5 y and not to exceed 50 mSv in any one year[100]). Furthermore, the optimized shift assignments are just in that they evenly distribute the exposures across the group rather than sacrificing any individual for the greater good. This combination of shift assignments reduced the exposure to the inhabitants by 73.4% to 0.27 Sv over the course of the entire one-hour exposure.

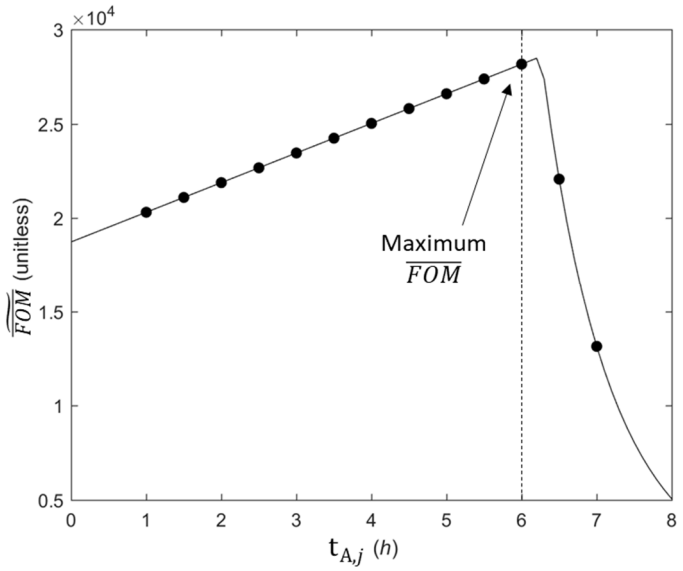

Figure 4.7. Population-averaged figure of merit for the illustrative example in emergency response. Population-averaged figure of merit, $\widetilde{\overline{FOM}}$, versus the amount of time worker j is assigned to Task A, $t_{A,j}$ for a representative set of shift-assignment combinations considered by the iterative optimization algorithm. Points indicate the possible 30-minute shift intervals. The vertical dashed line indicates the optimal shift assignment.

4.3.2. Diagnostic Radiology

The cumulative population-averaged figure of benefit ($\widetilde{\overline{F_B}}$) for digital breast tomosynthesis in conjunction with digital mammography (DBT+DM) in this hypothetical scenario was a factor of 1.6 larger than that for digital mammography alone (DM). The cumulative population-averaged

figure of detriment ($\widetilde{\overline{F_{\mathrm{D}}}}$) for DBT+DM, however, was three times that for DM. As with the example in emergency response, these data, which represent the benefit and detriment separately, do not reveal the optimal selection. The lifetime projection of the population-averaged figure of merit ($\widetilde{\overline{FOM}}$), we shall see, overcame this limitation by aggregating the benefit and detriment.

The $\widetilde{\overline{FOM}}$ for DBT+DM and DM were 0.032 and 0.020, respectively. Put another way, the $\widetilde{\overline{FOM}}$ for DBT+DM was a factor of 1.6 larger than that for DM. This suggests that the added benefit of DBT (*i.e.,* the increased positive predictive value ($\overline{PPV}$)) outweighs the additional detriment (*i.e.,* the increased risk of radiogenic breast-cancer incidence) for individuals in the population. More specifically, the use of DBT+DM as a universal screening tool is projected to induce an additional 50 radiogenic breast cancers while accurately diagnosing an additional 2,300 breast cancers in a population of 100,000 women. These results demonstrate the clear consideration of the principles of beneficence and non-maleficence in an algorithmic and objective framework for justifying the use of DBT+DM as a universal screening method.

4.3.3. Cancer Radiotherapy

Figure 4.8 plots the population-averaged figures of benefit, $\overline{F_{\mathrm{B,RT}}(a,e)}$, and detriment, $\overline{F_{\mathrm{D,RT}}(a,e)}$, for the hypothetical example of the lifespan of a 60-year-old man with prostate cancer following two different treatment approaches: conventional photon radiotherapy (CRT) and watchful waiting (WW). These data show that while the benefit for CRT is larger than that for WW, so too is the detriment. Furthermore, while the benefit for both CRT and WW peak in the year of diagnosis/treatment (a = 60 y) and monotonically decrease thereafter, the detriment from CRT peaks 25 years later (a = 85 y), obfuscating the optimal treatment choice for this patient. It should be noted that the decrease in the figures of benefit for both treatment options is

due to the increasing importance of other sources of mortality later in life. This manifests by the magnitudes of the temporal factors, $\overline{T_{\mathrm{B}}(a,e)}$ and $\overline{T_{\mathrm{D}}(a,e)}$ (see Eqs. 4.12 and 4.14), which sharply decrease towards the end of life.

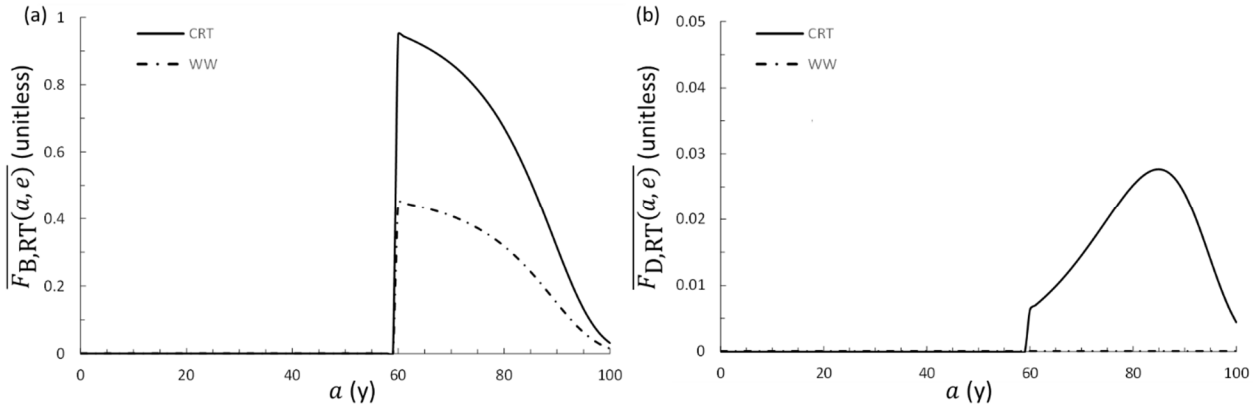

Figure 4.8. Figures of benefit and detriment for the illustrative example scenario in cancer radiotherapy. Figures of (a) benefit, $\overline{F_{\mathrm{B,RT}}(a,e)}$, and (b) detriment, $\overline{F_{\mathrm{D,RT}}(a,e)}$, versus attained age, a, for two alternative hypothetical treatment approaches for a 60-year-old man with prostate cancer: conventional photon radiotherapy (CRT) and watchful waiting (WW).

Figure 4.9 shows the population-averaged figure of merit, $\overline{FOM(a,e)}$, over the life of a 60-year-old man with prostate cancer following conventional photon therapy (CRT) compared to that for watchful waiting (WW). This figure shows that $\overline{FOM(a,e)}$ was 0 until the age of diagnosis/treatment (a = 60 y) for both treatment plans. After this time, the largest $\overline{FOM(a,e)}$ occurred in the year of diagnosis/treatment. The same monotonic decrease that was seen in the figures of benefit is evidenced in the $\overline{FOM(a,e)}$'s for both CRT and WW, mainly due to competing causes of death. Still, CRT resulted in a larger $\overline{FOM(a,e)}$, even at an attained age of 85 years, where its associated detriment was at a maximum. The figure of merit accumulated over the patient's lifetime ($\widetilde{FOM}$) for CRT was a factor of two larger than that for watchful waiting (23.51 versus 11.32, respectfully), thereby justifying the CRT treatment and its associated risk and ensuring a thorough consideration of the ethical principles of beneficence and

non-maleficence for this patient. We estimate that the increased $\widetilde{\overline{FOM}}$ for CRT represents adding 27 healthy years of life to the patient's life expectancy compared to that for WW.

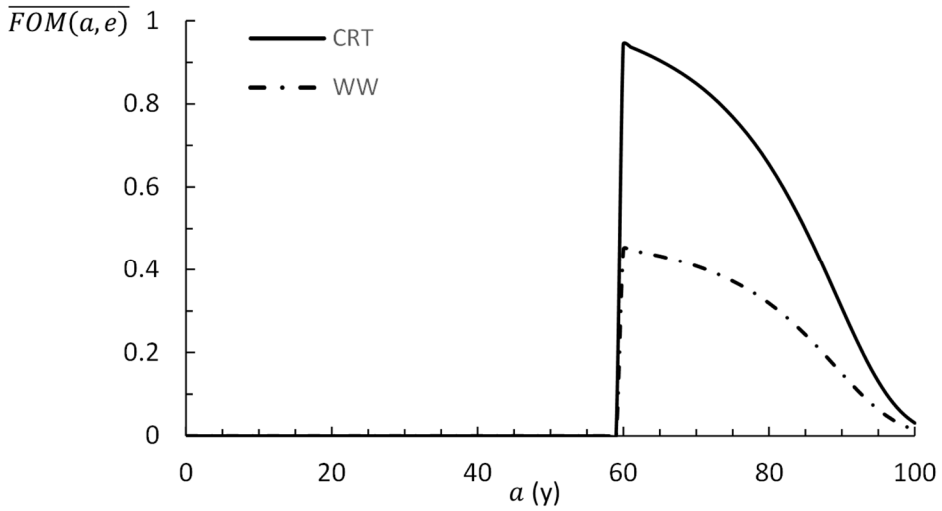

Figure 4.9. Population-averaged figures of merit for the illustrative examples in cancer radiotherapy. Population-averaged figure of merit,$\overline{FOM(a,e)}$, versus attained age, a, for two alternative treatment approaches for a 60-year-old man with prostate cancer: conventional photon radiotherapy (CRT) and watchful waiting (WW).

4.4. Discussion

In this study, we developed a new, comprehensive conceptual framework and corresponding quantitative methods to aggregate the benefits and detriments of planned radiation exposures to individuals, groups, and populations. We did this by way of a comprehensive figure of merit (FOM) that takes the major host- and exposure-related parameters into account. We then demonstrated the utility of this new framework in three illustrative planned-radiation-exposure examples: emergency response, diagnostic imaging, and cancer radiation therapy. The major finding of this work is that, for the first time, it is possible to quantitatively combine the various benefits and detriments of any planned radiation exposure to an individual or society in a way that enables justification and/or optimization of that exposure in an objective and automated manner.

This new framework has several important implications. First, the generalized, comprehensive nature of the algorithm developed here enables optimization and justification of arbitrarily complex exposure situations. This has the potential to open new avenues of inquiry in a variety of planned-exposure settings. For example, the algorithm could be used to facilitate the introduction of new radiation technologies (*e.g.*, medical procedures) by providing a framework to aid in justifying changes to standard practices, or to improve health outcomes for patients by guiding patient-specific, outcome-based decisions. There are also many industrial sectors that utilize radiation, including sterilization (*e.g.,* to disinfect food[126] and medical equipment[127]), environmental safety (*e.g.,* to remove toxic pollutants from the air[128]), fashion (*e.g.,* to treat clothing[129]), and agriculture (*e.g.,* to improve food production[130]) to which this framework could be applied. Another important implication of this new framework is that it provides a means to more fully respect the ethical principle of autonomy. Respecting an individual's autonomy requires clear and accessible communication of all of the possible outcomes (*i.e.*, beneficial and detrimental) of a planned exposure and giving them the freedom to make their own decisions on the basis of informed deliberation[1]. An important requisite step to this is the quantification of all possible effects and their relative magnitudes. The framework developed in this work can in principle automatically provide the complete information necessary for empowering individuals to exercise autonomy.

The major strength of the framework developed in this work is that the methods are generally applicable. The figure of merit (FOM) can consider arbitrary numbers of benefits and detriments of varying magnitudes for an individual, group, or population. Thus, the FOM is directly related to the overall projected health outcome of the exposed individual(s), including benefit, morbidity, and mortality. Finally, the framework is consistent with existing radiation-protection

practices. These characteristics greatly increase the FOM's scope of applicability, as demonstrated by the example calculations presented here.

This study has several limitations. First, the accuracy of the FOM is limited by the accuracy of the absolute dose-response models used to calculate the benefits and detriments. We did not consider this a significant limitation for two reasons. First, our methods involved comparing the relative FOM magnitudes between two or more options (*e.g.,* different shift-assignment combinations, DM vs DBT+DM, and CRT vs WW) rather than drawing any conclusions from the absolute FOM magnitudes. When used in this way, the covariance decreases the overall uncertainty, rendering the results less sensitive to uncertainties in the dose-response models. Second, the FOM was designed in such a way that new, more accurate models can easily be integrated into the framework as they become available. This is a focus of radiation-biology and radiation-epidemiology research[18, 131]. Another limitation of this study is that we did not explicitly take economic considerations (*e.g.,* costs or savings) into account in our examples. Cost-effectiveness of a planned exposure is an important consideration in many settings. Although we did not consider economic effects in the examples in this study, the formalism includes a provision for this and other factors (*i.e.*, in $O_{\mathrm{B},k}$ and $O_{\mathrm{D},m}$ in Eqs. 4.2 and 4.3 and $\overline{O_{\mathrm{B},k}}$ and $\overline{O_{\mathrm{D},m}}$ in Eqs. 4.12 through 4.15). There is strong interest to include such considerations; the European Society for Radiotherapy and Oncology (ESTRO) recently launched a Health Economics in Radiation Oncology (HERO) project, which aims to develop a database and model for health-economic evaluations in radiotherapy[132]. Efforts like the HERO project will greatly facilitate the consideration of economic burden and gain in the proposed framework.

4.5. Conclusion

We developed a comprehensive figure of merit, FOM, for guiding decisions on planned radiation exposures and evaluated its utility in three illustrative examples. This FOM fills a chronic gap in the application of radiation-protection theory, namely, the lack of a generally applicable framework and set of corresponding quantitative methods to algorithmically justify and optimize any planned-exposure scenario. This new framework enables the comprehensive and algorithmic risk-benefit analysis of planned radiation exposures to individuals, groups, and populations and translates the subjective guiding principle of optimization, or "as low as reasonably achievable" (*i.e.,* ALARA), into a more rigorous foundation. Our application of the proposed framework to three illustrative example scenarios suggests that it could find use in a wide range of planned-exposure settings, including medicine and industry. The FOM developed in this work could provide a more objective approach to complex, subjective pillars of radiation protection (*i.e.,* justification and optimization), while maintaining coherence with existing methods, which are largely based on the principle of limitation. This has the potential to enable the full realization of the long-term benefit of planned radiation exposures to individuals and society.

Chapter 5. Generalized Approach to Radiotherapy Treatment Planning by Optimizing Health Outcome Instead of Dose: Preliminary Results for External-Beam Prostate Radiotherapy

5.1. Introduction

Advancements in cancer care in recent decades have increased survival rates to nearly 70% overall and 85% in children[4]. This increase was mainly driven by improved cures for primary cancers. Epidemiological studies have revealed that the majority of cancer survivors suffer from myriad health conditions, even decades after the completion of treatment[7, 133-140]. These health conditions can have profound impacts on the survivor's length and quality of life by affecting their mortality[141], cognition[142, 143], employability[144], fertility[145], and access to survivorship care[146], to name a few. This has highlighted the fact that tumor cure is not the only hallmark of cancer survivorship[147]. In fact, the full beneficial potential of any medical intervention can only be realized by additionally minimizing the long- and short-term side effects in healthy tissues[18]. This has led to a need for innovative approaches to the planning of cancer care that consider normal-tissue effects to provide improved outcomes in addition to tumor cure[18, 147].

Current approaches in radiotherapy do attempt to prospectively limit side effects by constraining the dose received by normal tissues to be less than empirically determined tolerance dose values. More specifically, constrained iterative optimization of dose distributions is used as a surrogate for optimization of the patient's health outcome. These dosimetric constraints, however, rarely serve as reliable predictors of outcome due to interpatient variation in radiation sensitivity[19]. Research on direct optimization of health outcome is at an early stage. Researchers have attempted to improve outcomes directly by varying treatment factors, including the treatment modality[22, 112], prescription dose[25, 27, 30, 32, 148], fractionation scheme[28], and beam-weight combination[29, 31]. Most of these studies have focused on the short-term effects of radiotherapy

and neglected the long-term health effects, which may seriously impact a patient's quality and/or length of life[22-28]. Only three studies optimized aspects of radiotherapy delivery based on the long-term side effects[29-31], of which two included considerations of the dose from stray radiation sources[29, 32]. These stray radiation sources deliver low doses of radiation to large volumes in the patient (*i.e.,* the entire body) and increase the risk of late-occurring side effects[74, 75]. To our knowledge, no study has yet attempted to optimize radiotherapy treatment plans in consideration of all types of outcomes (*i.e.,* long- and short-term side effects) associated with the total dose (*i.e.,* therapeutic and stray) deposited in individual patients. Thus, it is not yet known whether it is feasible to optimize radiotherapy treatment plans based on the longitudinal (*i.e.*, long- and short-term) outcomes of the therapeutic and stray radiation exposures in individual patients.

The goal of this study was to develop a generally applicable method to directly optimize projected longitudinal outcomes in consideration of arbitrary numbers and types of radiogenic effects. To accomplish this, we developed an outcome-based objective function to replace dose-based constraints and penalties in radiotherapy treatment-plan optimization. This work demonstrates a practical application of this objective function to optimize photon and proton radiotherapy treatment plans in a sample of ten patients with low-risk prostate cancer.

5.2. Methods

In this study, we optimized photon and proton radiotherapy treatment plans in a sample of ten prostate-cancer patients. We begin by describing the sample and anatomical regions of interest (Section 5.2.1). Next we detail the treatment-planning (Section 5.2.2) and optimization (Section 5.2.3) methods, and the objective functions used to guide these optimizations (Section 5.2.3.1). Finally, we explain how we tested for improved projected health outcomes from outcome-optimized treatment plans compared to dose-optimized treatment plans and for the

generalizability of the proposed methods across three influence factors: treatment factors, risk-projection factors, and host factors (Section 5.2.4).

5.2.1. Patient Selection and Regions of Interest

We randomly sampled a cohort of ten early-stage prostate-cancer patients from the population of patients previously treated at our institution (Mary Bird Perkins Cancer Center, Baton Rouge, LA). We included all patients with an intact prostate and a single planning target volume (PTV). We excluded patients with artificial hip implants and patients who required a sequential boost to a sub-volume of the primary PTV. Wall *et al.*[149] previously described this cohort. The stages at diagnosis ranged from T1 to T2 with no nodal or metastatic involvement and the mean PTV volume was 73 cm^3 (standard deviation: 15 cm^3). The average age at diagnosis was 69.2 years (61-75 years).

Table 5.1 lists the regions of interest (ROI's) and the projected endpoints taken into account. The PTV is the only ROI in which we considered a beneficial endpoint, *i.e.,* tumor control. We selected the remaining ROI's, or organs at risk (OARs), based on previous studies that demonstrated increased risks following radiotherapy exposures in these organs and tissues[51, 150, 151]. For the purposes of risk projection, we included the bladder wall and rectal wall and excluded their contents (*e.g.,* urine, excrement, and gas) following the recommendations of the International Commission on Radiological Protection (ICRP) Publication 110[152]. The femoral head (cortical bone) ROI was also defined following the recommendations of ICRP Publication 110.

Table 5.1. Regions of interest (ROI's) considered in the sample of ten prostate-cancer patients. Details include the organ, projected endpoint, type of endpoint (*i.e.*, beneficial, B, or detrimental, D), and the magnitudes of parameters for calculating OF_{OORT} (see Eq. 5.1). These values include the probability, $P_{i \text{ or } j}(t)$, (where TCP stands for tumor control probability, NTCP stands for normal tissue complication probability, and EAR stands for excess absolute risk); relative endpoint magnitude, $S_{i \text{ or } j}$; factor for competing causes of death, $T_{i \text{ or } j}(t)$; and factor for other considerations, $O_{i \text{ or } j}$.

ROI	Endpoint	Type	$P_{i \text{ or } j}(t)$	$S_{i \text{ or } j}$	$T_{i \text{ or } j}(t)$	$O_{i \text{ or } j}$
PTV	Tumor control	B	TCP[153]	1.00 (This work)	$\frac{S(a)}{S(e)}$ [121, 124]	1.00
Bladder	Grade ≥2 toxicity	D	NTCP[154]	1.00[155]	$\frac{S(a)}{S(e)}$ [121, 124]	1.00
”	Radiogenic cancer	D	EAR[29, 115, 121]	0.50[100]	$\frac{S(a)}{S(e)}$ [121, 124]	1.00
Rectum	Grade ≥2 toxicity	D	NTCP[156]	1.00[155]	$\frac{S(a)}{S(e)}$ [121, 124]	1.00
”	Radiogenic cancer	D	EAR[29, 115, 121]	0.55[100]	$\frac{S(a)}{S(e)}$ [121, 124]	1.00
Femoral Head (cortical bone)	Hip fracture	D	NTCP[157]	0.60[155]	$\frac{S(a)}{S(e)}$ [121, 124]	1.00
Femoral Head (bone marrow)	Radiogenic cancer (leukemia)	D	EAR[29, 121, 158]	0.99[100]	$\frac{S(a)}{S(e)}$ [121, 124]	1.00
Remainder	Radiogenic cancer	D	EAR[29, 121]	0.72[100]	$\frac{S(a)}{S(e)}$ [121, 124]	1.00

5.2.2. Treatment planning

We performed treatment planning using a research treatment planning system (TPS) (CERR-LSU) that was previously trained and validated for 6- and 15-MV photon therapy[34] (see Chapter 3) and 100 to 250 MeV proton therapy[159]. We selected this research TPS because it calculated stray and therapeutic radiation whereas commercial systems only calculate the therapeutic radiation[38-40]. Specifically, the photon dose calculations included contributions from therapeutic and stray photons. The proton dose calculations included contributions from therapeutic protons and stray neutrons created in the treatment head following the methods of Schneider *et al.*[160] We combined therapeutic and stray doses from proton therapy following the methods of Eley *et al.*[83] We weighted the absorbed dose by a generic relative biological effectiveness (RBE) of 1.1 for protons and 1 for photons[161]. Following the methods of Schneider *et. al.*[160], we directly

calculated the radiobiological quantity of neutron equivalent dose (*H*) in Sv, which implicitly includes an RBE for neutrons.

We designed treatment beams for each patient following the methods of Rechner *et al.*[29] Namely, we placed 16 beams of each modality (*i.e.,* 6-MV photons, 15-MV photons, and spot-scanned protons) at equal intervals of gantry-angle separation around each patient (*i.e.*, every 22.5 degrees) starting at 0 degrees (see Figure 5.3). For every patient, we designed each of the 16 beams to provide full coverage of the PTV. We pre-computed the absorbed dose from each beam alone such that each one, and any weighted combination thereof, delivered the prescribed RBE-weighted absorbed dose of 76 Gy (RBE) to the clinical target volume (CTV). We exported the pre-computed dose matrices containing therapeutic- and stray-dose contributions for each beam angle, treatment modality, and patient from the TPS and imported them into an in-house code for beam-weight optimization (MATLAB version R2016a, Mathworks, Natick, MA).

5.2.3. Optimization

The in-house optimization code performed an exhaustive search over all permutations of the numbers and weights of the pre-computed beams. We selected the exhaustive search over iterative optimization approaches to avoid solutions comprising local minima, a potential source of methodological error in a problem of high susceptibility due to its large degree of mathematical degeneracy[162]. Our permutations included all combinations of 1 to 16 beams, where all relative beam weights were positive and summed to 1. We discretized the magnitude of relative beam weights from 0 to 1 in increments of 0.1. We took advantage of the mirror symmetry of the pelvis about the sagittal plane, whereby corresponding left and right beams (*i.e.*, at equal angular displacement from 0 degrees) induce roughly equivalent outcome. Specifically, we set corresponding left and right beams to equal weights (*i.e.*, each beam in a left-right pair

could bear relative weights ranging from 0 to 0.5 in steps of 0.05). Note that the beams at angles of 0 and 180 degrees (*i.e.*, anterior-posterior and posterior-anterior) did not have a corresponding left-right partner. This procedure resulted in a total of 43,758 possible discretized beam-weight combinations, henceforth referred to as treatment plans for brevity.

The optimization procedure calculated the composite dose from each treatment plan by weighting and summing the pre-computed dose matrices from each of the 16 beams for each patient and each treatment modality. Next, it calculated the magnitude of an objective function (OF) for each treatment plan. The plans were then ranked and sorted in ascending order of OF. Finally, the plan with the smallest OF was identified as the optimal treatment plan.

5.2.3.1 Objective Functions

We ranked and sorted the pre-computed treatment plans in this study by the values from two different objective functions. One was for our proposed outcome-optimized radiotherapy (OORT) treatment plans and the other was for dose-optimized radiotherapy (DORT) treatment plans, which is similar to the current standard of care. We designed the outcome-based objective function, OF_{OORT}, to be simple and intuitive, yet comprehensive to take into account arbitrary numbers of benefits and detriments of the planned treatment. Specifically, we calculated OF_{OORT} as,

$$OF_{\mathrm{OORT}} = -\sum_{t=e}^{l}\left(F_{\mathrm{B}}(t) - F_{\mathrm{D}}(t)\right) \qquad 5.1$$

where e is the attained age at exposure, l is the attained age at the end of life (assumed here to be at an age of 100 years), and $F_{\mathrm{B}}(t)$ and $F_{\mathrm{D}}(t)$ are the figures of benefit and detriment,

respectively. We calculated $F_{\mathrm{B}}(t)$ and $F_{\mathrm{D}}(t)$ according to Wilson and Newhauser[35] (see Chapter 4). We briefly review these factors here for the reader's convenience.

$F_{\mathrm{B}}(t)$ and $F_{\mathrm{D}}(t)$ are based on corresponding basic principles, namely,

$$F_{\mathrm{B}}(t) = \sum_{i=1}^{N_{\mathrm{B}}} P_i(t) \times S_i \times T_i(t) \times O_i \qquad 5.2$$

and

$$F_{\mathrm{D}}(t) = \sum_{j=1}^{N_{\mathrm{D}}} P_j(t) \times S_j \times T_j(t) \times O_j \qquad 5.3$$

where $P_i(t)$ is the probability of the i^{th} endpoint, S_i is the relative strength or magnitude of the i^{th} endpoint, $T_i(t)$ is a temporal factor that discounts radiation-related endpoints due to other non-radiation-related causes of mortality (*i.e.,* competing causes of death), and O_i is a factor for other considerations that might be important to the decision-making process (*e.g.,* cost of treatment, access to care, or patient preference). $P_j(t)$, S_j, $T_j(t)$, and O_j are the same for the detriment. N_{B} in Eq. 5.2 is the number of benefits considered (in this case 1) and N_{D} in Eq. 5.3 is the number of detriments considered (in this case 7). Table 5.1 lists the models and corresponding parameter values used to study the cohort in this work. For simplicity, we assigned a value of unity to O_i and O_j for all endpoints.

In order to assess the impact of uncertainties in the dose response on outcome optimizations, we performed a sensitivity test by calculating $P_j(t)$ using six different dose-response models. The most widely accepted of these models was the linear-non-threshold (LNT) model. We calculated

$P_j(t)$ for the risks of radiogenic cancer of the bladder, rectum, and remainder using LNT following the BEIR VII methodology[121]. We calculated the risk of leukemia using the linear-quadratic model recommended by the BEIR VII report[121] following the methods of Taddei *et al.*[158] We next modified the LNT risk by applying two different linear-exponential relationships and two different linear-plateau relationships[29, 51], which is conceptually consistent with sub-linear behavior at high (cytotoxic) exposures. Finally, we applied a mechanistic model for radiogenic cancer induction following the methods of Dasu *et al.*[115] Figure 5.1 plots representative examples of these six risk models and demonstrates the range of dose-response relationships considered in this study. Thus, we obtained a unique OORT treatment plan for each combination of patient, modality, and risk model.

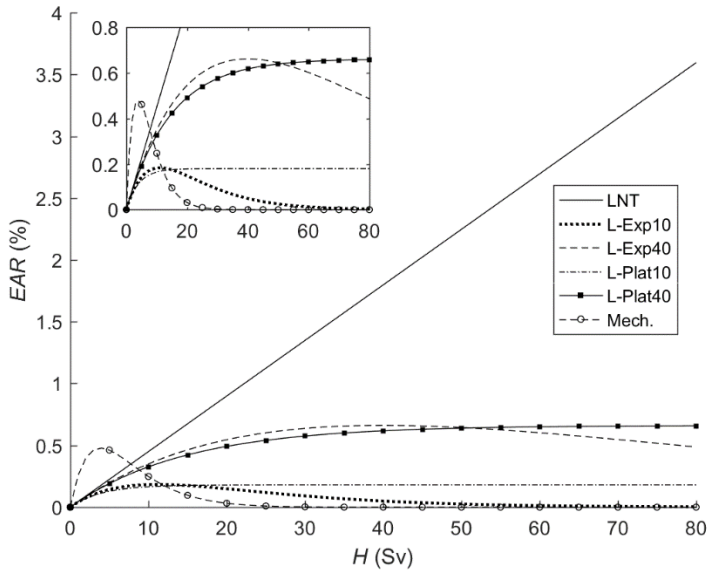

Figure 5.1. Representative examples of dose-response relationships. Excess absolute risk (*EAR*) versus dose equivalent (*H*) for six different models for the risk of radiogenic cancer induction. Models include linear-non-threshold[121] (LNT), linear exponential[51] with maxima at 10 Gy (L-Exp10) and at 40 Gy (L-Exp40), linear plateau[51] with maxima at 10 Gy (L-Plat10) and at 40 Gy (L-Plat40), and the mechanistic model of Dasu *et al.*[115] (Mech.). Examples are for radiogenic cancer of the bladder. Results for rectum, remainder, and leukemia are qualitatively similar.

The second objective function, OF_{DORT}, was based on dosimetric constraints and provided a mode of comparison with current standards of care. We calculated OF_{DORT} following the methods of Wu and Mohan[163] with,

$$OF_{\mathrm{DORT}} = \sum_{n=1}^{N} p_n^T f_n^T + \sum_{m=1}^{M} p_m^{OAR} f_m^{OAR} \qquad 5.4$$

where p_n^T is the weight for f_n^T, f_n^T is the dosimetric objective for the n^{th} target volume, p_m^{OAR} is the weight for f_m^{OAR}, and f_m^{OAR} is the dose-volume objective for the m^{th} organ at risk (OAR). In our case, the weights p_n^T and p_m^{OAR} were numerically equivalent to our strength factors S_i and S_j, respectively (see Eqs. 5.2 and 5.3 and Table 5.1). We calculated f_n^T for a single target dose of 76 Gy. We calculated f_m^{OAR} for ten dose-volume constraints (see Table 5.2). Thus, we obtained one DORT treatment plan for each patient and each treatment modality.

Table 5.2. Dose-volume constraints used for dose-optimized radiotherapy treatment planning. Constraints were used for calculating the dose-volume objective, f_m^{OAR}, for the objective function OF_{DORT} (see Eq. 5.4) whereby the normal tissue should receive no greater than the dose specified to the specified volume. Adapted from Rechner *et al.*[29]

Normal Tissue	Dose (Gy or Sv)	Relative Volume (%)
Bladder	70	15
Rectum	40	60
”	45	50
”	60	40
”	70	15
”	75.6	10
”	78	5
Rectal Wall	60	70
”	79	30
Femoral Heads	45	50

5.2.4. Tests for Improved Projected Outcomes

We quantified the projected health outcome resulting from each optimized treatment plan (*i.e.,* 210 total treatment plans: 180 OORT and 30 DORT) by calculating the figure of merit (FOM) of

Wilson and Newhauser[35] (see Chapter 4). The FOM provides a framework for combining arbitrary numbers and types of benefits and detriments from a planned radiation exposure, accumulated over time, into a single metric. It is calculated for an individual radiotherapy patient according to,

$$FOM = \sum_{t=e}^{l} FOM(t)\,\Delta t \tag{5.5}$$

where the figure of merit at a point in time is,

$$FOM(t) = F_{\mathrm{B}}(t) \times \left(1 - F_{\mathrm{D}}(t)\right) \tag{5.6}$$

and where e, l, $F_{\mathrm{B}}(t)$ and $F_{\mathrm{D}}(t)$ are as previously defined (see Eqs. 5.2 and 5.3). We calculated the FOM for each of the 210 optimized treatment plans in consideration of the endpoints listed in Table 5.1.

We used the ratio of FOM's ($RFOM$) to compare the projected long-term outcomes for corresponding treatment plans (*i.e.,* OORT and DORT) for each patient (p_i), treatment modality (m_j), and risk model (rm_k). We calculated $RFOM$ according to,

$$RFOM(p_i, m_j, rm_k) = \frac{FOM_{\mathrm{OORT}}(p_i, m_j, rm_k)}{FOM_{\mathrm{DORT}}(p_i, m_j)} \tag{5.7}$$

where $FOM_{\mathrm{OORT}}(p_i, m_j, rm_k)$ and $FOM_{\mathrm{DORT}}(p_i, m_j)$ are the FOM's calculated for OORT and DORT treatment plans, respectively, for patient p_i, modality m_j, and risk model rm_k. Thus, $RFOM(p_i, m_j, rm_k) > 1$ indicates that OORT has the superior projected longitudinal outcome compared to DORT and $RFOM(p_i, m_j, rm_k) < 1$ indicates that DORT has the superior

projected longitudinal outcome compared to OORT. Figure 5.2 contains a flow chart depicting the treatment-planning, optimization, and treatment-plan-evaluation methods described up to this point.

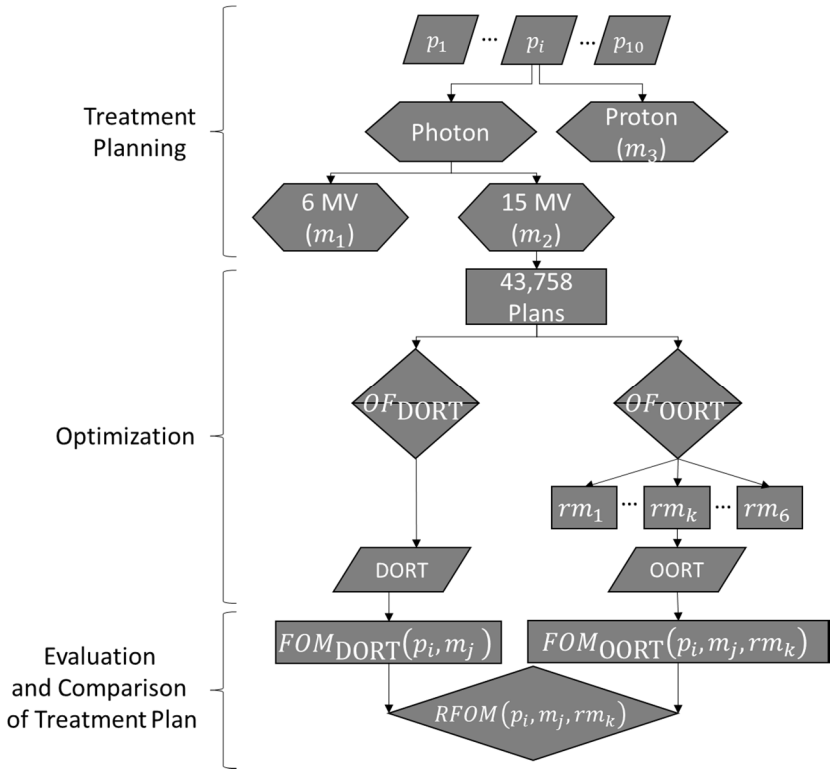

Figure 5.2. Flow chart of the treatment-planning, optimization, and evaluation-and-comparison methods. p_i refers to patient numbers 1 through 10, m_j refers to the three treatment modalities (*i.e.*, 6-MV photons, 15-MV photons, and protons), and rm_k refers to the six dose-response models used to project the risk of radiogenic-cancer incidence (see Figure 5.1).

We performed two statistical tests of significance in the differences between projected longitudinal outcomes after OORT and DORT. Specifically, we tested for values of $RFOM$ that were statistically significantly different than 1 in the sample of patients. First, we assessed whether the majority of OORT treatment plans had projected longitudinal outcomes superior to those of DORT treatment plans (*i.e.,* inclusive of all patients, treatment modalities, and risk models). To do this, we performed a one-sided sign test at the 95% significance level. The sign test is a non-parametric test for the location of the sample median ($\widetilde{RFOM}$) that does not require

any assumptions about the shape of the underlying distribution. Second, we assessed whether the OORT treatment plan for each patient had a superior projected longitudinal outcome compared to the DORT treatment plan for that patient. For this test, we rigorously propagated the 2-σ uncertainties in $RFOM$ following the methods of Homann *et al.*[164] for all patients and treatment modalities using treatment plans optimized using the LNT late-risk model. We then used these uncertainties to perform a one-sided z-test for each patient, p_i, and for each modality, m_j. Table 5.3 contains the details pertaining to each of these statistical tests.

Table 5.3. Statistical tests performed. Details include the name of the test, the null hypothesis (H_0), the alternate or test hypothesis (H_A), and the significance level (α).

Test	H_0	H_A	α
Sign Test	$\widetilde{RFOM}\forall\{p_i, m_j, rm_k\} \leq 1$	$\widetilde{RFOM}\forall\{p_i, m_j, rm_k\} > 1$	0.05
Z Test	$\overline{RFOM(p_\iota, m_\jmath, rm_{\mathrm{LNT}})} \leq 1$	$\overline{RFOM(p_\iota, m_\jmath, rm_{\mathrm{LNT}})} > 1$	0.05
Friedman Test 1	$\widetilde{RFOM}(m_j) = \widetilde{RFOM}(m_{j+1})\forall\{m_j\}$	≥ 1 $\widetilde{RFOM}$ differs	0.05
Friedman Test 2	$\widetilde{RFOM}(rm_k) = \widetilde{RFOM}(rm_{k+1})\forall\{rm_k\}$	≥ 1 $\widetilde{RFOM}$ differs	0.05
Friedman Test 3	$\widetilde{RFOM}(p_i) = \widetilde{RFOM}(p_{i+1})\forall\{p_i\}$	≥ 1 $\widetilde{RFOM}$ differs	0.05

Finally, we performed three sensitivity tests to determine whether the quantitative results were influenced by a series of factors: treatment factors (*e.g.*, the selection of treatment modality), risk-projection factors (*e.g.,* the late-risk model selection), and host factors (*e.g.,* age, anatomical variation such as target volume and organ-at-risk location). We achieved this by performing a Friedman test for each influence factor. The Friedman test is a non-parametric test to determine whether there is a significant difference between the medians of more than 2 populations. Table 5.3 lists the parameters relevant to performing these tests.

5.3. Results

Our optimizations of relative-fluence-weight combinations resulted in 180 OORT treatment plans, 81 of which were unique fluence-weight combinations. These combinations tended to be unique to the treatment-modality selection and patient (*i.e.,* repeated combinations were largely

for the same treatment modality and patient but multiple different late-risk models). 6-MV Photon OORT plans consisted of the largest number of beams (*i.e.,* 11 on average) while proton OORT plans comprised the fewest number of beams (*i.e.,* six on average). Our optimizations resulted in 30 DORT treatment plans, all of which were unique combinations of fluence weights. DORT treatment plans tended to comprise a greater number of beams than OORT (*i.e.,* 12 for 6- and 15-MV photon DORT and eight for proton DORT, on average). Only in one case were the OORT and DORT treatment plans identical (*i.e.,* patient number six, 6-MV photons, OORT using all late-risk models except LNT). Figure 5.3 shows a representative example of the dose distributions from each unique treatment plan for one patient and one treatment modality. These data show that while the DORT plan distributed dose roughly evenly around the patient, OORT treatment plans were characterized by heavily weighted lateral beams and other lower-weighted beam angles.

5.3.1. Tests for Improved Projected Outcomes

Figure 5.4 shows a violin plot of the $RFOM$ (see Eq. 5.7) distribution, inclusive of all patients, treatment modalities, and late-risk models. This plot reveals that the majority of the $RFOM$ probability distribution resides in the region corresponding to a superior projected outcome from OORT treatment plans compared to DORT treatment plans. Indeed, the sign test for the magnitude of the median $RFOM$ compared to 1 resulted in a p-value < 0.05 and thus we rejected the null hypothesis (see Table 5.3). This result suggests that the majority of OORT treatment plans did lead to superior projected long-term health outcomes compared to their corresponding DORT treatment plans.

Figure 5.5 shows the $RFOM$ for the subset of OORT treatment plans optimized using the LNT late-risk model for each patient and each treatment modality. Error bars represent the 95%

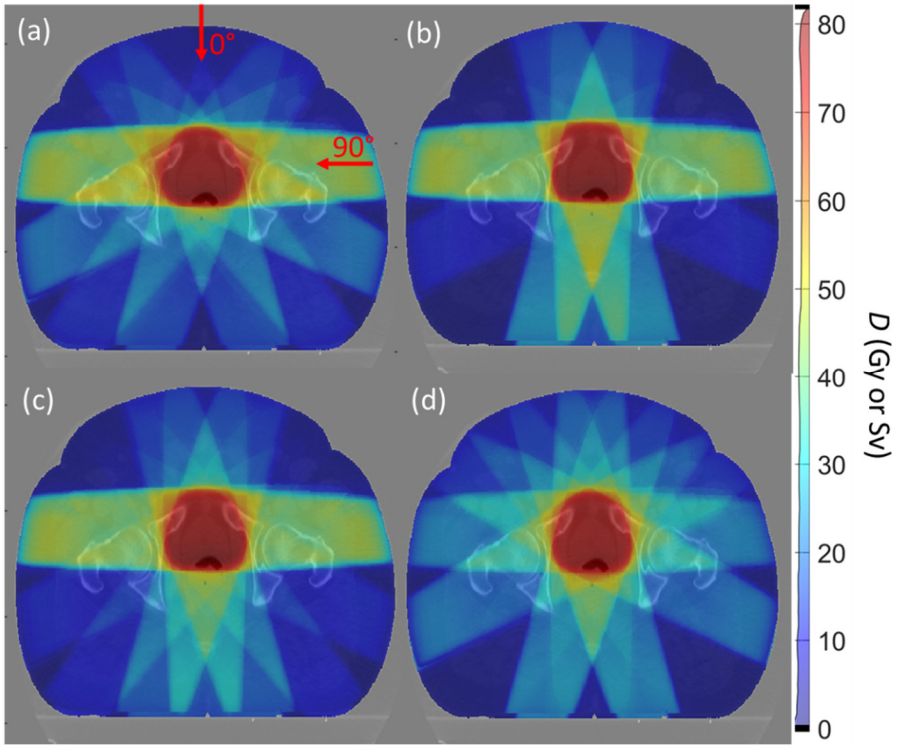

Figure 5.3. Representative example of unique treatment plans for one patient and one treatment modality. Absorbed dose is pictured as a color wash overlaid onto the isocentric slice of the patient computed tomography (CT) for (a) OORT based on late-risk calculated by the LNT model, (b) OORT based on the L-Exp10 late-risk model, (c) OORT based on L-Exp40, L-Plat10, and L-Plat40, and mechanistic late-risk models, and (d) DORT. Examples are shown for the 15-MV photon treatment plans for patient number five and are representative.

confidence intervals in $RFOM$ values. This plot shows that all OORT treatment plans were generally superior. More precisely, all OORT treatment plans except one (at 15 MV for patient number three) had $RFOM$ magnitudes larger than one. Z-tests for all modalities and patients except one resulted in a p-value < 0.05. These results suggest that the OORT methods led to treatment plans with superior projected longitudinal health outcomes compared to DORT at the 95% confidence level for every patient and every treatment modality except for the 15-MV photon treatment plan for patient number three (p = 0.1). It is important to note that the low $RFOM$ for patient number three was a result of an unusually high value of FOM_{DORT} rather than

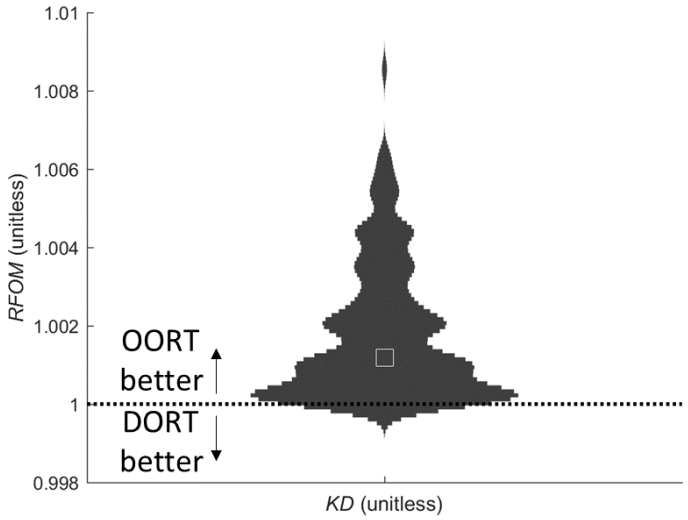

Figure 5.4. Violin plot of the $RFOM$ for all patients, treatment modalities, and risk-model selections. Plot of the ratio of OORT and DORT FOM's ($RFOM$, see Eq. 5.7) versus the kernel density (KD) where KD describes the likelihood of a given $RFOM$ magnitude. The white box indicates the median $RFOM$ ($\widetilde{RFOM}$). The horizontal dashed line represents an $RFOM$ magnitude of 1 where all points above this line indicate that OORT plans had a superior projected outcome compared to DORT plans and points below this line indicate that DORT plans had a superior projected outcome compared to OORT plans.

a particularly low value of FOM_{OORT}. The most-likely explanation for this is that patient number three had a larger separation between his PTV and all of his OARs than average in the population, thus simplifying the optimization problem and enabling both OF_{DORT} and OF_{OORT} to find favorable fluence-weight combinations.

Figure 5.6 shows violin plots of the $RFOM$ distributions for treatment plans grouped by treatment modality, late-risk model, and patient. These plots reveal that the majority of all probability distributions are > 1. This suggests that, qualitatively, the superior projected outcome of OORT treatment plans was generalizable across all influence factors (*i.e.,* treatment modality, late-risk model, and host characteristics). This figure also reveals, however, that there was variation in the $\widetilde{RFOM}$ for distributions grouped by treatment modality and patient, but not for those grouped by late-risk model. The Friedman tests resulted in p-values < 0.05 for plots a and c

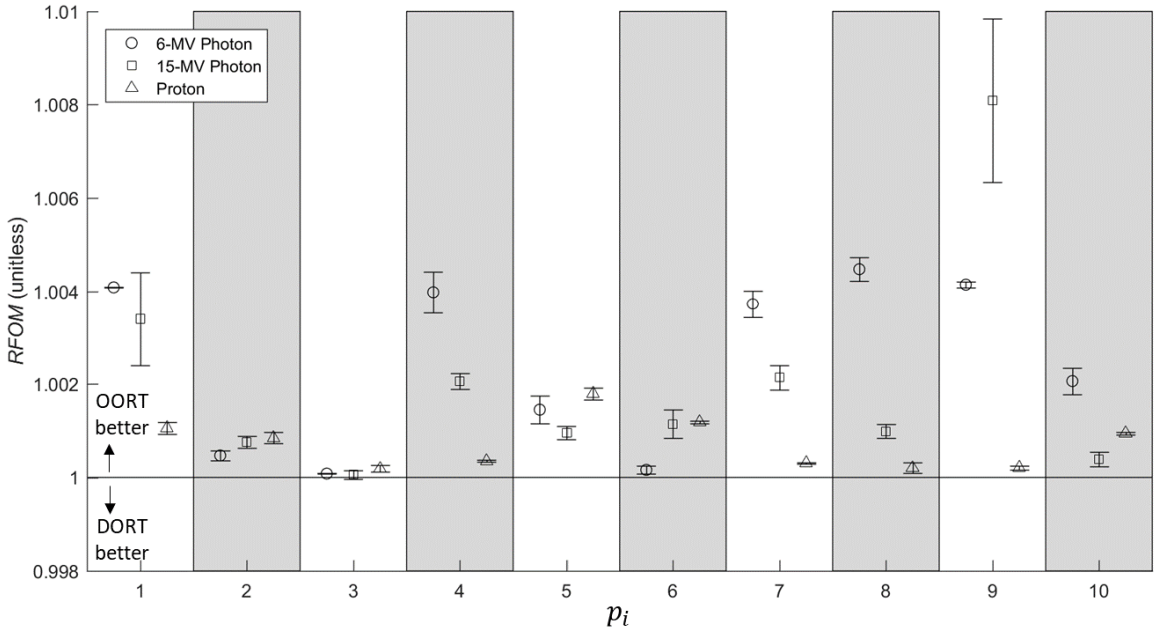

Figure 5.5. Scatter plot of results for treatment plans based on the LNT late-risk model. Ratio of OORT to DORT FOM's ($RFOM$, see Eq. 5.7) versus patient number (p_i). Error bars represent the 95% confidence intervals in the $RFOM$ values based on standard error-propagation methods. The solid horizontal line represents an $RFOM$ magnitude of 1 where points above this line indicate that OORT treatment plans had superior projected outcomes compared to DORT treatment plans and points below this line indicate that DORT plans had projected outcomes superior to those of OORT treatment plans.

and thus we rejected the null hypothesis that all $\widetilde{RFOM}$'s were equivalent (see Table 5.3). This indicates that the quantitative results were influenced, as expected, by the selection of treatment modality and by host factors. The Friedman test for the $\widetilde{RFOM}$ grouped by late-risk model indicated that we could not reject the null hypothesis ($p \gg 0.05$), suggesting that the selection of late-risk model did not influence the optimization results.

5.4. Discussion

In this study, we developed a generally applicable method to directly optimize projected longitudinal health outcomes. We demonstrated this new method by optimizing the relative fluence weight of photon and proton radiotherapy beams in a sample of prostate-cancer patients

in an entirely new and different way, *i.e.,* to improve the projected longitudinal health outcome rather than to meet physical constraints on the dose distribution in the patient. The major finding of this work is that it does appear feasible to directly optimize radiotherapy treatment plans based on the longitudinal (*i.e.*, long- and short-term) health outcomes associated with the therapeutic and stray radiation exposures in individual patients. The specific results of this study suggest that doing so is superior to optimizations aiming to meet dose-volume constraints as evidenced by the rejection of the null hypothesis in both population-based and individual statistical tests.

This study provides a simple and complete framework for optimizing radiotherapy treatment plans directly on the basis of the clinical goals in consideration of all outcomes (*i.e.,* beneficial and detrimental, long- and short-term, fatal and non-fatal) associated with the total dose (*i.e.*, therapeutic and stray) deposited in all of the tissues (*i.e.,* diseased and healthy) in individual patients, the implications of which could be broad. This framework has the potential to increase personalization in radiotherapy treatment planning, whereby dosimetric-constraint driven optimizations are superseded by the direct optimization of projected patient-specific health outcomes. The discrete nature of scalar dosimetric constraints comprise a form of incomplete information (on the dose response) for the optimization algorithm. The missing information precludes the optimization algorithms from finding the best plan. Furthermore, the dosimetric constraints are not necessarily representative of the patient outcome[19]. In this study, the best projected health outcomes were obtained by optimizing the projected health outcome directly. Specifically, we were able to decrease the cumulative risk of long- and short-term detrimental endpoints by an average of 3% and increase the tumor control probability by an average of 1% compared to conventional dose-optimization methods. We estimate that this corresponds to adding up to 7 additional healthy months to the patient's lifetime compared to that expected from

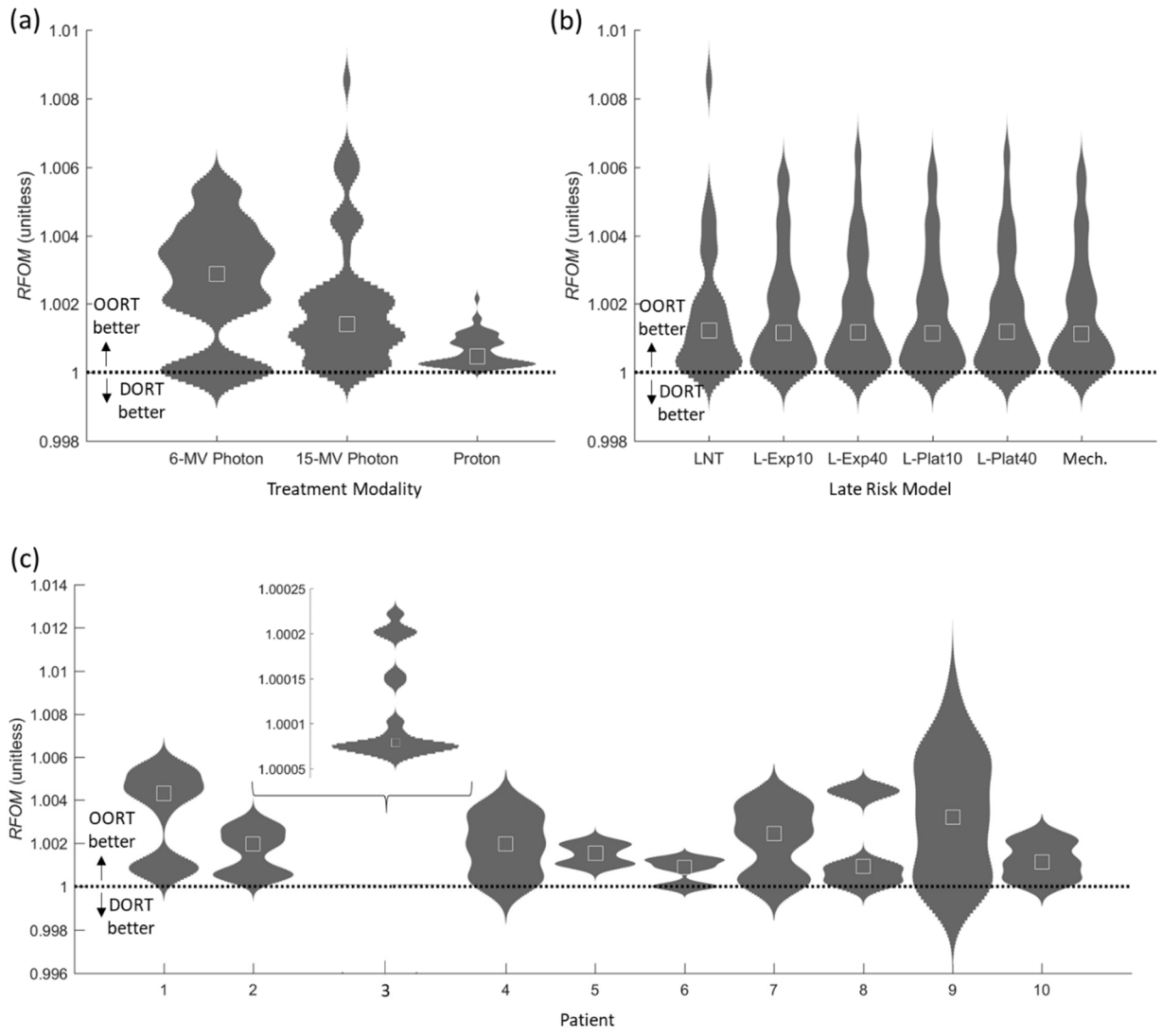

Figure 5.6. Violin plots of three influence factors. Plots of the ratio of OORT and DORT FOM's ($RFOM$, see Eq. 5.7) grouped by (a) treatment modality, (b) late-risk model, and (c) patient number versus the kernel density (KD). KD represents the likelihood of a given $RFOM$ magnitude. The white boxes indicate the median $RFOM$ ($\widetilde{RFOM}$) and the horizontal dashed lines separate $RFOM$ magnitudes indicating that OORT treatment plans had projected longitudinal outcomes superior to those of DORT treatment plans (*i.e.*, those > 1) from $RFOM$ magnitudes indicating that DORT treatment plans had projected outcomes superior to OORT treatment plans (*i.e.*, those < 1). The inlay in panel (c) shows the probability distribution for patient number three in greater detail.

dose-optimized treatment plans. The results of this study also indicated that the methods were generalizable across three treatment modalities, six models for late risk, and ten unique combinations of host factors (*e.g.,* age, tumor size, organ-at-risk location and size). Although, the

degree of improvement varied with the selection of treatment modality and the unique combination of patient-specific parameters.

The results of this study are in agreement with previous studies in the literature. In the most directly comparable study, Modiri *et al.*[31] optimized the relative fluence weight for photon-therapy treatments of one breast and one Hodgkin lymphoma case by minimizing the total risk of tumor recurrence and mortality from radiation-related late effects. Their outcome optimizations resulted in a total decrease in risk of detrimental effects of less than 2% for the breast case and 6% for the Hodgkin lymphoma case. Our average decrease in cumulative risk of 3% is in agreement with their results. In another related study, Rechner *et al.*[29] optimized beam angle and relative fluence weight for one prostate-cancer patient receiving proton therapy by minimizing the risk of second cancer in the rectum and bladder. They were able to reduce the excess relative risk of second cancer in the rectum and bladder by 30% and 21%, respectively. This is similar to the results of our longitudinally optimized outcomes, which reduced the excess relative risk of second cancer in the rectum and bladder by an average of 23% and 21%, respectively.

This study has several notable strengths. First, we minimized methodological bias by utilizing a recently developed research TPS capable of calculating the total absorbed dose from both therapeutic and stray radiation exposures, the latter of which is usually neglected. This enabled us to optimize complete projections of the long- and short-term effects in each individual patient. Additionally, we used a new framework for combining arbitrary numbers and types of beneficial and detrimental health effects of planned radiation exposures to assess the projected outcomes resulting from OORT and DORT treatment plans. This study also explored a wide array of influence factors including charged and uncharged particles, six different late-risk models, and ten patients, each with their own unique combination of host factors like age and anatomical

characteristics, such as target volume and organ-at-risk location. This enabled us to explore the generalizability of our OORT methods across three influence factors. Finally, the exhaustive-search methods employed in this study had two important strengths. First, they reliably found the global minimum in each and every optimization. Gradient-search iterative optimization techniques common in contemporary radiotherapy optimization are known to be limited by the "local minima" problem whereby they are susceptible to getting trapped in a local minimum and missing the true optimal result, the global minimum[162]. Our exhaustive search, however, avoided this limitation. Second, the exhaustive search provided additional information on the parameter space of the optimization. Different iterative optimization techniques are best suited to specific parameter-space characteristics. Prior to this study, the parameter-space characteristics for the new outcome-based objective function were unknown and thus it was not clear which iterative optimization algorithm was best suited to outcome optimizations. Thus, the additional information yielded by the exhaustive search could guide the selection of appropriate optimization algorithms in the future.

This study also had several limitations. First, the outcome-optimization methods presented here rely heavily on the availability of dose-response functions for all tissues and endpoints to be considered, the knowledge of which is still incomplete. The functional form of dose-response functions, however, is well understood for many endpoints and most commonly taken to be sigmoidal or linear, depending on the endpoint. Thus we believe it would be possible to translate the information contained in currently used, discrete, scalar dose objectives into continuous dose-response functions matching a known or assumed functional form (*e.g.,* linear, sigmoidal, linear exponential, linear plateau, *etc.*) for preliminary inclusion in our framework. These models could

easily be modified and updated as radiobiological and epidemiological understanding of the true relationships are refined in the future.

Another limitation is that, due to the conceptually different approach taken here, relatively less is known about how the uncertainty in the dose-response functions (*e.g.,* due to interpatient variations) affects the certainty of the optimization result. This issue may be addressed, however, by performing additional sensitivity tests, such as those performed in this work and by others[29, 31, 51], to assess the sensitivity of the optimization to uncertainties in the dose-response functions. Another limitation related to the conceptually different approach is the question of continuity of care. This is not a serious limitation, however, because it is possible to do both outcome- and dose-based optimizations separately (allowing for training and retrospective evaluations of projected versus actual outcomes) or to combine OF_{OORT} with OF_{DORT} to create a hybrid objective function, OF_{H}, as in

$$OF_{\mathrm{H}} = OF_{\mathrm{OORT}} \times OF_{\mathrm{DORT}} . \qquad 5.8$$

Our preliminary tests revealed that OF_{H} collapses to the hitherto method (*i.e.*, dosimetric optimization using OF_{DORT} alone) thus providing a mechanism to do comparative studies and ensure continuity of care.

Finally, the optimization technique that we utilized (*i.e.,* the exhaustive search) was not representative of standard-of-care methods in most clinical settings (*i.e.,* iterative gradient-search optimization techniques). Our preliminary studies suggest, however, that OF_{OORT} should work to replace OF_{DORT} to guide an iterative optimization algorithm. In fact, OF_{OORT} decreased the number of local minima in the parameter space by nearly 4% compared to OF_{DORT}. This suggests that OF_{OORT} appears to be less susceptible to the local minima problem than standard-of-care

methods. Additionally, OF_{OORT} increased the slope of the gradient (assessed over the 1000 top-ranked values) by 44% compared to OF_{DORT}. These findings suggest that OF_{OORT} is compatible with clinical optimization algorithms and could computationally simplify the optimization problem.

5.5. Conclusion

The results of this study provide promising evidence that it may be possible to improve the projected longitudinal health outcomes of radiotherapy patients by directly optimizing the projected health outcomes themselves (*i.e.,* by replacing discrete, dose-based objectives and penalties with continuous, long- and short-term dose-response functions). The methods developed in this work are generalizable and may consider arbitrary numbers and types of endpoints. Thus, they enable all important aspects of cancer survivorship to be taken into account and provide a more direct approach to realizing the full beneficial potential of cancer radiotherapy.

Chapter 6. Discussion and Conclusions

This work, for the first time, tested the end-to-end feasibility of directly optimizing outcomes considering beneficial and detrimental, long- and short-term, and fatal and non-fatal effects associated with all of the radiation exposures in all of the tissues of individuals, groups, and populations. This necessitated the development and testing of several tools to calculate the dose from both therapeutic and stray exposures in individuals, evaluate the dose across the wide dynamic range of magnitudes, combine the risks of varying types and severity, and directly optimize the outcomes. The major finding is that it is feasible to directly optimize the biological goal, the projected health outcome, of planned radiation exposures (*e.g.*, industrial, diagnostic, or therapeutic) in a personalized manner. Furthermore, these methods do not necessitate a complete abandonment of current guidelines and limits, thus providing backwards compatibility with current standards of practice.

6.1. Implications

The specific results of this study suggest that there is an opportunity to improve health outcomes by algorithmically and directly optimizing the outcomes themselves, rather than indirectly optimizing dose distributions via scalar dosimetric constraints that are poor surrogates for the health outcome[19]. With the new methods developed here, it is now possible to consider all of the benefits and detriments for which there exists any information on the dose response. For example, in the field of radiotherapy, recent research in the fields of medical physics, radiation biology, and epidemiology have rapidly expanded the knowledge of the potential beneficial and detrimental health effects and their relationships with dose[121, 150]. This deluge of information now necessitates a framework to algorithmically consider arbitrary numbers of opposing forces in a personalized manner. Thus, we find ourselves at an auspicious time when a framework that is

capable of utilizing all of the available information could bring the realization of the full beneficial potential of radiotherapy within reach. The tools developed in this work could be implemented, for example, to enhance radiotherapy treatment-planning methods (Chapter 5). These new methods, however, are not limited to radiotherapy. They could also be applied to other medical and non-medical applications as computer-aided decision tools (Chapter 4).

6.2. Coherence with Existing Literature

Due to the fact that previous works in this area took relatively fewer of the potential health effects into account, it is difficult to draw direct quantitative comparisons. Rechner *et al.*[29] optimized proton radiotherapy treatment plans for a prostate radiotherapy patient by minimizing the cumulative risk of second cancer in the rectum and bladder. Our results are in agreement with those of Rechner *et al.* in that both studies revealed an opportunity to reduce the cumulative risk to the patient while maintaining or improving the projected benefits by directly optimizing the continuous dose-response functions. Furthermore, Rechner explored the influence of risk-model selection on the optimization result by repeating their optimizations for six different late-risk models. They found that this resulted in three unique treatment plans for one patient, depending on the selection of risk model. We also explored the effects of six late-risk models on our optimization results and found that on average, these risk models resulted in three unique plans for each patient. Qualitatively, our results are in agreement with those of Homann *et al.*[164] who showed the importance of a personalized approach to radiotherapy treatment planning in a population of female Hodgkin-lymphoma patients. In our study of male prostate-cancer patients, the largest quantitative variations were due to inter-patient variation in host factors, such as age and anatomical characteristics (*e.g.,* tumor volume, organ-at-risk volume and location). This points towards a theoretical advantage to optimizing treatment plans in a personalized manner

for each and every patient. Our findings for prostate radiotherapy differ from those of prior studies of pediatric medulloblastoma patients receiving craniospinal irradiation, which showed a class solution (*i.e.*, little or no need for personalized optimization)[15, 165]. In the most directly comparable study, Modiri *et al.*[31] optimized the beam angle and relative fluence weight for two patients by minimizing the cumulative risk of early and late health effects. Although they neglected the stray radiation exposures, Modiri *et al.* found that such methods could reduce the cumulative risk by between 1% and 6%. This quantitatively agrees with our results, which reduced the cumulative risk of early and late effects by an average of 3%.

6.3. Strengths of the Study

This study had several notable strengths. First, we specifically designed our framework to be generalizable; scalable to arbitrary health effects, tissues, and organs; and broadly applicable. In fact, we demonstrated these methods in the field of cancer radiotherapy, diagnostic imaging, and emergency response. The comprehensive and algorithmic approach developed in this work was also a strength in that it decreased subjectivity and concomitant requirements for user skill. Furthermore, the exhaustive-search optimization methods implemented here also decreased requirements for user skill as no initial guess was required or made. Thus, the methods were not susceptible to erroneous results due to a poor choice of initial guess. Another major strength is that the tools developed here are conceptually transparent (*i.e.*, simple and intuitive). This is especially important for clinicians and others who are responsible for ensuring that any decisions are ethical and therefore in keeping with an individual's wishes (*i.e.,* autonomy) and well-being (*i.e.,* beneficence). Finally, we performed an analysis of uncertainty, thus ensuring the comprehensive consideration of the significance of our findings and proper interpretation of the results.

6.4. Limitations of the Study

This study was not free from features that might be viewed as limitations. First, we only tested the practical application of our new methods to one cancer treatment site, the prostate. This was not a significant limitation because with this one site, we explored 3 different treatment modalities, 10 patients, and 1.3 million treatment plans. Thus, while future studies are needed to confirm the findings at different treatment sites, our findings illustrate the capabilities and potential of this approach. Additionally, we only simulated conventional radiotherapy and did not explore the applicability to more advanced treatment deliveries, such as intensity modulated radiotherapy (IMRT) or volumetric arc therapy (VMAT), for which exhaustive-search methods may not be feasible. Treatment planning for these delivery techniques typically involves gradient-search iterative optimization methods. This was not considered a serious limitation, however, because our framework should work with gradient-search optimization algorithms. In fact, when compared to the objective function commonly used to guide these algorithms, our outcome-based objective function decreased the number of local minima and increased the gradient near the global minimum. This suggests that our new figure of merit could computationally simplify the iterative optimization problem. Finally, the entirety of this study was performed *in silico* rather than *in vivo*. This, however, is common and indeed necessary. The long follow-up times that would be required to observe late effects, which have latencies on the order or years or decades, combined with rapidly evolving technology would render the results of an *in vivo* study obsolete by the time adequate follow-up data were acquired.

6.5. Conclusion

This work demonstrated that it is, in fact, possible to combine all of the potential effects (*i.e.,* beneficial and detrimental, long-term and short-term, fatal and non-fatal) of a medical

intervention, thereby enabling the improvement of longitudinal health outcome as opposed to the treatment benefits alone. Our example in cancer radiotherapy revealed the opportunity to improve the probability of treatment benefit by an average of 1%, while simultaneously decreasing the cumulative probability of long- and short-term treatment side effects by an average of 3% compared to contemporary treatment-planning techniques. An algorithmic approach such as that developed in this work will become necessary to improve outcomes for many patients with serious illnesses and who face treatment side effects. In conclusion, this work, taken together, provides an objective and comprehensive methodological framework that could enable a paradigm shift towards more objective and automated approaches to improving patient outcomes.

Appendix A. Copyright Information

This Agreement between Louisiana State University -- Lydia Wilson ("You") and John Wiley and Sons ("John Wiley and Sons") consists of your license details and the terms and conditions provided by John Wiley and Sons and Copyright Clearance Center.

License Number	4535970071636
License date	Feb 25, 2019
Licensed Content Publisher	John Wiley and Sons
Licensed Content Publication	Medical Physics
Licensed Content Title	An objective method to evaluate radiation dose distributions varying by three orders of magnitude
Licensed Content Author	Lydia J. Wilson, Wayne D. Newhauser, Christopher W. Schneider
Licensed Content Date	Feb 23, 2019
Licensed Content Volume	0
Licensed Content Issue	0
Licensed Content Pages	8
Type of use	Dissertation/Thesis
Requestor type	Author of this Wiley article
Format	Electronic
Portion	Full article
Will you be translating?	No
Title of your thesis / dissertation	Generally Applicable Framework for Algorithmically Optimizing Longitudinal Health Outcomes of Medical Interventions: An Example in Cancer Radiotherapy
Expected completion date	Apr 2019
Expected size (number of pages)	120
Requestor Location	Louisiana State University Department of Physics and Astronomy 202 Nicholson Hall BATON ROUGE, LA 70810 United States Attn: Louisiana State University
Publisher Tax ID	EU826007151

Appendix B. Additional Generalized Gamma Index Equations

The generalized gamma index can be calculated for 2- and 3-dimensional analyses by the following equations:

2-Dimensional Analysis:

$$\Gamma_{\mathrm{G}}(x_{\mathrm{m}}, y_{\mathrm{m}}, x_{\mathrm{c}}, y_{\mathrm{c}}) = \begin{cases} \sqrt{\dfrac{r^2(x_{\mathrm{m}}, y_{\mathrm{m}}, x_{\mathrm{c}}, y_{\mathrm{c}})}{\Delta d^2} + \dfrac{{\delta_R}^2(x_{\mathrm{m}}, y_{\mathrm{m}}, x_{\mathrm{c}}, y_{\mathrm{c}})}{\Delta {D_{\mathrm{R}}}^2}}, & \text{for } x_{\mathrm{m}}, y_{\mathrm{m}} \text{ at therapeutic locations} \\ \sqrt{\dfrac{r^2(x_{\mathrm{m}}, y_{\mathrm{m}}, x_{\mathrm{c}}, y_{\mathrm{c}})}{\Delta d^2} + \dfrac{{\delta_A}^2(x_{\mathrm{m}}, y_{\mathrm{m}}, x_{\mathrm{c}}, y_{\mathrm{c}})}{\Delta {D_{\mathrm{A}}}^2}}, & \text{for } x_{\mathrm{m}}, y_{\mathrm{m}} \text{ at out-of-field locations} \end{cases} \quad \text{B.1}$$

$$r(x_{\mathrm{m}}, y_{\mathrm{m}}, x_{\mathrm{c}}, y_{\mathrm{c}}) = \sqrt{(x_{\mathrm{m}} - x_{\mathrm{c}})^2 + (y_{\mathrm{m}} - y_{\mathrm{c}})^2} \forall \{x_{\mathrm{m}}, y_{\mathrm{m}}, x_{\mathrm{c}}, y_{\mathrm{c}}\} \quad \text{B.2}$$

$$\delta_{\mathrm{R}}(x_{\mathrm{m}}, y_{\mathrm{m}}, x_{\mathrm{c}}, y_{\mathrm{c}}) = \frac{D_{\mathrm{c}}(x_{\mathrm{c}}, y_{\mathrm{c}}) - D_{\mathrm{m}}(x_{\mathrm{m}}, y_{\mathrm{m}})}{D_{\mathrm{Rx}}} \quad \text{B.3}$$

$$\delta_{\mathrm{A}}(x_{\mathrm{m}}, y_{\mathrm{m}}, x_{\mathrm{c}}, y_{\mathrm{c}}) = D_{\mathrm{c}}(x_{\mathrm{c}}, y_{\mathrm{c}}) - D_{\mathrm{m}}(x_{\mathrm{m}}, y_{\mathrm{m}}) \quad \text{B.4}$$

$$\gamma_{\mathrm{G}}(x_{\mathrm{m}}, y_{\mathrm{m}}) = \min\{\Gamma_{\mathrm{G}}(x_{\mathrm{m}}, y_{\mathrm{m}}, x_{\mathrm{c}}, y_{\mathrm{c}})\} \forall \{x_{\mathrm{c}}, y_{\mathrm{c}}\} \quad \text{B.5}$$

3-Dimensional Analysis:

$$\Gamma_{\mathrm{G}}(x_{\mathrm{m}}, y_{\mathrm{m}}, z_{\mathrm{m}}, x_{\mathrm{c}}, y_{\mathrm{c}}, z_{\mathrm{c}}) = \begin{cases} \sqrt{\dfrac{r^2(x_{\mathrm{m}}, y_{\mathrm{m}}, z_{\mathrm{m}}, x_{\mathrm{c}}, y_{\mathrm{c}}, z_{\mathrm{c}})}{\Delta d^2} + \dfrac{{\delta_R}^2(x_{\mathrm{m}}, y_{\mathrm{m}}, z_{\mathrm{m}}, x_{\mathrm{c}}, y_{\mathrm{c}}, z_{\mathrm{c}})}{\Delta {D_{\mathrm{R}}}^2}}, & \text{for } x_{\mathrm{m}}, y_{\mathrm{m}}, z_{\mathrm{m}} \text{ at therapeutic locations} \\ \sqrt{\dfrac{r^2(x_{\mathrm{m}}, y_{\mathrm{m}}, z_{\mathrm{m}}, x_{\mathrm{c}}, y_{\mathrm{c}}, z_{\mathrm{c}})}{\Delta d^2} + \dfrac{{\delta_A}^2(x_{\mathrm{m}}, y_{\mathrm{m}}, z_{\mathrm{m}}, x_{\mathrm{c}}, y_{\mathrm{c}}, z_{\mathrm{c}})}{\Delta {D_{\mathrm{A}}}^2}}, & \text{for } x_{\mathrm{m}}, y_{\mathrm{m}}, z_{\mathrm{m}} \text{ at out-of-field locations} \end{cases} \quad \text{B.6}$$

$$r(x_{\mathrm{m}}, y_{\mathrm{m}}, z_{\mathrm{m}}, x_{\mathrm{c}}, y_{\mathrm{c}}, z_{\mathrm{c}}) = \sqrt{(x_{\mathrm{m}} - x_{\mathrm{c}})^2 + (y_{\mathrm{m}} - y_{\mathrm{c}})^2 + (z_{\mathrm{m}} - z_{\mathrm{c}})^2} \forall \{x_{\mathrm{m}}, y_{\mathrm{m}}, z_{\mathrm{m}}, x_{\mathrm{c}}, y_{\mathrm{c}}, z_{\mathrm{c}}\} \quad \text{B.7}$$

$$\delta_{\mathrm{R}}(x_{\mathrm{m}}, y_{\mathrm{m}}, z_{\mathrm{m}}, x_{\mathrm{c}}, y_{\mathrm{c}}, z_{\mathrm{c}}) = \frac{D_{\mathrm{c}}(x_{\mathrm{c}}, y_{\mathrm{c}}, z_{\mathrm{c}}) - D_{\mathrm{m}}(x_{\mathrm{m}}, y_{\mathrm{m}}, z_{\mathrm{m}})}{D_{\mathrm{Rx}}} \quad \text{B.8}$$

$$\delta_{\mathrm{A}}(x_{\mathrm{m}}, y_{\mathrm{m}}, z_{\mathrm{m}}, x_{\mathrm{c}}, y_{\mathrm{c}}, z_{\mathrm{c}}) = D_{\mathrm{c}}(x_{\mathrm{c}}, y_{\mathrm{c}}, z_{\mathrm{c}}) - D_{\mathrm{m}}(x_{\mathrm{m}}, y_{\mathrm{m}}, z_{\mathrm{m}}) \quad \text{B.9}$$

$$\gamma_{\mathrm{G}}(x_{\mathrm{m}}, y_{\mathrm{m}}, z_{\mathrm{m}}) = \min\{\Gamma_{\mathrm{G}}(x_{\mathrm{m}}, y_{\mathrm{m}}, z_{\mathrm{m}}, x_{\mathrm{c}}, y_{\mathrm{c}}, z_{\mathrm{c}})\}\forall\{x_{\mathrm{c}}, y_{\mathrm{c}}, z_{\mathrm{c}}\} \quad \text{B.10}$$

Works Cited

[1] R. Gillon, "Medical ethics: four principles plus attention to scope," BMJ (Clinical research ed.) **309**, 184-188 (1994).

[2] L.L. Lipscombe, J.E. Hux, "Trends in diabetes prevalence, incidence, and mortality in Ontario, Canada 1995–2005: a population-based study," The Lancet **369**, 750-756 (2007).

[3] H. Weir, R. Anderosn, S. Coleman King, A. Soman, T. Thomspson, Y. Hong, "Heart Disease and Cancer Deaths - Trends and Projections in the United States, 1969-2020," Prev. Chronic Dis. **13**, 160211 (2016).

[4] N. Howlader, A. Noone, M. Krapcho, D. Miller, K. Bishop, C. Kosary, M. Yu, J. Ruhl, Z. Tatalovich, A. Mariotto, D. Lewis, H. Chen, E. Feuer, *SEER Cancer Statistics Review, 1975-2014*. (National Cancer Institute, Bethesda, MD, 2017).

[5] S. Vijan, J.B. Sussman, J.S. Yudkin, R.A. Hayward, "Effect of Patients' Risks and Preferences on Health Gains With Plasma Glucose Level Lowering in Type 2 Diabetes Mellitus," JAMA Internal Medicine **174**, 1227-1234 (2014).

[6] P.A. McCullough, R. Wolyn, L.L. Rocher, R.N. Levin, W.W. O'Neill, "Acute Renal Failure After Coronary Intervention: Incidence, Risk Factors, and Relationship to Mortality," The American Journal of Medicine **103**, 368-375 (1997).

[7] G.T. Armstrong, T. Kawashima, W. Leisenring, K. Stratton, M. Stovall, M.M. Hudson, C.A. Sklar, L.L. Robison, K.C. Oeffinger, "Aging and Risk of Severe, Disabling, Life-Threatening, and Fatal Events in the Childhood Cancer Survivor Study," J. Clin. Oncol. **32**, 1218-1227 (2014).

[8] ACS, *Global Cancer Facts & Figures 4th Edition*. (Atlanta, 2018).

[9] N. Howlader, A. Noone, M. Krapcho, J. Garshell, D. Miller, S. Altekruse, C. Kosary, M. Yu, J. Ruhl, Z. Tatalovich, A. Mariotto, D. Lewis, H. Chen, E. Feuer, K. Cronin, *SEER Cancer Statistics Review, 1975-2012*. (National Cancer Institute, Bethesda, MD, 2014).

[10] ACS, *Cancer Treatment & Survivorship Facts & Figures 2016-2017*. (Atlanta, 2016).

[11] D.R. Smart, *Physician Characteristics and Distribution in the US 2010*. (American Medical Association, 2009).

[12] R.H. Mak, D. Hunt, J.A. Efstathiou, N.M. Heney, C.U. Jones, H.R. Lukka, J.-P. Bahary, M. Patel, A. Balogh, A. Nabid, M.H. Leibenhaut, D.A. Hamstra, K.S. Roof, R.J. Lee, E.M. Gore, H.M. Sandler, W.U. Shipley, "Acute and Late Urinary Toxicity following Radiation in Men With an Intact Prostate Gland or after a Radical Prostatectomy: A Secondary Analysis of RTOG 94-08 and 96-01," Urol. Oncol. **34**, 430.e431-430.e437 (2016).

[13] L. Claude, D. Pérol, C. Ginestet, L. Falchero, D. Arpin, M. Vincent, I. Martel, S. Hominal, J.-F. Cordier, C. Carrie, "A prospective study on radiation pneumonitis following conformal radiation therapy in non-small-cell lung cancer: clinical and dosimetric factors analysis," Radiotherapy and Oncology **71**, 175-181 (2004).

[14] S.P. Elliott, S.L. Jarosek, S.R. Alanee, B.R. Konety, K.E. Dusenbery, B.A. Virnig, "3-DIMENSIONAL EXTERNAL BEAM RADIOTHERAPY FOR PROSTATE CANCER INCREASES THE RISK OF HIP FRACTURE," Cancer **117**, 4557-4565 (2011).

[15] W.D. Newhauser, J.D. Fontenot, A. Mahajan, D. Kornguth, M. Stovall, Y. Zheng, P.J. Taddei, D. Mirkovic, R. Mohan, J.D. Cox, S. Woo, "The risk of developing a second cancer after receiving craniospinal proton irradiation," Phys. Med. Biol. **54**, 2277-2291 (2009).

[16] R. Zhang, R.M. Howell, K. Homann, A. Giebeler, P.J. Taddei, A. Mahajan, W.D. Newhauser, "Predicted risks of radiogenic cardiac toxicity in two pediatric patients undergoing photon or proton radiotherapy," Radiat. Oncol. **8**, 184 (2013).

[17] A. Perez-Andujar, W.D. Newhauser, P.J. Taddei, A. Mahajan, R.M. Howell, "Predicted relative risk of follicular depletion for three radiotherapy modalities in a girl receiving craniospinal irradiation," Phys. Med. Biol. **58**, 3107 (2013).

[18] J.P. Williams, W. Newhauser, "Normal tissue damage: its importance, history and challenges for the future," Br. J. Radiol., 20180048 (2018).

[19] J.O. Deasy, A. Niemierko, D. Herbert, D. Yan, A. Jackson, R.K. Ten Haken, M. Langer, S. Sapareto, "Methodological issues in radiation dose–volume outcome analyses: Summary of a joint AAPM/NIH workshop," Medical Physics **29**, 2109-2127 (2002).

[20] A. Niemierko, "A generalized concept of equivalent uniform dose (EUD)," Med. Phys. **26**, 1101 (1999).

[21] U. Schneider, D. Zwahlen, D. Ross, B. Kaser-Hotz, "Estimation of radiation-induced cancer from three-dimensional dose distributions: Concept of organ equivalent dose," International Journal of Radiation Oncology*Biology*Physics **61**, 1510-1515 (2005).

[22] J.A. Langendijk, P. Lambin, D. De Ruysscher, J. Widder, M. Bos, M. Verheij, "Selection of patients for radiotherapy with protons aiming at reduction of side effects: The model-based approach," Radiotherapy and Oncology **107**, 267-273 (2013).

[23] P. Kallman, B.K. Lind, A. Brahme, "An algorithm for maximizing the probability of complication-free tumour control in radiation therapy," Physics in Medicine and Biology **37**, 871 (1992).

[24] R. Mohan, G.S. Mageras, B. Baldwin, L.J. Brewster, G.J. Kutcher, S. Leibel, C.M. Burman, C.C. Ling, Z. Fuks, "Clinically relevant optimization of 3-D conformal treatments," Medical Physics **19**, 933-944 (1992).

[25] B.K. Lind, P. Mavroidis, S. Hyodynmaa, C. Kappas, "Optimization of the dose level for a given treatment plan to maximize the complication-free tumor cure," Acta Oncol. **38**, 787-798 (1999).

[26] J.J. Wilkens, U. Oelfke, "Fast multifield optimization of the biological effect in ion therapy," Physics in Medicine and Biology **51**, 3127 (2006).

[27] A.L. Hoffmann, H. Huizenga, J.H. Kaanders, "Employing the therapeutic operating characteristic (TOC) graph for individualised dose prescription," Radiation Oncology **8**, 1-9 (2013).

[28] Y. Sugano, M. Mizuta, S. Takao, H. Shirato, K.L. Sutherland, H. Date, "Optimization of the fractionated irradiation scheme considering physical doses to tumor and organ at risk based on dose–volume histograms," Medical Physics **42**, 6203-6210 (2015).

[29] L.A. Rechner, J.G. Eley, R.M. Howell, R. Zhang, D. Mirkovic, W.D. Newhauser, "Risk-optimized proton therapy to minimize radiogenic second cancers," Phys. Med. Biol. **60**, 3999-4013 (2015).

[30] N.P. Brodin, I.R. Vogelius, T. Bjork-Eriksson, P. Munck Af Rosenschold, M.V. Maraldo, M.C. Aznar, L. Specht, S.M. Bentzen, "Optimizing the radiation therapy dose prescription for pediatric medulloblastoma: minimizing the life years lost attributable to failure to control the disease and late complication risk," Acta Oncol. **53**, 462-470 (2014).

[31] A. Modiri, L.B. Stick, S.R. Rice, L.A. Rechner, I.R. Vogelius, S.M. Bentzen, A. Sawant, "Individualized estimates of overall survival in radiation therapy plan optimization - A concept study," Medical Physics **45**, 5332-5342 (2018).

[32] B. Sánchez-Nieto, M. Romero-Expósito, J.A. Terrón, F. Sánchez-Doblado, "Uncomplicated and Cancer-Free Control Probability (UCFCP): A new integral approach to treatment plan optimization in photon radiation therapy," Physica Medica: European Journal of Medical Physics **42**, 277-284 (2017).

[33] L.J. Wilson, W.D. Newhauser, C.W. Schneider, "An objective method to evaluate radiation dose distributions varying by three orders of magnitude," Medical Physics **46**, 1888-1895 (2019).

[34] L.J. Wilson, W.D. Newhauser, C.W. Schneider, F. Kamp, M. Reiner, J.C. Martins, G. Landry, R.-P. Kapsch, M. Schrader, M. Meier, O. Tappe, K. Parodi, "Method to quickly and accurately calculate absorbed dose from therapeutic and stray photon exposures throughout the entire body in individual patients," Med. Phys.(in preparation)).

[35] L.J. Wilson, W.D. Newhauser, "Justification and optimization of planned exposures: a new framework to aggregate arbitrary detriments and benefits," Radiat. Environ. Biophys.(in preparation)).

[36] L.J. Wilson, W.D. Newhauser, "Generalized approach for radiotherapy treatment planning by optimizing health outcome instead of dose: preliminary results for prostate radiotherapy patients," Phys. Med. Biol.(in preparation)).

[37] ICRU, *Determination of Absorbed Dose in a Patient Irradiated by X or Gamma Rays in Radiotherapy Procedures. Report 24*. (1976).

[38] R.M. Howell, S.B. Scarboro, S.F. Kry, D.Z. Yaldo, "Accuracy of out-of-field dose calculations by a commercial treatment planning system," Phys. Med. Biol. **55**, 6999-7008 (2010).

[39] U. Schneider, R.A. Halg, M. Hartmann, A. Mack, F. Storelli, A. Joosten, R. Mockli, J. Besserer, "Accuracy of out-of-field dose calculation of tomotherapy and cyberknife treatment planning systems: a dosimetric study," Zeitschrift fur medizinische Physik **24**, 211-215 (2014).

[40] L.J. Jagetic, W.D. Newhauser, "A simple and fast physics-based analytical method to calculate therapeutic and stray doses from external beam, megavoltage x-ray therapy," Phys. Med. Biol. **60**, 4753-4775 (2015).

[41] A. Joosten, O. Matzinger, W. Jeanneret-Sozzi, F. Bochud, R. Moeckli, "Evaluation of organ-specific peripheral doses after 2-dimensional, 3-dimensional and hybrid intensity modulated radiation therapy for breast cancer based on Monte Carlo and convolution/superposition algorithms: implications for secondary cancer risk assessment," Radiother Oncol **106**, 33-41 (2013).

[42] B.E. Nelms, J.A. Simon, "A survey on planar IMRT QA analysis," J Appl Clin Med Phys **8**, 2448 (2007).

[43] I. Diallo, N. Haddy, E. Adjadj, A. Samand, E. Quiniou, J. Chavaudra, I. Alziar, N. Perret, S. Guerin, D. Lefkopoulos, F. de Vathaire, "Frequency Distribution of Second Solid Cancer Locations in Relation to the Irradiated Volume among 115 Patients Treated for Childhood Cancer," Int J Radiat Oncol **74**, 876-883 (2009).

[44] R. Zhang, R.M. Howell, P.J. Taddei, A. Giebeler, A. Mahajan, W.D. Newhauser, "A comparative study on the risks of radiogenic second cancers and cardiac mortality in a set of pediatric medulloblastoma patients treated with photon or proton craniospinal irradiation," Radiotherapy and Oncology **113**, 84-88 (2014).

[45] Ž. Knežević, L. Stolarczyk, I. Bessieres, J.M. Bordy, S. Miljanić, P. Olko, "Photon dosimetry methods outside the target volume in radiation therapy: Optically stimulated luminescence (OSL), thermoluminescence (TL) and radiophotoluminescence (RPL) dosimetry," Radiation Measurements **57**, 9-18 (2013).

[46] N. Chofor, D. Harder, K.C. Willborn, B. Poppe, "Internal scatter, the unavoidable major component of the peripheral dose in photon-beam radiotherapy," Phys. Med. Biol. **57**, 1733-1743 (2012).

[47] M.A. Benadjaoud, J. Bezin, A. Veres, D. Lefkopoulos, J. Chavaudra, A. Bridier, F. de Vathaire, I. Diallo, "A multi-plane source model for out-of-field head scatter dose calculations in external beam photon therapy," Phys. Med. Biol. **57**, 7725-7739 (2012).

[48] P.H. Van der Giessen, "A simple and generally applicable method to estimate the peripheral dose in radiation teletherapy with high energy x-rays or gamma radiation," Int J Radiat Oncol Biol Phys **35**, 1059-1068 (1996).

[49] J.V. Bezin, A. Veres, D. Lefkopoulos, J. Chavaudra, E. Deutsch, F. de Vathaire, I. Diallo, "Field size dependent mapping of medical linear accelerator radiation leakage," Phys. Med. Biol. **60**, 2103-2106 (2015).

[50] A. Perez-Andujar, R. Zhang, W. Newhauser, "Monte Carlo and analytical model predictions of leakage neutron exposures from passively scattered proton therapy," Med. Phys. **40**, 121714 (2013).

[51] J.D. Fontenot, A.K. Lee, W.D. Newhauser, "Risk of Secondary Malignant Neoplasms From Proton Therapy and Intensity-Modulated X-Ray Therapy for Early-Stage Prostate Cancer," International Journal of Radiation Oncology*Biology*Physics **74**, 616-622 (2009).

[52] C. Lee, J.W. Jung, C. Pelletier, A. Pyakuryal, S. Lamart, J.O. Kim, C. Lee, "Reconstruction of organ dose for external radiotherapy patients in retrospective epidemiologic studies," Phys. Med. Biol. **60**, 2309-2324 (2015).

[53] J. Van Dyk, R.B. Barnett, J.E. Cygler, P.C. Shragge, "Commissioning and quality assurance of treatment planning computers," Int J Radiat Oncol Biol Phys **26**, 261-273 (1993).

[54] K.R. Hogstrom, M.D. Mills, J.A. Meyer, J.R. Palta, D.E. Mellenberg, R.T. Meoz, R.S. Fields, "Dosimetric evaluation of a pencil-beam algorithm for electrons employing a two-dimensional heterogeneity correction," Int J Radiat Oncol Biol Phys **10**, 561-569 (1984).

[55] D.A. Low, W.B. Harms, S. Mutic, J.A. Purdy, "A technique for the quantitative evaluation of dose distributions," Med. Phys. **25**, 656-661 (1998).

[56] S. Both, I.M. Alecu, A.R. Stan, M. Alecu, A. Ciura, J.M. Hansen, R. Alecu, "A study to establish reasonable action limits for patient-specific quality assurance in intensity-modulated radiation therapy," Journal of Applied Clinical Medical Physics **8**, 1-8 (2007).

[57] R.M. Howell, I.P.N. Smith, C.S. Jarrio, "Establishing action levels for EPID-based QA for IMRT," Journal of Applied Clinical Medical Physics **9**, 16-25 (2008).

[58] P.S. Basran, M.K. Woo, "An analysis of tolerance levels in IMRT quality assurance procedures," Medical Physics **35**, 2300-2307 (2008).

[59] M. Hussein, E. Clementel, D.J. Eaton, P.B. Greer, A. Haworth, S. Ishikura, S.F. Kry, J. Lehmann, J. Lye, A.F. Monti, M. Nakamura, C. Hurkmans, C.H. Clark, "A virtual

dosimetry audit - Towards transferability of gamma index analysis between clinical trial QA groups," Radiotherapy and Oncology **125**, 398-404 (2017).

[60] G. Yan, C. Liu, T.A. Simon, L.-C. Peng, C. Fox, J.G. Li, "On the sensitivity of patient-specific IMRT QA to MLC positioning errors," Journal of Applied Clinical Medical Physics **10**, 120-128 (2009).

[61] H. Zhen, B.E. Nelms, W.A. Tomé, "Moving from gamma passing rates to patient DVH-based QA metrics in pretreatment dose QA," Medical Physics **38**, 5477-5489 (2011).

[62] B.E. Nelms, H. Zhen, W.A. Tomé, "Per-beam, planar IMRT QA passing rates do not predict clinically relevant patient dose errors," Medical Physics **38**, 1037-1044 (2011).

[63] J.J. Kruse, "On the insensitivity of single field planar dosimetry to IMRT inaccuracies," Medical Physics **37**, 2516-2524 (2010).

[64] M. Stasi, S. Bresciani, A. Miranti, A. Maggio, V. Sapino, P. Gabriele, "Pretreatment patient-specific IMRT quality assurance: A correlation study between gamma index and patient clinical dose volume histogram," Medical Physics **39**, 7626-7634 (2012).

[65] R. Kaderka, D. Schardt, M. Durante, T. Berger, U. Ramm, J. Licher, C. La Tessa, "Out-of-field dose measurements in a water phantom using different radiotherapy modalities," Phys. Med. Biol. **57**, 5059-5074 (2012).

[66] J.O. Deasy, A.I. Blanco, V.H. Clark, "CERR: A computational environment for radiotherapy research," Medical Physics **30**, 979-985 (2003).

[67] C.W. Schneider, W.D. Newhauser, L.J. Wilson, U. Schneider, R. Kaderka, S. Miljanić, Ž. Knežević, L. Stolarcyzk, M. Durante, R.M. Harrison, "A descriptive and broadly applicable model of therapeutic and stray absorbed dose from 6 to 25 MV photon beams," Medical Physics **44**, 3805-3814 (2017).

[68] D.B. Pelowitz, "MCNPX User's Manual Version 2.7.0," (Los Alamos, NM, 2011).

[69] D.L. Friedman, J. Whitton, W. Leisenring, A.C. Mertens, S. Hammond, M. Stovall, S.S. Donaldson, A.T. Meadows, L.L. Robison, J.P. Neglia, "Subsequent Neoplasms in 5-Year Survivors of Childhood Cancer: The Childhood Cancer Survivor Study," JNCI Journal of the National Cancer Institute **102**, 1083-1095 (2010).

[70] J. DeVita, V T, T.S. Lawrence, S.A. Rosenberg, *Cancer: Principles and Practice of Oncology*. (Lippincott Williams and Wilkins, Philadelphia, 2008).

[71] S.F. Kry, B. Bednarz, R.M. Howell, L. Dauer, D. Followill, E. Klein, H. Paganetti, B. Wang, C.-S. Wuu, X. George Xu, "AAPM TG 158: Measurement and calculation of doses outside the treated volume from external-beam radiation therapy," Medical Physics **44**, e391-e429 (2017).

[72] A. Berrington de Gonzalez, R.E. Curtis, S.F. Kry, E. Gilbert, S. Lamart, C.D. Berg, "Proportion of second cancers attributable to radiotherapy treatment in adults: a cohort study in the US SEER cancer registries," Lancet Oncol. **12**, 353-360 (2011).

[73] NCRP, *Second Primary Cancers and Cardiovascular Disease after Radiation Therapy (Report No. 170)*. (National Council on Radiation Protection and Measurements, Bethesda, MD, 2011).

[74] W.D. Newhauser, C. Schneider, L. Wilson, S. Shrestha, W. Donahue, "A REVIEW OF ANALYTICAL MODELS OF STRAY RADIATION EXPOSURES FROM PHOTON- AND PROTON-BEAM RADIOTHERAPIES," Radiation protection dosimetry **180**, 245-251 (2018).

[75] W.D. Newhauser, R. Schulte, A. Berrington de Gonzalez, C. Lee, "A Review of Radiotherapy-Induced Late Effects Research After Advanced-Technology Treatments," Front. Oncol. **6**, 13 (2016).

[76] L. Wang, G.X. Ding, "The accuracy of the out-of-field dose calculations using a model based algorithm in a commercial treatment planning system," Physics in Medicine & Biology **59**, N113 (2014).

[77] M. Stovall, C.R. Blackwell, J. Cundiff, D.H. Novack, J.R. Palta, L.K. Wagner, E.W. Webster, R.J. Shaleck, "Fetal dose from radiotherapy with photon beams: Report of AAPM Radiation Therapy Committee Task Group No. 36," Med. Phys. **22**, 63-82 (1995).

[78] S.F. Kry, U. Titt, F. Pönisch, D. Followill, O.N. Vassiliev, R.A. White, R. Mohan, M. Salehpour, "A Monte Carlo model for calculating out-of-field dose from a Varian beam," Medical Physics **33**, 4405-4413 (2006).

[79] P.J. Taddei, W. Jalbout, R.M. Howell, N. Khater, F. Geara, K. Homann, W.D. Newhauser, "Analytical model for out-of-field dose in photon craniospinal irradiation," Phys. Med. Biol. **58**, 7463-7479 (2013).

[80] L. Irazola, J.A. Terrón, B. Sánchez-Nieto, B. Roberto, F. Sánchez-Doblado, "Peripheral equivalent neutron dose model implementation for radiotherapy patients," Physica Medica **42**, 345-352 (2017).

[81] B. Sánchez-Nieto, R. El-far, L. Irazola, M. Romero-Expósito, J.I. Lagares, J.C. Mateo, J.A. Terrón, F.S. Doblado, "Analytical model for photon peripheral dose estimation in radiotherapy treatments," Biomedical Physics & Engineering Express **1**, 045205 (2015).

[82] L.B. Travis, J.D. Boice Jr., J.M. Allan, K.E. Applegate, *NCRP Report No. 170- Second Primary Cancers and Cardiovascular Disease After Radiation Therapy*. (National Council on Radiation Protection and Measurements, Bethesda, MD, 2011).

[83] J. Eley, W. Newhauser, K. Homann, R. Howell, C. Schneider, M. Durante, C. Bert, "Implementation of an Analytical Model for Leakage Neutron Equivalent Dose in a Proton Radiotherapy Planning System," Cancers **7**, 427 (2015).

[84] W.U. Laub, T.W. Kaulich, F. Nusslin, "A diamond detector in the dosimetry of high-energy electron and photon beams," Phys. Med. Biol. **44**, 2183-2192 (1999).

[85] N. Chofor, D. Harder, B. Poppe, "Non-reference condition correction factor kNR of typical radiation detectors applied for the dosimetry of high-energy photon fields in radiotherapy," Zeitschrift fur medizinische Physik **22**, 181-196 (2012).

[86] N. Chofor, D. Harder, B. Poppe, "Supplementary values of the dosimetric parameters kNR and Em for various types of detectors in 6 and 15 MV photon fields," Zeitschrift fur medizinische Physik **24**, 27-37 (2014).

[87] S.F. Kry, M. Price, D. Followill, F. Mourtada, M. Salehpour, "The use of LiF (TLD-100) as an out-of-field dosimeter," J Appl Clin Med Phys **8**, 169-175 (2007).

[88] R. Zhang, A. Perez-Andujar, J.D. Fontenot, P.J. Taddei, W.D. Newhauser, "An analytic model of neutron ambient dose equivalent and equivalent dose for proton radiotherapy," Phys. Med. Biol. **55**, 6975-6985 (2010).

[89] R. Topolnjak, J.-J. Sonke, J. Nijkamp, C. Rasch, D. Minkema, P. Remeijer, C. van Vliet-Vroegindeweij, "Breast Patient Setup Error Assessment: Comparison of Electronic Portal Image Devices and Cone-Beam Computed Tomography Matching Results," International Journal of Radiation Oncology*Biology*Physics **78**, 1235-1243 (2010).

[90] C.W. Hurkmans, E. Scheepers, B.G.F. Springorum, H. Uiterwaal, "Influence of radiotherapy on the latest generation of implantable cardioverter-defibrillators," International Journal of Radiation Oncology*Biology*Physics **63**, 282-289 (2005).

[91] P. Hauri, R.A. Hälg, J. Besserer, U. Schneider, "A general model for stray dose calculation of static and intensity-modulated photon radiation," Medical Physics **43**, 1955-1968 (2016).

[92] A. Di Fulvio, C. Domingo, M. De San Pedro, E. D'Agostino, M. Caresana, L. Tana, F. d'Errico, "Superheated emulsions and track etch detectors for photoneutron measurements," Radiation Measurements **57**, 19-28 (2013).

[93] Y.S. Kim, Z. Khazaei, J. Ko, H. Afarideh, M. Ghergherehchi, "Estimation of photoneutron yield in linear accelerator with different collimation systems by Geant4 and MCNPX simulation codes," Phys. Med. Biol. **61**, 2762 (2016).

[94] M. Kralik, K. Turek, V. Vondracek, "Spectra of photoneutrons produced by high-energy X-ray radiotherapy linacs," Radiation Protection and Dosimetry **132**, 13-17 (2008).

[95] A. Naseri, A. Mesbahi, "A review on photoneutrons characteristics in radiation therapy with high-energy photon beams," Reports of Practical Oncology and Radiotherapy **15**, 138-144 (2010).

[96] C. Ongaro, A. Zanini, U. Nastasi, J. Ródenas, G. Ottaviano, C. Manfredotti, "Analysis of photoneutron spectra produced in medical accelerators," Phys. Med. Biol. **45**, L55 (2000).

[97] T. Fujibuchi, S. Obara, H. Sato, M. Nakajima, N. Kitamura, T. Sato, H. Kumada, T. Sakae, T. Fujisaki, "Estimate of Photonuclear Reaction in a Medical Linear Accelerator Using a Water-Equivalent Phantom," Progress in Nuclear Science and Technology **2**, 803-807 (2011).

[98] ICRP, *Recommendations of the ICRP. ICRP Publication 26.* (The International Commission on Radiological Protection, New York, NY, 1977).

[99] ICRP, *The 2007 Recommendations of the International Commission on Radiological Protection. ICRP Publication 103*. (International Commission on Radiological Protection, 2007).

[100] ICRP, *Recommendations of the International Commission on Radiological Protection. ICRP Publication 60*. (International Commission on Radiological Protection, Oxford, 1991).

[101] K.-H. Do, "General Principles of Radiation Protection in Fields of Diagnostic Medical Exposure," J. Korean Med. Sci. **31**, S6-S9 (2016).

[102] SCENIHR, "Health effects of security scanners for passenger screening (based on X-ray technology)," in *Scientific Committee on Emerging and Newly Identified Health Risks* (2012).

[103] BFCR, *A guide to understanding the implications of the Ionising Radiation (Medical Exposure) Regulations in diagnostic and interventional radiology.* (The Royal College of Radiologists, London, 2015).

[104] R.H. Corbett, K. Faulkner, "Justification in radiation protection," The British Journal of Radiology **71**, 905-907 (1998).

[105] J. Vom, I. Williams, "Justification of radiographic examinations: What are the key issues?," Journal of Medical Radiation Sciences **64**, 212-219 (2017).

[106] BFCR, "A Guide to Justification for Clinical Radiologists," (Royal College of Radiologists, London, 2000).

[107] ICRP, *Implications of Commission Recommendations that Doses be Kept as Low as Readily Achievable*. (Pergamon Press, Oxford, 1973).

[108] ICRP, *Recommendations of the International Commission on Radiological Protection*. (Pergamon Press, Oxford, 1966).

[109] ICRP, *Optimization and Decision Making in Radiological Protection. ICRP Publication 55*. (The International Commission on Radiological Protection, 1990).

[110] T. Schneider, J. Lochard, L. Vaillant, "Focal role of tolerability and reasonableness in the radiological protection system," Ann. ICRP **45**, 309-321 (2016).

[111] H. Holthusen, "Erfahrungen über die Verträglichkeitsgrenze für Röntgenstrahlen und deren Nutzanwendung zur Verhütung von Schäden," Strahlentherapie **57**, 254-269 (1936).

[112] A.M. Austin, M.J.J. Douglass, G.T. Nguyen, S.N. Penfold, "A radiobiological Markov simulation tool for aiding decision making in proton therapy referral," Phys. Med. **44**, 72-82 (2017).

[113] J. Malone, R. Guleria, C. Craven, P. Horton, H. Järvinen, J. Mayo, G. O'reilly, E. Picano, D. Remedios, J.L. Heron, M. Rehani, O. Holmberg, R. Czarwinski, "Justification of diagnostic medical exposures: some practical issues. Report of an International Atomic Energy Agency Consultation," The British Journal of Radiology **85**, 523-538 (2012).

[114] IAEA/WHO, *Bonn Call for Action: 10 actions to improve radiation protection in medicine in the next decade*. (International Atomic Energy Agency/World Health Organization, Vienna, 2014).

[115] A. Daşu, I. Toma-Daşu, L. Franzén, A. Widmark, P. Nilsson, "Secondary Malignancies From Prostate Cancer Radiation Treatment: A Risk Analysis of the Influence of Target Margins and Fractionation Patterns," International Journal of Radiation Oncology • Biology • Physics **79**, 738-746 (2011).

[116] ICRP, *Compendium of Dose Coefficients based on ICRP Publication 60. ICRP Publication 119*. (International Commission on Radiological Protection, 2012).

[117] E.H. Donnelly, J.B. Nemhauser, J.M. Smith, Z.N. Kazzi, E.B. Farfán, A.S. Chang, S.F. Naeem, "Acute radiation syndrome: assessment and management," Southern medical journal **103**, 541-546 (2010).

[118] A.L. Siu, o.b.o.t.U.S.P.S.T. Force, "Screening for Breast Cancer: U.S. Preventive Services Task Force Recommendation StatementScreening for Breast Cancer," Ann. Intern. Med. **164**, 279-296 (2016).

[119] E.F. Conant, E.F. Beaber, B.L. Sprague, S.D. Herschorn, D.L. Weaver, T. Onega, A.N.A. Tosteson, A.M. McCarthy, S.P. Poplack, J.S. Haas, K. Armstrong, M.D. Schnall, W.E. Barlow, "Breast cancer screening using tomosynthesis in combination with digital mammography compared to digital mammography alone: a cohort study within the PROSPR consortium," Breast Cancer Res. Treat. **156**, 109-116 (2016).

[120] R.E. Hendrick, "Radiation Doses and Cancer Risks from Breast Imaging Studies," Radiology **257**, 246-253 (2010).

[121] NAS-NRC, *Health Risks from Exposure to Low Levels of Ionizing Radiation: BEIR VII Phase 2*. (National Academy of Sciences, Washington, DC, 2006).

[122] R.N. Anderson, P.B. DeTurk, *United States Life Tables, 1999*. (2002).

[123] E. Arias, *United States Life Tables, 2008*. (2012).

[124] E. Arias, M. Heron, J. Xu, *United States Life Tables, 2014*. (2017).

[125] J.F. Faber, A.H. Wade, *Life Tables for the United States: 1900-2050*. (U.S. Department of Health and Human Services, 1983).

[126] X. Li, M. Farid, "A review on recent development in non-conventional food sterilization technologies," Journal of Food Engineering **182**, 33-45 (2016).

[127] N.P. Tipnis, D.J. Burgess, "Sterilization of implantable polymer-based medical devices: A review," International Journal of Pharmaceutics **544**, 455-460 (2018).

[128] M. Lim, Y. Zhou, L. Wang, V. Rudolph, G.Q. Lu, "Development and potential of new generation photocatalytic systems for air pollution abatement: an overview," Asia-Pacific Journal of Chemical Engineering **4**, 387-402 (2009).

[129] S. Shahidi, J. Wiener, "Radiation Effects in Textile Materials," in *Radiation Effects in Materials* (InTech, 2016).

[130] R.-D. Jeong, M.-A. Jeong, M.-R. Park, "Gamma irradiation-induced disease resistance of pear (Pyrus pyrifolia “Niitaka”) against Penicillium expansum," Journal of Phytopathology **165**, 626-633 (2017).

[131] V. Chauhan, Z. Said, J. Daka, B. Sadi, D. Bijlani, F. Marchetti, D. Beaton, A. Gaw, C. Li, J. Burtt, J. Leblanc, M. Desrosiers, M. Stuart, M. Brossard, N.Q. Vuong, R. Wilkins, S. Qutob, J. McNamee, Y. Wang, C. Yauk, "Is there a role for the adverse outcome pathway framework to support radiation protection?," Int. J. Radiat. Biol. **95**, 225-232 (2019).

[132] Y. Lievens, C. Grau, "Health Economics in Radiation Oncology: Introducing the ESTRO HERO project," Radiotherapy and Oncology **103**, 109-112 (2012).

[133] M.D. Stubblefield, "Neuromuscular complications of radiation therapy," Muscle Nerve **56**, 1031-1040 (2017).

[134] A.D. Hutchinson, S.M. Pfeiffer, C. Wilson, "Cancer-related cognitive impairment in children," Current opinion in supportive and palliative care **11**, 70-75 (2017).

[135] N.S. Klee, C.G. McCarthy, P. Martinez-Quinones, R.C. Webb, "Out of the frying pan and into the fire: damage-associated molecular patterns and cardiovascular toxicity following cancer therapy," Ther. Adv. Cardiovasc. Dis. **11**, 297-317 (2017).

[136] M.T. Nolan, D.J. Russell, T.H. Marwick, "Long-term Risk of Heart Failure and Myocardial Dysfunction After Thoracic Radiotherapy: A Systematic Review," Can. J. Cardiol. **32**, 908-920 (2016).

[137] L. Van Le, M. McCormack, "Enhancing Care of the Survivor of Gynecologic Cancer: Managing the Menopause and Radiation Toxicity," American Society of Clinical Oncology educational book. American Society of Clinical Oncology. Annual Meeting **35**, e270-275 (2016).

[138] F.E. van Leeuwen, A.K. Ng, "Long-term risk of second malignancy and cardiovascular disease after Hodgkin lymphoma treatment," Hematology Am. Soc. Hematol. Educ. Program **2016**, 323-330 (2016).

[139] A.M. Groves, C.J. Johnston, J.P. Williams, J.N. Finkelstein, "Role of Infiltrating Monocytes in the Development of Radiation-Induced Pulmonary Fibrosis," Radiat. Res. **189**, 300-311 (2018).

[140] D. Barnea, N. Raghunathan, D.N. Friedman, E.S. Tonorezos, "Obesity and Metabolic Disease After Childhood Cancer," Oncology (Williston Park) **29**, 849-855 (2015).

[141] M. Tukenova, C. Guibout, M. Hawkins, E. Quiniou, A. Mousannif, H. Pacquement, D. Winter, A. Bridier, D. Lefkopoulos, O. Oberlin, I. Diallo, F. de Vathaire, "Radiation Therapy and Late Mortality From Second Sarcoma, Carcinoma, and Hematological Malignancies After a Solid Cancer in Childhood," International Journal of Radiation Oncology • Biology • Physics **80**, 339-346 (2011).

[142] K.K. Hardy, V.W. Willard, A. Gioia, C. Sharkey, K.S. Walsh, "Attention-mediated neurocognitive profiles in survivors of pediatric brain tumors: comparison to children with neurodevelopmental ADHD," Neuro Oncol. **20**, 705-715 (2017).

[143] K.L. Netson, J.M. Ashford, T. Skinner, L. Carty, S. Wu, T.E. Merchant, H.M. Conklin, "Executive dysfunction is associated with poorer health-related quality of life in pediatric brain tumor survivors," J. Neurooncol. **128**, 313-321 (2016).

[144] A.C. Kirchhoff, W. Leisenring, K.R. Krull, K.K. Ness, D.L. Friedman, G.T. Armstrong, M. Stovall, E.R. Park, K.C. Oeffinger, M.M. Hudson, L.L. Robison, T. Wickizer, "Unemployment among adult survivors of childhood cancer: a report from the childhood cancer survivor study," Med. Care **48**, 1015-1025 (2010).

[145] M.M. Hudson, "Reproductive outcomes for survivors of childhood cancer," Obstet. Gynecol. **116**, 1171-1183 (2010).

[146] A. Dumas, R. Allodji, B. Fresneau, D. Valteau-Couanet, C. El-Fayech, H. Pacquement, A. Laprie, T.D. Nguyen, P.-Y. Bondiau, I. Diallo, C. Guibout, C. Rubino, N. Haddy, O. Oberlin, G. Vassal, F. de Vathaire, "The right to be forgotten: a change in access to insurance and loans after childhood cancer?," J. Cancer Surviv. **11**, 431-437 (2017).

[147] J.J. Mao, S.C. Palmer, J.B. Straton, P.F. Cronholm, S. Keddem, K. Knott, M.A. Bowman, F.K. Barg, "Cancer survivors with unmet needs were more likely to use complementary and alternative medicine," J. Cancer Surviv. **2**, 116-124 (2008).

[148] Y. Vinogradskiy, S.L. Tucker, J.B. Bluett, C.A. Wages, Z. Liao, M.K. Martel, "Prescribing radiation dose to lung cancer patients based on personalized toxicity estimates," J. Thorac. Oncol. **7**, 1676-1682 (2012).

[149] P.D.H. Wall, R.L. Carver, J.D. Fontenot, "Impact of database quality in knowledge-based treatment planning for prostate cancer," Pract. Radiat. Oncol. **8**, 437-444 (2018).

[150] ASTRO, *Quantitative analyses of normal tissue effects in the clinic (QUANTEC).* (American Society for Radiation Oncology, New York, NY, 2010).

[151] K.M. Schmeler, A. Jhingran, R.B. Iyer, C.C. Sun, P.J. Eifel, P.T. Soliman, P.T. Ramirez, M. Frumovitz, D.C. Bodurka, A.K. Sood, "Pelvic Fractures After Radiotherapy for Cervical Cancer: Implications for Survivors," Cancer **116**, 625-630 (2010).

[152] ICRP, *Adult Reference Computational Phantoms. ICRP Publication 110.* (International Commission on Radiological Protection, 2009).

[153] J.J. van Tol-Geerdink, P.F. Stalmeier, P.C. Pasker-de Jong, H. Huizenga, E.N. van Lin, E.C. Schimmel, J.W. Leer, W.A. van Daal, "Systematic review of the effect of radiation dose on tumor control and morbidity in the treatment of prostate cancer by 3D-CRT," Int J Radiat Oncol Biol Phys **64**, 534-543 (2006).

[154] E. Dale, T.P. Hellebust, A. Skjonsberg, T. Hogberg, D.R. Olsen, "Modeling normal tissue complication probability from repetitive computed tomography scans during fractionated high-dose-rate brachytherapy and external beam radiotherapy of the uterine cervix," Int J Radiat Oncol Biol Phys **47**, 963-971 (2000).

[155] NCI, *Common Terminology Criteria for Adverse Events v4.0 (CTCAE).* (US Department of Health and Human Services, 2009).

[156] J.M. Michalski, H. Gay, A. Jackson, S.L. Tucker, J.O. Deasy, "Radiation dose-volume effects in radiation-induced rectal injury," Int J Radiat Oncol Biol Phys **76**, S123-129 (2010).

[157] C. Okoukoni, D.M. Randolph, E.R. McTyre, A. Kwok, A.A. Weaver, A.W. Blackstock, M.T. Munley, J.S. Willey, "Early dose-dependent cortical thinning of the femoral neck in anal cancer patients treated with pelvic radiation therapy," Bone **94**, 84-89 (2017).

[158] P.J. Taddei, N. Khater, B. Youssef, R.M. Howell, W. Jalbout, R. Zhang, F.B. Geara, A. Giebeler, A. Mahajan, D. Mirkovic, W.D. Newhauser, "Low- and middle-income countries can reduce risks of subsequent neoplasms by referring pediatric craniospinal cases to centralized proton treatment centers," Biomedical Physics & Engineering Express **4**, 025029 (2018).

[159] L. Tian, G. Landry, G. Dedes, F. Kamp, M. Pinto, K. Niepel, C. Belka, K. Parodi, "Toward a new treatment planning approach accounting for in vivo proton range verification," Phys. Med. Biol. **63**, 215025 (2018).

[160] C. Schneider, W. Newhauser, J. Farah, "An analytical model of leakage neutron equivalent dose for passively-scattered proton radiotherapy and validation with measurements," Cancers (Basel) **7**, 795-810 (2015).

[161] A. Lühr, C. von Neubeck, M. Krause, E.G.C. Troost, "Relative biological effectiveness in proton beam therapy – Current knowledge and future challenges," Clinical and Translational Radiation Oncology **9**, 35-41 (2018).

[162] J.L. Brierton, "Techniques for avoiding local minima in gradient-descent-based ID algorithms," AeroSense '97 **3066**, 6 (1997).

[163] Q. Wu, R. Mohan, "Algorithms and functionality of an intensity modulated radiotherapy optimization system," Med. Phys. **27**, 701-711 (2000).

[164] K. Homann, R. Howell, J. Eley, D. Mirkovic, C. Etzel, A. Giebeler, A. Mahajan, R. Zhang, W. Newhauser, "The need for individualized studies to compare radiogenic second cancer (RSC) risk in proton versus photon Hodgkin Lymphoma patient treatments," Jour Proton Ther **1**, 118 (2015).

[165] R. Miralbell, A. Lomax, L. Cella, U. Schneider, "Potential reduction of the incidence of radiation-induced second cancers by using proton beams in the treatment of pediatric tumors," Int. J. Radiat. Oncol. Biol. Phys. **54**, 824-829 (2002).

Vita

Lydia Wilson was born in Winfield, Illinois to Diane Batistich and John Scott Wilson. After falling in love with physics, she graduated from Downers Grove South High School in 2005 and moved to sunny California to attend the University of California, Berkeley where she majored in physics and minored in music. After receiving her Bachelor of Arts in 2009, Lydia spent a year backpacking across Europe and living in Sydney, Australia. During this time, she became interested in the field of medical physics and went on to receive her Master of Science from Louisiana State University in 2013. Lydia then embarked on another year-and-a-half long adventure as the recipient of a Fulbright Student Fellowship to Croatia where she researched radiotherapy healthcare disparities in the capital city of Zagreb. Upon the conclusion of this fellowship, Lydia decided she really missed the sweet, sticky appeal of red stick and returned to LSU in January of 2015 to pursue her PhD in medical physics. During her doctoral studies, Lydia kept a degree of balanced insanity to her life by teaching Zumba fitness classes and hiking hundreds of miles in the rain, snow, and desert heat. Upon completion of her dissertation, Lydia will be moving to Memphis, Tennessee to begin a postdoctoral fellowship at St. Jude Children's Research Hospital where she will continue pursuing her life's goal of saving the world one pediatric-cancer patient at a time.